

**DYNAMIC AND STATIC TEM STUDIES
ON THE FORMATION OF Au-Si AND
Au-Ge NANOSTRUCTURES**

By

ASHUTOSH RATH
INSTITUTE OF PHYSICS
BHUBANESWAR, INDIA

A THESIS SUBMITTED TO THE
BOARD OF STUDIES IN PHYSICAL SCIENCE DISCIPLINE

IN PARTIAL FULLFILLMENT OF REQUIREMENTS
FOR THE DEGREE OF

DOCTOR OF PHILOSOPHY
OF
HOMI BHABHA NATIONAL INSTITUTE



SEPTEMBER, 2012

Homi Bhabha National Institute

Recommendations of the Viva Voce Board

As members of the Viva Voce Board, we certify that we have read the dissertation prepared by **Mr. Ashutosh Rath** entitled “*Dynamic and static TEM Studies on the Formation of Au-Si and Au-Ge Nanostructures*” and recommend that it may be accepted as fulfilling the dissertation requirement for the Degree of Doctor of Philosophy.



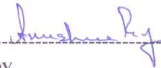
Chairman – A. Srivastav

Date: 21.09.2012



Guide / Convener – P. V. Satyam

Date: 21.09.2012



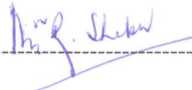
Member 1 – Anushree Roy

Date: 21.09.2012



Member 2 – S. Varma

Date: 21.09.2012

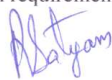


Member 3 – B. R. Sekhar

Date: 21.09.2012

Final approval and acceptance of this dissertation is contingent upon the candidate's submission of the final copies of the dissertation to HBNI.

I hereby certify that I have read this dissertation prepared under my direction and recommend that it may be accepted as fulfilling the dissertation requirement.


(P. V. Satyam)

Date: 21st September 2012

Place: Bhubaneswar

Statement By Author

This dissertation has been submitted in partial fulfillment of requirements for an advanced degree at Homi Bhabha National Institute (HBNI) and is deposited in the Library to be made available to borrowers under rules of the HBNI.

Brief quotations from this dissertation are allowable without special permission, provided that accurate acknowledgement of source is made. Requests for permission for extended quotation from or reproduction of this manuscript in whole or in part may be granted by the Competent Authority of HBNI when in his or her judgment the proposed use of the material is in the interests of scholarship. In all other instances, however, permission must be obtained from the author.

Ashutosh Rath
Institute of Physics
Bhubaneswar

Declaration

I, Ashutosh Rath, hereby declare that the investigations presented in the thesis have been carried out by me. The matter embodied in the thesis is original and has not been submitted earlier as a whole or in part for a degree/diploma at this or any other University/Institution.

Ashutosh Rath
Institute of Physics
Bhubaneswar

Acknowledgments

Now, at the end of the research period for my PhD thesis, I want to express my thanks to several people who have contributed to the thesis development.

First, I would like to express my sincere appreciation to my advisor Prof. P. V. Satyam for giving me the unique opportunity to work in his group and his fatherly care for the work and me. In his group, I enjoyed the freedom to make decisions and tried every absurd ideas. I owe a great depth of gratitude to him for his continuous encouragement and enthusiastic motivation throughout and beyond this work. I am indebted to him for his excellent guidance and for providing excellent facilities. I am eternally thankful to him for teaching me some very important skills and supporting me on my career goals in every imaginable way. It is my very pleasure to thank for his fruitful input as a reader of this thesis.

I am grateful to the Director, IOPB for all the help I received from him during my stay here.

I would like to thank Prof. Andreas Roesnauer, University of Bremen, Germany as collaborator for the investigations with 300 KeV Titan Machine.

It was a great pleasure for me to spend the last 4 years working in the Electron microscopy group. I gratefully acknowledge the individual help and support from our TEM group members. I express thanks to all my colleagues for creating the pleasant atmosphere, especially Dr Jay Ghatak, Dr Umananda M Bhatta, Jatis, Raghav, Arnab and Anjan. Everyone has helped me one way or another. It is my innermost urge to Jay bhai and Uma bhai for being the strongest supporters of me, for their patience with an unexperienced graduate student, for their guidance during my learning period and for sharing their intellectual property(both in academics and social issues). Special thanks to Jatis for being a great colleague and friend. Raghav needs

a special word of appreciation for his help in sharing the responsibility of running the microscopy facility (doing the routine maintenance work of our microscopy lab) and giving me ample time to finish writing my thesis.

I enjoyed the company of all my colleagues and many more and I would like to thank them for all their help in making my stay a pleasant experience here at IOPB. Multiple cheers go to all scholars (starting from 1999 predoc batch to 2010 batch) in the IOP campus. I feel so blessed that I have been surrounded by this set of nice people. Special thanks to Hara bhai for making me happy. It was always fun to listen stories of the old times that he told me.

No experimental work would be successful without skilled technical support. Thanks to Mr S.R. Mohanty (Soumya), Mr B .K. Dash and Mr A.K Dash for providing it and always being patient, even if I had many requests. Thanks to Soumya for his always quick and reliable help. I wish my all juniors (raghav, anjan and arnab) the best and a lot of success for the remaining parts of their PhD studies.

I acknowledge the excellent library and computer facilities provided by the IOP and the timely help of all the academic as well as non academic staff.

Finally, but not the least I wish to express my deep sense of gratitude to my parents and sisters. Your love has always been the very reason that motivates me to go forward. It was their encouragement, support and affection that helped me immensely in completing this thesis work.

TO MY PARENTS

List of Publications

1. ^{1‡} Epitaxial growth of Au-Ge nanostructures on Ge(100) surface under ultra high vacuum condition.
A. Rath, J. K. dash, R. R. Juluri, A. Ghosh and P. V. Satyam,
To be submitted (2012):arXiv:1208.0238
2. ^{1‡} Dynamic and Static Transmission Electron Microscopy Studies on Structural Evaluation of Au nanoislands on Si (100) Surface.
A. Rath, R. R. Juluri and P. V. Satyam
J. Crystal Growth (Under review, 2012): arXiv:1204.4618.
3. ^{1‡} Structural Modification in Au/Si(100) system: Role of surface oxide and vacuum level.
A. Rath, J. K Dash, R. R. Juluri and P. V. Satyam,
J. Vac. sci. technol. A-Lett.(Under review, 2012): arXiv:1204.5370
4. ^{1‡} Nano scale phase separation in Au-Ge system on ultra clean Si(100) surfaces.
A. Rath, J. K. Dash, R. R. Juluri, Marco Schoewalter, Knut Mueller, A. Rosenauer and P.V. Satyam,
J. Appl. Phys. **111**, 104319 (2012): arXiv:1202.0614
5. ^{1‡} Growth of Oriented Au Nanostructures: Role of Oxide at the Interface.
A. Rath, J. K. Dash, R. R. Juluri, A. Rosenauer, Marco Schoewalter and P.V. Satyam,
J. Appl. Phys. **111**, 064322 (2012):arXiv:1203.0819
6. ^{1‡} Temperature dependent electron microscopy study of Au thin films on Si(100) with and without native oxide layer as barrier at the interface.
A. Rath, J. K. Dash, R. R. Juluri, A. Rosenauer and P.V. Satyam,
J. Physics D: Applied Physics **44**, 115301 (2011).

7. Shape Evolution of MBE grown $\text{Si}_{1-x}\text{Ge}_x$ Structures on High Index Si(5 5 12) surfaces : A temperature tempendent study
J. K. Dash, **A. Rath**, R. R. Juluri and P. V.Satyam,
J. Physics D: Applied Physics (In press, 2012): arXiv:1205.6039
8. Universality in Shape Evolution of $\text{Si}_{1-x}\text{Ge}_x$ Structures on High Index Silicon Surfaces
J. K. Dash, T. Bagarti, **A. Rath**, R. R. Juluri and P. V.Satyam,
Euro. Phys. Lett. (In press, 2012): arXiv:1204.0578
9. Migration and extrusion of metal nanowire inside the filled multi-walled carbon nanotube
Pawan K. Tyagi,Umananda M Bhatta, **Ashutosh Rath**, J. Raghavendra Rao, Jatis K. Dash,Sanjeev Kumar, and P V Satyam,
Carbon(Under review, 2012)
10. MeV Au^{2+} ions induced surface patterning in silica
P. Santhana Raman, K.G.M. Nair, M. Kamruddin, A.K. Tyagi, **A. Rath**, P.V. Satyam, B.K. Panigrahi and V. Ravichandran.
Applied Surface Science **258**, 4156-4160(2012)
11. Epitaxy-like orientation of nano scale Ag islands grown on air-oxidized Si(110)-(5×1) surfaces.
Anupam Roy, J. K. Dash, **A. Rath** and B. N. Dev,
Accepted in *Surface and Interface Anlysis(2011)(wileyonlinelibrary.com)* DOI 10.1002/sia.3837.
12. Synthesis of re-dispersible Ce^{3+} co-doped $\text{LaPO}_4:\text{Tb}^{3+}$ nanorods and effects of concentrations of Ce^{3+} or Tb^{3+} and reaction medium on luminescence properties: luminescence switching behavior through redox reaction and polymer films.
G. Phaomei,R. S. Ningthoujam,W.R.Singh, R.S. Loitongbam,N.S.Singh, **Ashutosh Rath**, R. R. Juluri and R. K. Vatsa,
Dalton Trans. **40**, 115301(2011).
13. Shape transformation of $\text{Si}_{1-x}\text{Ge}_x$ structures on ultra clean Si (5 5 7) and Si (5 5 12) surfaces. J. K. Dash, **A.Rath**, R. R. Juluri,P Santhana Raman, K.

- Muller, M. Schowalter, R. Imlau, A. Rosenauer and P. V. Satyam
J. Phys.: Conf. Ser. **326**, 012021(2011).
14. DC heating induced shape transformation of Ge structures on ultra clean Si (5 5 12) surfaces
 J. K. Dash, **A. Rath**, R. R. Juluri, P. Santhana Raman, K. Muller, A. Rosenauer and P. V. Satyam ,
J. Phys.: Condens. Matter **23**, 135002 (2011).
 15. Oxidation of Ion Beam Synthesized Embedded indium Nanoclusters in Silica.
 P. Santhana Raman, K. G. M. Nair, **Ashutosh Rath**, P. V. Satyam, B. K. Panigrahi and V. Ravichandran,
Eur. Phys. J.: Applied Physics **53**, 30403 (2011).
 16. Growth of SnO₂/WO₃- nano wire hierarchical hetero-structure and their application as chemical sensor.
 S. Sen, P. Kanitkar, A. Sharma, K. P. Muthe, **Ashutosh Rath**, S. K. Deshpande, M. Kaur, R. C. Aiyer, S. K. Gupta and J. V. Yakhmi
Sensors and Actuators B: Chemical, **147**, 453-460(2010).
 17. Antiferro to superparamagnetic transition on Mn doping in NiO,
 P. Mallick, Chandana Rath, **A. Rath**, A. Banerjee and N. C. Mishra,
Solid State Communications, **150**, 1342-1345(2010).
 18. Real-time study of oxide mediated liquid-solid growth of high aspect ratio - aligned gold silicide microrods on Si(110) substrates.
 Umananda M. Bhatta, **Ashutosh Rath**, Jatis K. Dash, Jay Ghatak, Lai Yi-Feng, Chuan-Pu Liu and P. V. Satyam,
Nanotechnology **20**, 465601 (2009).
 19. Structural phase transitions in Au thin films on Si (110): An *in-situ* temperature dependent transmission electron microscopy study.
 Umananda M. Bhatta, J. K. Dash, **A. Rath** and P. V. Satyam,
Appl. Surf. Sci. **256**, 567 (2009).
 20. Formation of aligned nano-silicide structures in MBE grown Au/Si(110) system: A real-time temperature dependent TEM study.

Umananda M. Bhatta, J. K. Dash, Anupam Roy, **A. Rath** and P. V. Satyam,
J Phys: Cond. Matt. **21**, 205403 (2009).

21. Surface and Interfacial Structural Characterization of MBE Grown Si/Ge Multilayers.

Biswajit Saha, Manjula Sharma, Abhisakh Sarma, **Ashutosh Rath**, P.V. Satyam,
Purushottam Chakraborty, Milan K. Sanyal,
Applied Surface Science, **256**, 547-551(2009).

Conference Presentations

- ^{1‡} Shape transition in Au/Si(100) System : Role of surface oxide and vacuum Level.
A. Rath, J. K. Dash, R. R. Juluri and P. V. Satyam,
ICONSAT-2012, Hyderabad, India.
- ^{1‡} Shape transition in Au/Si(100) hetero epitaxial system: Role of vacuum level during annealing
Ashutosh Rath, J. K. Dash, R. R. Juluri and P. V. Satyam,
ICANN-2011, Guwahati, Assam, India.
- ^{1‡} Nano pattern formation in Ge/Au/Si(100) hetero epitaxial system
A. Rath, J. K. Dash, R. R. Juluri and P.V. Satyam,
IINM-2011, International conference on Ion beam induced nano patterning of materials Institute of Physics, Bhubaneswar, India.
- Temperature dependent structural phase transformation from nano to microstructures: A real time TEM study.
Umananda M. Bhatta, J. Ghatak, **A. Rath**, J. K. Dash, P. Santhana Raman and P. V. Satyam,
PSI - 2009, International Conference on Physics at surfaces and interfaces, Puri, India
- Formation of AuSi microrods on Si(110) surface: A real time TEM study.
Umananda M. Bhatta, J. Ghatak, **A. Rath**, P. Santhana Raman, P.V. Satyam,
DAE-Solid State Physics Symposium (India) **53**, 809(2008).

1

^{1‡} Papers on which this thesis is based upon.

Synopsis

The thesis work involves an extensive study on the formation of Au–Si and Au–Ge nanostructures under different thermal annealing conditions achieved by varying parameters such as, pressure, film thickness, substrate, presence or absence of native oxide on the substrate, temperature *etc.*

As the nano particle size and shape plays a crucial role on the unique material properties [1-3], studies of the particle size and shape evolution could be useful in providing a mechanistic insight into the manipulation and control of their properties and functionalities. Making use of these unique material properties at the nanoscale largely depends on the ability to control the size and shape of these nanostructures for various applications. This in turn is influenced by the details of substrate preparation, temperature of the substrate, rate of material deposition, chemical form of the depositing species and ambient conditions which can all affect the growth of thin films and lead to dramatically different morphologies for the same combination of materials [4]. The processes by which nano materials and nano devices are produced are mainly divided into two approaches: top-down and bottom-up. Top-down process has been successfully used in making sub micron scale structures easily and it's economical viability helped much in progress of electronic industries. On the other hand, bottom-up synthesis, such as self assembly growth help to move on to nanometer scale as the involved processes are atomic in nature [5]. The bottom-up techniques, once properly tuned, offer the potential to fabricate nano materials and nano devices in large scale. This thesis work is on understanding of the bottom-up approach process using real time *in-situ* TEM studies. There have been a large number of studies where in various material properties getting enhanced or changed dramatically at the nanoscale. Gold is one such example which is known to be chemically inert in its bulk form behaves completely different in its nano form as far as optical, catalytic and mechanical properties are concerned. As a result it holds great promise in applications such as building blocks for nano–bioelectronic devices [6, 7], catalysts [8] and sensors

[9]. Specifically, several works have been done using the alloyed nanostructures of Au *viz* Au-Si and Au-Ge as catalysts for the growth of Ge and Si nano wires [10-14]. It has been well studied that the phase stability and phase transformation of the catalyst determine properties such as the growth rate and the structure of the nano wire [15, 16]. It is therefore natural that the physics and chemistry of these materials is the current research subject of great interest [17]. This thesis work focuses on the use of bottom-up nano particle self-assembly techniques to synthesize well tuned Au, Ge, Au-Si, and Au-Ge alloyed nano structures. Our results suggest that, by varying the parameters such as temperature and interface conditions, we can form Au-Si and Au-Ge nano-structures of various shapes and sizes which can be used as catalysts for growing various crystalline nanowires. The range of the study covers thin film thickness from as low as 2.0 nm to 50 nm of gold and germanium. The emphasis in my thesis work is on the use of transmission electron microscopy (TEM) for carrying out in-situ temperature dependent structural variations in Au and Ge nanostructures and their respective alloys on silicon and germanium substrate.

The thesis is organized as follows. Chapter one is the introduction to the thesis and gives a brief overview about the interest in assembling nano particles in 2D and 3D and several methods available in the literature for the same. It also discusses the importance of these nanostructures with respect to their optical and catalytic properties and different routes of synthesis of these nanostructures.

Chapter two describes the experimental characterization techniques that have been consistently used for the depiction of the work. Transmission Electron Microscopy (TEM), High Resolution TEM (HRTEM), Scanning TEM (STEM), Scanning electron microscopy (SEM), Electron dispersive x-ray analysis (EDX), Electron backscattered diffractometry (EBSD), Focused ion beam (FIB) measurement are some of the techniques which have been extensively used to illustrate the formation of nanostructures and their properties. Physical vapor deposition method and molecular beam epitaxy method are used to deposit thin films. The physical principles of different techniques and their application to understand the various aspects of formation of the nano/micro structures have been presented. Remaining chapters of this thesis describe the study of formation of Au and Ge nanostructures and their respective alloys (Au-Si and Au-Ge alloy).

Various thicknesses of gold thin films were deposited using MBE as well as thermal evaporation technique. Difference in the temperature dependent behavior of

gold nanostructures on Si (100) surfaces in presence and absence of native oxide layer were studied in-situ using a hot-stage holder (GATAN, Model 628). In case of MBE samples, formation of highly oriented square /rectangular shape nano structures were observed at high temperatures (500°C). Strain relaxation and substrate symmetry plays a major role in the alignment of these Au-Si nanostructures [18]. In case of samples with native oxide layer, formation of bigger sized rectangular structures was observed at higher temperatures (850°C). Native oxide at the interface was found to act like a barrier for the inter-diffusion phenomena. At these higher temperatures, due to desorption of native oxide present at the interface, rectangular structures were formed. We observed desorption of gold and /or gold silicide structures and formation of symmetric hole like structures in some cases [18]. Using different thicknesses of gold films in both cases (with and without native oxide layer), size of the nanostructures could be controlled.

In thickness dependent studies (5, 11.7 and 50 nm Au on SiO_x/Si) at low vacuum ($\approx 10^{-2}$ mbar) annealing did not reveal any alloy formation, rather well oriented gold nanostructures at high temperature ($\approx 975^\circ\text{C}$) was observed. The shape of the oriented structures can be tuned with a variable initial thickness of gold films: Au films with lower thickness (≈ 5 nm) lead to spherical particles. Increasing the film thickness result in the formation of oriented and faceted gold structures. The effects of native oxide layer on morphology, orientations of the structures were studied in detail. Interfacial oxide layer, low vacuum and high temperature annealing conditions are found to be necessary to grow oriented gold structures. We also showed that oriented microstructures cannot be fabricated without oxide layer at the interface (using MBE method) [19]. These gold structures can be transferred by simple scratching method.

We further extended our understanding of the influence of vacuum conditions upon the formation of nanostructures in presence and absence of oxide layer. A ≈ 2 nm Au deposited on SiO_x /Si by thermal evaporation method was annealed at high temperature (850°C) under both high vacuum (HV) and low vacuum (LV) conditions. In HV, gold silicide rectangles were observed following the four-fold symmetry of the substrate due to selective thermal decomposition of native oxide layer, where as in LV, it does not show any such formation. This has been explained as due to low vacuum which ensures that the rate of formation(re-deposition) of oxide over takes over the rate of oxide decomposition in a relatively oxygen rich environment compared

to high vacuum conditions [20]. To study the effect of vacuum conditions on MBE grown samples (without oxide layer), 2nm Au/Si(100) sample was annealed at 500°C in three different vacuum conditions: (i) LV external furnace ($\approx 10^{-2}$ mbar), (ii) ultra high vacuum (UHV at $\approx 10^{-10}$ mbar) chamber (MBE chamber), (iii) HV($\approx 10^{-7}$ mbar). Although well aligned nano rectangles were formed in both HV and LV, corner rounding is more prominent in LV. Furthermore in UHV, random structures were formed having sharp corners. In all the above three cases, samples were exposed to air before annealing. To study the effect of surface oxide, *in-situ* annealing inside UHV–MBE chamber was done without exposing to air. Well aligned rectangles with sharp corners (no corner rounding) were formed [21]. The details about the role of surface oxide in the corner rounding process are discussed in this thesis.

One of the utilization of such Au-Si nanostructures as a catalyst is to study the controlled formation of lobe-lobe (bi-lobed) Au-Ge nanostructures under UHV conditions on clean Si(100) surfaces. For this study, ≈ 2.0 nm thick Au films were grown by molecular beam epitaxy (MBE). Nearly square shaped $\text{Au}_x\text{Si}_{1-x}$ nano structures of average length ≈ 48 nm were formed after UHV annealing at temperature $\approx 500^\circ\text{C}$. A ≈ 2 nm Ge film was further deposited on the annealed sample while the substrate was kept at $\approx 500^\circ\text{C}$. Well ordered Au-Ge nanostructures where Au and Ge residing side by side (lobe-lobe structures) were formed. In our systematic studies, we show that, gold-silicide nano alloy formation at the substrate (Si) surface is necessary for forming phase separated Au-Ge bilobed nanostructures [22]. The morphology of such bi-lobed structures has been tuned by varying thickness (amount) of the Ge, substrate temperature and sequence of material deposition. It has been studied that the bonding between Au and Ge is unstable which leads to the phase separation [23]. Our results also indicate that Si–Ge bonding is more favorable to have than having Au–Ge bond. This observation of phase separation at nanoscale would be very useful for proper understanding of gold contacts on Si-Ge based devices.

To study this nanoscale phase separation and its effect on the formation bilobed structures, it would be interesting to study growth of Au on Ge. For this study, ≈ 2.0 nm thick Au films were grown on Ge (100) substrate by MBE. Nearly square shaped $\text{Au}_x\text{Ge}_{1-x}$ nano structures were formed after UHV annealing at temperature $\approx 500^\circ\text{C}$. A ≈ 2 nm Ge film was further deposited on the annealed sample while the substrate was kept at $\approx 500^\circ\text{C}$. Well distributed Au-Ge nanostructures with Au on the top of the pedestal Ge were formed. It is very interesting to notice that no

Au-Ge bilobed structures were formed like previous case. To study the temperature dependence, similar Ge deposition was performed at the substrate temperature of 600°C. The height of the pedestal Ge increased with temperature [24]. The detailed study of the Au-Ge interface has been done in this work.

The last chapter summarizes the work presented in the thesis and emphasizes on the possible further research in this area.

References

1. J. P. Borel, *Surf. Sci.* **106**, 1(1981).
2. Y. D. Glinka, S. H. Lin, L. P. Hwang, Y. T. Chen, N. H. Tolk, *Phys. Rev. B* **64**, 085421(2001).
3. C. Burda, X. Chen, R. Narayanan, M. A. El-Sayed, *Chem. Rev.* **105**, 1025(2005).
4. M. Zinke-Allmang, L. C. Feldman, M. H. Grabow, *Surf. Sci. Rep.* **16**, 381(1992).
5. Rosei Federico, *J. Phys.: Condens. Matter* **16**, S1373-S1436 (2004).
6. M. G. Warner and J. E. Hutchison, *Nature Materials* **2**, 272 (2003).
7. Y. Xiao, F. Patolsky, E. Katz, J. F. Hainfeld, and I. Willner, *Science* **299**, 1877 (2003).
8. A. T. Bell, *Science* **299**, 1688 (2003).
9. S. O. Obare, R. E. Hollowell, and C. J. Murphy, *Langmuir* **18**, 10407 (2002).
10. R. S. Wagner and W. C. Ellis, *Appl. Phys. Lett.* **4**, 89 (1964).
11. J. B. Hannon, S. Kodambaka, F. M. Ross and R. M. Tromp, *Nature* **440**, 69 (2006).
12. G. A. Bootsma and H. J. Gassen, *J. Cryst. Growth* **10**, 223(1971).
13. S. Kodambaka, J. Tersoff, M. C. Reuter and F. M. Ross, *Science* **316**, 729 (2007).
14. Hemant Adhikari, Ann F. Marshall, Irene A. Goldthorpe, Christopher E. D. Chidsey, and Paul C. McIntyre, *ACS nano* **1**, 415-422(2007).

15. E. A. Sutter and P. W. Sutter, *ACS Nano* **4**, 4943 (2010).
16. B. Kim, J. Tersoff, S. Kodambaka, M.C. Reuter and F. M. Ross, *Science* **322**, 1070(2008).
17. Metal Nanoparticles; Synthesis, Characterization, and Applications, ed. D. L. Feldheim and C. A. Foss, Dekker, New York (2002).
18. A. Rath, J. K. Dash, R. R. Juluri, A. Rosenauer and P.V. Satyam, *J. Physics D: Applied Physics* **44**, 115301 (2011).
19. A. Rath, J. K. Dash, R. R. Juluri, A. Rosenauer, Marco Schoewalter and P.V.Satyam, *J. Appl. Phys.* **111**, 064322 (2012):arXiv:1203.0819.
20. A. Rath, R. R. Juluri and P. V. Satyam, *J. Crystal Growth* (Under review, 2012) :arXiv:1204.4618.
21. A. Rath, J. K Dash, R. R. Juluri and P.V. Satyam, *J. Vac.sci.technol A-Lett.* (Under review, 2012) :arXiv:1204.5370.
22. A. Rath, J. K. Dash, R. R. Juluri, Marco Schoewalter, Knut Mueller, A. Rosenauer and P.V. Satyam, *J. Appl. Phys.* **111**, 104319 (2012):arXiv:1202.0614.
23. E. Sutter and P. Sutter, *Nanotechnology* **22**, 295605 (2011).
24. A. Rath, J. K Dash, R. R. Juluri, A. Ghosh and P. V. Satyam(to be submitted, 2012):arXiv:1208.0238

Contents

Statement By Author	iii
Declaration	iv
Acknowledgments	v
List of Publications	viii
Synopsis	xii
1 Introduction	1
2 Experimental techniques	7
2.1 Introduction	7
2.2 Thin film Growth	8
2.2.1 Physical vapor deposition Method	8
2.2.2 Molecular beam epitaxy	9
2.2.3 Low vacuum annealing setup	14
2.3 Characterization techniques	14
2.3.1 Transmission electron microscopy	15
2.3.2 FIB-SEM-Cross beam system	24
2.3.3 Electron Backscatter Diffraction Technique (EBSD)	30
2.3.4 Scanning Transmission Electron Microscopy (STEM)	31
2.3.5 Rutherford Backscattering Spectrometry	34
3 Temperature-dependent electron microscopy study of Au thin films on Si(100)	38
3.1 Introduction	38
3.2 Experimental methods	41

3.3	Results and discussions	42
3.4	Conclusions	53
4	Growth of Oriented Au Nanostructures: Role of Oxide at the Interface	54
4.1	Introduction	54
4.2	Experimental Section	56
4.3	Results and discussion	57
4.3.1	Formation of oriented Au Structures	59
4.3.2	Role of Vacuum level and interfacial oxide	61
4.3.3	Study of orientation of the Faceted Gold structures	65
4.4	Conclusions	68
5	Structural modification of gold silicide structures in Au/Si(100)system: Role of vacuum level and surface oxide	69
5.1	Introduction	69
5.2	Experimental methods	71
5.3	Results and discussions	72
5.3.1	With oxide at the interface	72
5.3.2	Without oxide at the interface	78
5.4	Conclusions	82
6	Nano scale phase separation in Au-Ge system on ultra clean Si(100) surfaces	83
6.1	Introduction	83
6.2	Experimental details	86
6.3	Results and discussion	87
6.4	Conclusions	96
7	Gold assisted molecular beam epitaxy of Ge nanostructures on Ge (100) Surface	97
7.1	Introduction	97
7.2	Experimental methods	99
7.3	Results and discussions	100
7.4	Conclusions	106

8 Summary	107
A Table to summarize the results of chapter 3-chapter 5	111

List of Figures

2.1	Schematic illustration of the three equilibrium growth modes: (a) layer- by-layer (Frank-van der Merwe, FM) growth mode (b) layer-plus-island (Stranski-Krastanov, SK) growth mode (c) Island (Volmer-Weber, VW) growth mode [77].	11
2.2	A custom-designed compact MBE system (MBE chamber diameter: 250 mm) and a UHV variable temperature scanning tunneling microscope (VTSTM) attached to it.	13
2.3	A schematic diagram of (a) Filament and illumination part, (b) Diffraction pattern formation and (c) Image formation [79].	17
2.4	A schematic diagram of different processes taking place during electron–solid interaction.	18
2.5	200 keV JEOL HRTEM installed at Institute of Physics, Bhubaneswar.	21
2.6	A schematic diagram of procedure to prepare a typical planar TEM specimen.	22
2.7	A schematic diagram of procedure to prepare a typical cross-sectional TEM specimen.	22
2.8	Single tilt hot stage holder installed at IOP, Bhubaneswar (Model 628, Gatan, Inc.).	24
2.9	FIB-SEM crossbeam system installed at Institute of Physics, Bhubaneswar.	26
2.10	A schematic diagram of different processes taking place during electron–solid interaction	29
2.11	Schematic diagram of detector geometry for a STEM [94].	32
2.12	A schematic diagram of the interaction of two particles [97].	35
2.13	A schematic diagram of the RBS spectrum for a thin film [97].	36

3.1	As deposited MBE sample showing (a) gold nanostructures with typical size of about ~ 24 nm (b) SAD pattern showing reflections of both Si and Au and corresponding (c) high resolution image of one of the islands which is showing the d-spacing of Au(111). [127].	42
3.2	Bright field transmission electron micrographs depicting real time morphological changes during the <i>in-situ</i> heating. (a), (b), (c), (d), (e), (f), (g), (h) and (i) show the morphology at 200°C, 300°C, 325°C, 350°C, 363°C, 400°C, 510°C, 600°C and 700°C, respectively. With increasing temperature, growth of rectangular nanostructures can be seen [127].	43
3.3	<i>In-situ</i> SAD patterns taken at various temperatures during heating of 2.0 nm Au/Si(100) system. (a), (b), (c), (d), (e) and (f) show the real-time diffraction pattern at 325°C, 350°C, 363°C, 510°C, 600°C and 700°C respectively [127].	45
3.4	(a) Bright field image taken at room temperature after the sample was heated up to 700°C, (b)selected area diffraction showing the presence of mixed phase of silicide and (c) high resolution transmission electron micrograph of single nano rectangles.[127]	47
3.5	(a) Showing <i>as-deposited</i> thermally grown nanostructures 5 nm Au/SiO ₂ /Si(100) system, (b) corresponding SAD pattern showing the reflection of Au and Silicon, (c) BF transmission electron micrograph at 850°C and (d) corresponding selected area diffraction pattern [127].	49
3.6	(a) STEM– HAADF image on one of gold silicide structure. This shows formation of a hole like structure: (b) the elemental mapping formed with Au x-ray signals, (c) with Si x-ray signals in the STEM-XEDS mode [127].	51
3.7	(a) STEM–HAADF image on one of larger gold silicide structure. This shows formation of many holes like structures inside (b) the TEM bright field image of same structure that was shown in (a)[127].	52
3.8	The lattice image taken from the area shown with circles in figure 3.7(b)[127].	53
4.1	(a) SEM image of <i>as-deposited</i> samples of 5 nm Au/SiO ₂ /Si(100) (b) SEM image taken at <i>RT</i> after annealed upto 975°C (c) corresponding bright field TEM image (inset figure shows the HRTEM image of one of the multiply twinned decahedral gold structure).	57

4.2	(a) BF XTEM image of <i>as-deposited</i> samples 5 nm Au/SiO ₂ /Si(100) and (b) corresponding HRTEM image. (c) shows the XTEM image of the 5 nm Au/SiO ₂ /Si(100) taken at <i>RT</i> after annealed upto 975°C and (d) corresponding HRTEM image.	58
4.3	(a)SEM image of <i>as-deposited</i> samples 11.7 nm Au/SiO ₂ /Si(100)(b) SEM image taken at <i>RT</i> after annealed upto 975°C and (c) corresponding XTEM image.	59
4.4	SEM image of 50nm Au/SiO ₂ /Si(100) heated upto 975°C (a) elemental mapping which shows the presence of substrate silicon (b) and Au (c) and corresponding EDX spectrum (d).	59
4.5	(a) SEM image of <i>as deposited</i> samples 50 nm Au/SiO ₂ /Si(100), (b) SEM image taken at <i>RT</i> after the sample was annealed upto 975°C (inset figure shows SEM image taken at 5 KeV electron energy), (c) corresponding XTEM image and (d) SAD pattern taken on one of the Au island.	60
4.6	SEM image shows the (a) 11.7nm Au grown by MBE (without native oxide at the interface) method which is annealed upto 975°C inside LV and (b)corresponding XTEM image (inset figure shows the SAD pattern) (c) thermally grown (with oxide) 11.7 nm Au annealed upto 975°C inside HV and (d)corresponding XTEM image	61
4.7	(a)SEM image of thermally grown 50 nm Au heated upto 975°C inside HV (b) corresponding Bright field TEM image and (c) the HRTEM image shows the presence of gold silicide.	63
4.8	(a) STEM image from 50 nm Au/SiO _x /Si(100) annealed at 975°C. (b) is the region taken at higher magnification from a selected area in (a). Fig. c(i) is from the Oxygen EELS line scan from region (i) and d(ii) is from the region (ii) shown in (b). Width of the variation of oxide layer thickness can be seen in (c) and (d)[161].	64
4.9	SEM image of 50 nm Au/thermally grown 50 nm SiO _x /Si(100) substrate annealed at 975°C under low vacuum ((inset figure shows SEM image taken at 5 KeV electron energy.)	65
4.10	(a) SEM based EBSD orientation mapping in 50 nm Au/SiO _x /Si(100) annealed at 975°C, (b) and (c) corresponding inverse pole figures (d) histogram plot of the misorientation angle <i>Vs</i> number fraction [161].	66

4.11	(a) SEM image taken at 54° tilt from 50 nm Au/SiO _x /Si(100) annealed at 975°C, (b) corresponding XSEM image showing the contact angle between the faceted structure and the silicon. The schematic diagram shows the planes of the facets.	67
4.12	SEM image of the faceted gold particles on the carbon coated copper grid which are transferred from the silicon substrate by simple scratching method.	67
5.1	(a) BFTEM image of thermally grown <i>as-deposited</i> sample 2 nm Au/SiO _x /Si(100) showing nanostructures (b) Corresponding SAD pattern showing the reflection of Au and silicon (c) Bright Field transmission electron micrograph at 850°C (<i>system-A1</i>) (d) Corresponding selected area diffraction pattern and the ring (arrow marked) indicates the alloy formation [172].	74
5.2	Real time bright field TEM image depicting the growth of a nano rectangle at the expense of gold nano particles (at 850°C)[172].	76
5.3	Bright field TEM image depicting the real time morphological changes during <i>in situ</i> heating (stabilized at the temp of 850°C)[172].	77
5.4	(a) 2 nm Au/SiO ₂ /Si(100) was <i>ex-situ</i> annealed (at 850°C) under low vacuum (<i>system-A2</i>) and then seen in TEM at RT (b) corresponding SAD showing the reflection of gold and silicon [172].	77
5.5	(a) Reflection high energy electron diffraction (RHEED) pattern showing clean reconstructed Si100-(2× 1) surface (b) Bright field TEM image shows the as deposited 2nm Au/Si(100) system.	78
5.6	Bright field TEM image of MBE grown 2 nm Au/Si(100) system annealed upto 500°C inside (a) HV chamber and (c) LV chamber having average length 29.4 ± 1.5 nm (b) and 21.9 ± 1.2 nm (c) respectively. Inset figure shows the HRTEM image of one of the structures.	80
5.7	Bright field TEM image of MBE grown 2 nm Au/Si(100) system annealed upto 500°C inside UHV chamber (a) (with air-exposed) and (c) without air exposed (<i>in-situ</i>) having average length 38.2 ± 1.4 nm (b), 56.4 ± 1.6 nm (d) respectively. <i>Inset</i> figure shows the HRTEM image of one of the structures.	81
6.1	Schematic diagrams showing (a) the formation of gold silicide, (b) Ge nano structures and (c) Au-Ge bi-lobed structures on a Si substrate.	86

6.2	(a) <i>As-deposited (sample A)</i> showing gold nanostructures with corresponding high resolution image of one of the islands which is showing the d-spacing of Au(111) in the inset (b) SAD pattern showing reflection of both Si and Au, (c) bright field TEM image taken for the sample that was annealed at 500°C in UHV chamber (<i>sample B</i>) with corresponding high resolution image of one of the single islands (<i>inset</i>), (d) SAD pattern showing the formation gold silicide along with the reflection Au and Si for the sample B, (e) bright field high resolution XTEM image of one of the nanostructure (<i>sample B</i>) showing inter-diffusion of Au into Si. (f) Depicts a SAD pattern taken at RT for the sample that was annealed <i>in-situ</i> TEM at 400°C (<i>sample G</i>) and then cooled to RT. This shows no gold silicide formation at 400°C [203].	89
6.3	Length distribution(fitted with Gaussian distribution) along $\langle 110 \rangle$ direction, of the sample shown in Fig. 6.2(c) which shows an average length of 48.1 ± 1.1 nm and (b) corresponding aspect ratio distribution and average aspect ratio is 0.99 ± 0.01 (here the histograms are fitted with Gaussian distribution to estimate the mean aspect ratio) (c) length distribution(fitted with Gaussian distribution) of the sample shown in Fig. 6.4(a) (for several frames) which shows the average length is 116 ± 1.8 nm and (d) corresponding aspect ratio distribution and average aspect ratio is 1.12 ± 0.03 (here the histograms are fitted with log-normal distribution to estimate the mean aspect ratio) [203].	90
6.4	(a) SEM image taken at 0° tilt (c) 54° tilt; (b) depicts a XTEM image of epitaxially grown Ge nano structures and (d) for Au-Ge bilobed structures (<i>sample C</i>) [203].	91
6.5	(a) Bright field TEM image of one of the bi-lobed Au-Ge nanostructures and (b) corresponding HRTEM images showing the Au-Ge alloy formation at the Au-Ge junction. (c) depicts STEM micrograph (<i>sample C</i>) and (d) STEM-EDS elemental mapping (<i>sample C</i>)[203]. . . .	92
6.6	SEM image taken at RT after 5.0 nm Ge deposited on Au patterned substrate at (a) 400°C (b) 500°C and (c) 600°C. This shows that no bi-lobed structures are formed at 400°C. Corresponding RBS spectra in (d) show diffusion status of Au and Ge in Silicon at 400°C (<i>sample F1</i>), 500°C (<i>sample F2</i>) and 600°C (<i>sample F3</i>) [203].	93

6.7	Schematic diagram showing the Au and Ge lobe making angle θ_1 and θ_2 respectively with the normal to the triple point. Here the segmented line is perpendicular to the image plane.	95
6.8	SEM images showing absence of Au-Ge bilobed structures for (a) <i>sample D</i> and (b) for <i>sample E</i> [203].	96
7.1	For <i>as deposited</i> MBE sample (<i>sample A</i>), (a) SEM micrograph showing gold nanostructures (b) XTEM image showing the interface of Au thin film and Ge substrate and corresponding high resolution image (<i>inset figure</i>) shows d-spacing of Au(200) and Ge(111) [216].	101
7.2	(a) SEM image taken at 54° tilt for the sample that was annealed at 500°C in UHV chamber (<i>sample B</i>) (b) corresponding bright field XTEM image of the islands and (c) high resolution XTEM image of one of the nanostructure (<i>sample B</i>) showing inter-diffusion of Au into Ge substrate [216].	101
7.3	(a) SEM micrograph taken at RT after 2.0 nm Ge deposited on Au patterned substrate at 500°C (<i>sample C</i>), (b) corresponding XTEM image shows the Au-Ge nanostructures along with the Ge nano islands (the High resolution of the square marked region is shown in the <i>inset</i>), (c) HRXTEM image of one of the Au-Ge islands depicts the pedestal Ge underneath the Au and (d) filtered image of the square marked region shows the formation of Au-Ge composition at the interface [216].	103
7.4	(a) SEM micrograph taken at RT after 2.0 nm Ge deposited on Au patterned substrate at 600°C (<i>sample D</i>), (b) corresponding XTEM image shows the Au-Ge nanostructures, (c) HRXTEM image of one of the Au-Ge islands depicts the pedestal Ge underneath the Au and (d) filtered image of the square marked region shows the formation of Au-Ge composition at the interface [216].	104
7.5	High resolution XTEM of the sample taken at <i>RT</i> after 2 nm Ge was deposited on Ge (100) followed by UHV annealing at 500°C (<i>sample E</i>), shows the homo epitaxial growth of Ge layer on Ge (100) [216]. .	105

Chapter 1

Introduction

Nano science, nanotechnology, nano particles and nanostructures are among the most widely used terms in the modern scientific and technological literature. The area of nano science and nanotechnology is growing very rapidly and is believed to lead to dramatic modifications of many of our activities such as information technology and communication, medicine, materials, space, energy, water *etc.* [1, 2, 3, 4, 5, 6, 7]. Nanoscience is the study of phenomena and manipulation of materials at atomic, molecular and macro molecular scales, where properties differ significantly from those at the bulk scale. Nanotechnologies are the design, characterization, production and application of structures, devices and systems by controlling shape and size at the nanometer scale [8]. It has already shown a variety of important achievements. For example, in realization of molecular-scale transistors using semiconducting carbon nanotubes [9] and superiority of semiconductor quantum dots in high power laser diodes [10]. The potential application of hexagonal mesoporous silicas in catalysis [11] and in controlled drug release [12] has also been demonstrated. Nano particles are often applied as additives *e.g.* for the reinforcement of steel [13] and for the production of precipitation-hardened alloys [14].

The properties of materials can be different at the nano scale for two main reasons : nano materials have a relatively large surface area when compared to the same mass of material produced in bulk form, which make materials more chemically reactive and affect their strength or electrical properties. The increasing surface to volume ratio with decreasing size results in increased significance of grain boundaries. Thus, nano particles often exhibit exceptional physical properties such as, high coercive force [15],

giant magneto-resistance [16], high thermal stability and super plasticity [14, 17]. It is also expected that the quantum effects can begin to dominate the behavior (optical, magnetic and electrical) of materials at the nanoscale. In the case of nanomaterials, the size [18, 19], shape [20], surface composition [21], dielectric environment of the particle [22] and the inter particle interactions [23] are the key factors that can modulate the chemical, optical, magnetic and electronic properties. As mentioned above, the structural arrangement of atoms and the length scales of the material are the two important parameters, which when tuned properly at the nanometer scale, could lead to variation in the properties of the material, compared to its bulk. That means, at least in one dimension the material should be in nano meter scale so that it will confine the electronic structure in that dimension. As the nano particle size/shape plays a crucial role on the unique material properties, studies of the particle size and shape evolution could be useful in providing an insight into the manipulation and control of their properties and functionalities. Thus, for the design of novel advanced functional nano materials the uniformity of the shape and size of the nanoparticles is also a key issue. It has been shown by several groups that how shape tunes the catalytic behavior of the nanoparticles [24]. However, the synthesis of nano particles with uniform size and shape is difficult. Thus, large scale synthesis of nano materials remains a challenge.

Top-down and Bottom-up are the two approaches that have been used for the synthesis of nanomaterials [25]. Top-down approach involves mainly physical methods where a bulk material is sliced into pieces till the desired size is achieved. Lithographic techniques, laser induced chemical etching and ball milling fall into this category. But it is very difficult to synthesize nanostructures. For example, in case of nano lithography method, the sizes of the structures are limited by the resolution of the lithography. The bottom-up approaches mainly involve chemical and biological methods and also physical method (thin film growth and self assembly) to make nano structures. As the traditional *top-down* approach for device scaling in micro- electronics technology is recently encountering strong challenges due to physical resolution limits, a new way of the *bottom-up* type in manufacturing devices is presently under investigation. Recently, self-assembled techniques have attracted considerable interest for nanoscale device applications because these techniques offer the potential to fabricate nanoscale elements such as quantum dots, quantum wires and electronic device

configuration without direct use of conventional lithography techniques. A number of self-assembly techniques have been reported for fabricating nanoscale structures. One type of self-assembly involves the preparation of semiconductor/metal islands, and it can be carried out by a technique called heteroepitaxy, which involves the placement or deposition of the material that forms the island on a supporting substance made of a different material with a closely matched interface between them. Heteroepitaxy has been widely used for research, as well as for the fabrication of many semiconductor devices, so it is a well-developed technique. It involves bringing atoms or molecules to the surface of the substrate where they do one of three things as mentioned in the following. They are either adsorbed and diffuse about on the surface until they join or nucleate with another *adatom* to form an island attach themselves to or aggregate into an existing island or desorb and thereby leave the surface. Small islands can continue to grow, migrate to other positions or evaporate. There is a critical size at which they become stable and no longer experience much evaporation. Thus, there is an initial nucleation stage when the number of islands increases with the coverage. This is followed by an aggregation stage when the number of islands level off and the existing ones grow in size. Finally, there is the coalescence stage when the main events that take place involve the merger of existing islands with each other to form larger islands. There have been numerous interesting studies on the mechanism of relaxation of strain in such epitaxial layers. Strained epitaxial layers are inherently unstable and have interesting properties. It has been reported that the dislocation formation and the shape transition are the important processes by which relaxation of strain occurs [26, 27, 28, 29]. In recent years, it has been recognized that shape changes such as island formation constitute a major mechanism for strain relief [26, 28]. Tersoff and Tromp reported that a strain-induced shape transition may occur [26]. Below a critical size, islands have a compact symmetric shape. For larger sizes, they adopt a long thin shape that allows better elastic relaxation of the island's stress [26].

Metallic nanoparticles are important for both theoretical and practical view points. They represent one of the most promising classes of nano materials by virtue of their interesting optoelectronic, thermal, magnetic, and superior catalytic properties [30, 31, 33, 32], which result in the preparation of new materials for energy storage, photonics, communications and sensing application [34, 35, 36, 37]. Unlike the bulk

metals, in the case of metal nanoparticles the conduction band is absent being replaced by discrete states at the band edge because of the quantum-confinement of the electrons. As the spectrum of the potential applications of metallic nanoparticles is diversifying every day, there is a tremendous interest in preparation of metal nanoparticles with uniform sizes and shapes by cost-effective and easily scalable procedures. Gold has been for many years a case metal to study the changes in physical and chemical properties at nano scale. This precious element has long been known as being essentially chemically inert (and therefore catalytically inactive) in its bulk form [38]. Quite recently, however, it was found that, when dispersed in the form of nanoscale clusters and supported on transition metal oxide surfaces such as TiO_2 [39, 40], Au exhibits a very high (low temperature) catalytic activity for the partial oxidation of hydrocarbons, hydrogenation of unsaturated hydrocarbons and reduction of nitrogen oxides [41]. It was shown that the catalytic properties of Au nanoparticles depend specifically on the support, the preparation method and critically, on the size of the Au clusters, which are active when their diameter is smaller than 3.5 nm [42, 39]. Furthermore, the catalytic behavior depends on whether the overlayer nanostructures are in direct contact with its support material or they will have to overcome a barrier. For example inter diffusion behavior of metal (overlayer) – semiconductor (substrate) system is strongly influenced by the presence or absence of an oxide layer at the interface. It has been shown that the interfacial diffusion of gold and silicon occurs at lower temperature in absence of interfacial oxides than in presence of oxide [28, 29, 43]. It is well known that, at elevated temperature and high vacuum conditions, silicon oxide thin films decompose to expose the clean Si surface [44, 45]. This would contribute to play important role in controlling the inter-diffusion and reaction of gold with silicon. Detailed explanation of thermal decomposition of oxide layer and the resulting growth of gold silicide nanostructures would be presented in this thesis work.

Furthermore, gold has been widely used as a catalyst for metal-catalyzed *vapor-liquid-solid* (VLS) growth [46]. In this method, a nanometer-sized metallic seed particle which forms a low temperature eutectic alloy with the wire material acts as a site of preferential, unidirectional crystal growth. While wire growth is a nonequilibrium process, the equilibrium phase diagram provides important guidance on the conditions such as temperature and liquid composition needed for nanowire fabrication. Unfortunately, these temperatures and compositions cannot be determined from the

bulk phase diagram, even if the wire is growing very close to equilibrium, due to the major influence of capillarity and stress in these nanoscale objects. Hourlier *et al* have studied thermodynamically the relative stability of different systems solid and liquid at equilibrium involved in the growth of semiconductor nanowires. They calculated it for the two binary systems Au-Si and Au-Ge [47]. Sutter and Sutter have measured the equilibrium composition of a Au-Ge liquid alloy drop on the end of a Ge nanowire using *in situ* heating in a transmission electron microscope (TEM) [48]. These results indicate that phase boundaries in the nanowire system are shifted to lower temperatures compared to those of a bulk system. A direct observation of the VLS growth of Ge nanowires was reported by Wu and Yang [49], who identified the various growth stages in correlation to the Au-Ge binary phase diagram. Similar *in situ* observation of VLS growth of Si NWs by using ultrahigh-vacuum transmission electron microscopy was reported by Ross et al [50]. Haraguchi *et al* applied the VLS mechanism using gold droplets as catalysts for the growth of III-V NWs, for example, GaAs and InGaAs [51]. In this thesis work, goldsilicide is used as catalyst for the growth of Au-Ge bilobed structures. It is similar to the VLS growth of Ge with Au-Si as transport medium, except molecular-beam source is used instead of a chemical compound vapor like CVD growth. The detail mechanism would be discussed in this thesis.

Direct observation of nano structural evolution under dynamic reaction conditions is a powerful scientific tool in materials science. Numerous advancements have been achieved in electron microscopy in the past decades. Not only has the spatial resolution been improved, image recording techniques have been revolutionized by the application of CCD cameras and analytical spectroscopies with almost atomic resolution have been integrated into the standard electron microscope. For example, *in-situ* electron microscopy provides dynamic information on processes under controlled reaction conditions which can not be obtained directly by other techniques. Some of the earlier *in situ* experiments carried out in high vacuum in the TEM have produced important results. *In-situ* experimentation requires specially designed specimen stages that fit into the narrow gap of the objective pole pieces for high resolution microscopy. Nowadays, varieties of specimen stages are available, for example for heating, cooling, electrical probing, straining or indentation of the specimen [52]. Incorporation of a genuine UHV range suitable for surface science studies was started by Pashley [53]

and has been developed into a powerful scientific tool by Yagi and coworkers [54]. The value of using a hot stage to study *in situ* crystallization with lattice imaging in a high vacuum environment of a TEM has been demonstrated [55]. Any type of phase transformation that can be induced by temperature changes within the limits of the heating holder can be examined by *in-situ* hot stage measurements. These include order-disorder reactions [56], grain-boundary motion [57], melting-freezing of materials [58], interfacial reaction [59], crystallization [60], faceting-roughening transitions [61], nanoparticle reactions [62], coarsening [63], quasimelting [64] and catalytic reaction [65], *etc.* Elegant experiments have been performed and the results of these studies are relevant to the wider surface science community. Among these, our interest lies mainly in nanoparticles reaction by using the heating holder. In some part of this thesis work, *in situ* studies of temperature dependent behavior of gold nanoparticles (of different sizes) on single crystalline silicon substrate with and without native oxide layer has been presented.

The thesis is organized as follows. The principle and instrumentation of various thin film deposition methods and characterization techniques employed in this thesis work is demonstrated in chapter 2. The temperature dependent *in situ* studies of formation of well aligned rectangular nano gold silicide structures on Si (100) surfaces with and without an oxide layer at the interface is reported in chapter 3. The study of formation of the highly oriented faceted gold structures is the topic of chapter 4. Role of interfacial oxides and low vacuum condition on the formation of above faceted structures is demonstrated experimentally in this chapter. Chapter 5 outline the vacuum dependence study, where the effect of different vacuum level on the formation of gold silicide structures and their shape in presence or absence of native oxide is explained in detail. In chapter 6, the role of gold silicide nanostructures as a catalyst in the formation of phase separated lobe-lobe (bi-lobed) Au-Ge nanostructures under UHV conditions on clean Si(100) surfaces has been described. Chapter 7 describes the out of plane growth of epitaxial Au-Ge nanostructures on clean Ge (100) surface under UHV condition. The effect of substrate temperature on the formation of above structures was studied in detail. The summary of the work presented in the thesis and possibility of further research in this area is given in chapter 8.

Chapter 2

Experimental techniques

2.1 Introduction

This chapter covers the details on experimental techniques employed to accomplish the objectives of this thesis. The chapter would begin with an introduction to thin film deposition and various types of deposition techniques that have been used in this thesis. This is followed by description of characterization techniques *viz.* transmission electron microscopy (TEM), scanning electron microscopy (SEM), scanning transmission electron microscopy (STEM), focused ion beam (FIB), electron backscatter diffraction Technique (EBSD) and Rutherford backscattering spectrometry (RBS).

The gold and germanium nanostructures can be synthesized in several ways like thermal vapor deposition and molecular beam epitaxy(MBE) method, where the bulk metal is subjected to resistive heating under high vacuum/ultra high vacuum conditions. Depending on the rate of deposition, vacuum level and substrate condition, the gold nanostructure morphology varies. In this thesis work, deposition of gold nanostructures onto silicon substrates has been done using both vacuum coating method and molecular beam epitaxy (MBE) method and germanium deposition has been done using the MBE. The detailed will be discussed in the following sections.

2.2 Thin film Growth

Thin film growth is an essential part in modern device fabrication. It is desirable to have an ability to control morphology and microstructure to meet functional requirements of devices made by stacking thin film layers. Understanding of growth kinetics is, therefore, crucial in advancing the modern technology. Besides this practical purpose, it has been a challenging fundamental scientific subject and is still an active research area.

Thin film depositions can be either purely physical-like evaporative methods, or purely chemical-like gas and liquid phase chemical processes [66]. Some of the other techniques which involve glow discharge and reactive sputtering can be regarded as physical-chemical methods. In this thesis, only physical *viz.* vacuum coating method will be discussed.

2.2.1 Physical vapor deposition Method

Thermal evaporation (physical vapor deposition) is the vaporization of a material by heating to a temperature such that the vapor pressure becomes appreciable and atoms or molecules are lost from the surface in vacuum[68]. Physical Vapor Deposition (PVD) employs the atomic vapor cloud formed by the vaporization of metal in a vacuum environment to cover all the surfaces. It involves the following sequential steps: (i) Conversion of deposited material into vapour by heating, (ii)Transportation of material from source to the target substrate and (iii) Condensation of the vapour on the substrate and formation of thin film. Heating of the material in PVD can be done in several ways. The simplest one is the resistive heating, when a wire of tungsten or molybdenum is resistively heated, so that the metal being in thermal contact to the wire melts and evaporates (sublimation can occur as well). In electron beam evaporation, a beam of electrons is directed at the material, thus heating up and evaporating the material. A thermal evaporator uses an electric resistance heater to melt the material and raise its vapor pressure to a useful range. This is done in a high vacuum (generally 5×10^{-5} to 1×10^{-6} mbar) both to allow the vapor to reach the substrate without reacting with or scattering against other gas-phase atoms in the chamber and reduces the incorporation of impurities from the residual gas in the vacuum chamber. Obviously, only materials with a much higher vapor pressure than

the heating element can be deposited without contamination of the film. The principal requirement for successful thin film growth in this experiment is that the mean free path of the gold atoms must be greater than the distance between the source and substrate [69].

In this thesis work, we have used thermal evaporation technique to deposit the material. Au films of various thicknesses were deposited using Hind hivac made thermal evaporator (model 12A4-D). The deposited material was placed in a tantalum boat. A large current was passed through this boat, heated it up and melted the material to be deposited. The coating unit for this system consists of a cylindrical, stainless steel vacuum chamber, approximately 55 cm tall and 40 cm in diameter. This chamber is connected to double stage pumping system: 250 liter per min rotary pump and 280 liter per second oil diffusion pump. There is a stationary sample stage placed 12cm away from the boat at the top of the chamber for holding substrates, including a shutter for controlling film growth, and there is an evaporation boat at the bottom of the chamber. Pirani and Penning gauge are used to measure the vacuum level during deposition. Thickness of the thin film was controlled using thickness monitor with quartz crystal microbalance. The quartz crystal mechanically oscillates when ac voltage is applied to it (piezoelectric effect)[67]. The resonance frequency of oscillations is dependent on the mass of the film deposited onto it. Quartz monitors can measure thickness of about a single atomic layer with relatively high accuracy. The calibration is checked routinely with RBS experiment.

2.2.2 Molecular beam epitaxy

This is another vacuum deposition technique but carried out under ultra high vacuum (UHV). While characterizing a surface on an atomic level, basic requirement will be that the surface composition essentially remains unchanged over the duration of the experiment. This requires that the experimental chamber to be in ultra high vacuum. The concept of vacuum can be understood in terms of parameters such as molecular density, mean free path and the time constant to form a monolayer(ML). where one ML corresponds to 6.78×10^{14} atoms cm^{-2} for a Si(100) surface. At UHV, mean free path of atoms/molecules present in the chamber is of the order of kilo meters and the time required for the formation of a monolayer is almost a hour. Whereas in low vacuum ($\approx 10^{-2}$ mbar) it reduces to fraction of a centimeter and time required

for monolayer is fraction of milisecond [76]. Molecular beam epitaxy (MBE) is an advanced, sophisticated vacuum deposition process under UHV conditions, where in, significantly more precise control of beam fluxes and growth conditions are possible. The growth process is governed by mainly the kinetics of the surface processes occurring when the incident atomic/molecular beam interacts with a few surface atomic layers of the substrate crystal. As it is done in UHV, the growth process may be observed and controlled by *in-situ* surface sensitive methods such as reflection high energy electron diffraction (RHEED), Auger electron spectroscopy (AES) etc.

MBE was developed in the early 1970's as a technology to grow high-purity epitaxial layers of compound semiconductors [70, 71]. Since then, it has evolved into a popular technique for growing compound semiconductors Si[72, 73, 74, 75] and Ge, as well as several other materials, such as oxides. MBE can produce high-quality single crystal layers with very abrupt interfaces, monolayer control of thickness, precise doping and compositional accuracy. Because of the high degree of control and flexibility using MBE, it is a valuable tool in the development of sophisticated electronic, magnetic and photonic devices. The operating principle behind MBE is conceptually very straightforward; a source material is heated up to a high enough temperature where a considerable vapor pressure is realized and the development of a directed vapor towards a substrate is accomplished by the process called *effusion*. Consider a container filled with gas molecules in equilibrium. If a small hole is made in the wall of the container, molecules with the *right* velocity components will effuse out of the container through the small hole, forming a molecular beam (after which MBE is named). When the hole is sufficiently small, only a tiny portion of the gas molecules effuses out of the container and the equilibrium state is disturbed to a negligible extent. Molecular-beam epitaxy (MBE) is a process of depositing epitaxial films from molecular beams on a heated crystalline substrate under ultra-high vacuum (UHV) conditions. UHV conditions are necessary in order to prevent the interference of impurities with the growth.

Growth Modes

The growth of deposited thin film can take any form during deposition depending upon the deposition conditions (viz. temperature and pressure during deposition,

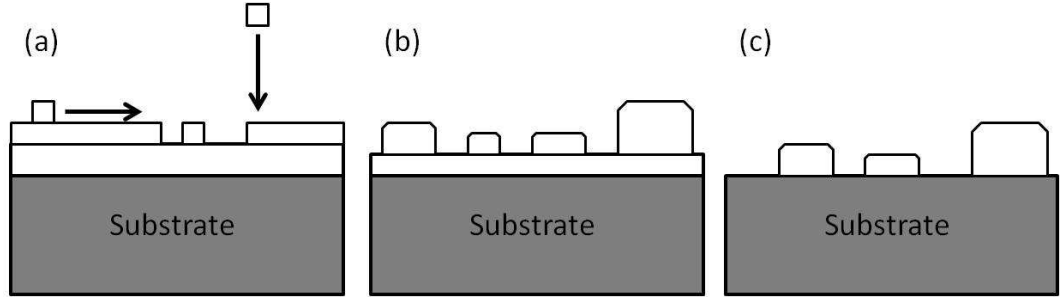


Figure 2.1: Schematic illustration of the three equilibrium growth modes: (a) layer-by-layer (Frank-van der Merwe, FM) growth mode (b) layer-plus-island (Stranski-Krastanov, SK) growth mode (c) Island (Volmer-Weber, VW) growth mode [77].

chemical bonding between the substrate and the material, surface energy of film and substrate). For the determination of the growth mode, the surface free energies of the substrate (γ_{sub}), interface (γ_{int}) and the film (γ_{film}) are important[76, 77]. The growth of thin film depends on the resultant free energy as follows:

$$\Delta\gamma = \gamma_{film} + \gamma_{int} - \gamma_{sub} \quad (2.1)$$

Island growth mode(VW Growth)

In this growth mode, the smallest stable clusters nucleate on the substrate and grow in three dimensions to form islands. This happens when the deposited atoms are more strongly bound to each other than to the substrate. Hence, adsorbate forms 3-dimensional islands instead of a complete layer. This type of growth is commonly known as Volmer-Weber growth (Fig. 2.1(c)). Here $\Delta\gamma > 0$. This growth mode is typical for metal on insulators.

Layer Growth Mode (FM Growth)

In this growth mode, the smallest stable clusters grow in two dimensions, resulting in the formation of planar sheets. This happens when the atoms are more strongly bound to the substrate than to each other. The adsorbate is forming a complete monolayer before a second layer starts on top of the first. This type of growth is commonly known as Frank-van der Merwe growth (Fig. 2.1(a)). Here $\Delta\gamma \leq 0$. An example of this growth mode is single crystal epitaxial growth of semiconductor films.

Layer plus Island growth mode (SK Growth)

This growth mode is considered as intermediate between the FM and VW growth modes. After forming the first few monolayer, subsequent growth is unfavourable and islands are formed on the top of the intermediate layer. This type of growth is commonly known as Stranski-Krastanov (Fig. 2.1(b)). It happens if $\Delta\gamma \leq 0$ and the materials have large lattice mismatch and strain associated. This is due to the influences of the surface and the interfaces and also the film structure, determined by the initial condensation process. First it tries to form a wetting layer and after a critical thickness when no more strain can be accommodated, then only island forms. In SK growth, islanding happens to relieve the misfit strain. The clusters grow in size and density until the islands begin to merge in what is known as the coalescence phenomenon. Coalescence decreases the island density allowing further nucleation to occur. The strain-assisted self assembly in the Ge/Si(100) system is a popular example of this growth mode.

Relaxation and Reconstruction: The atoms at solid surfaces have missing neighbors on one side. Driven by this asymmetry, the topmost atoms often assume a structure different from the bulk. They might form dimers or more complex structures to saturate dangling bonds. In the case of *surface relaxation*, the lateral or in-plane spacing of the surface atoms remains unchanged but the distance between the topmost atomic layers is altered. If the lateral distance of the atoms are changed, this is called the *surface reconstruction*. For example, semiconductor surfaces tend to exhibit surface reconstruction due to the directional character of the dangling bonds at the surface. Reconstruction can be readily detected by electron diffraction techniques, including low-energy electron diffraction (LEED) and reflection high-energy electron diffraction (RHEED).

A photograph of the MBE system used [78] for this thesis work is shown in Fig. 2.2. It is a custom-designed, compact MBE system along with the capability to transfer the MBE-grown samples to a UHV STM without breaking vacuum (Omicron, GmbH) (Fig. 2.2). It consists of a load-lock chamber and growth chamber which is connected to the STM chamber. Each chamber has an associated pumping system. The load-lock facilitates the introduction and removal of samples or wafers without

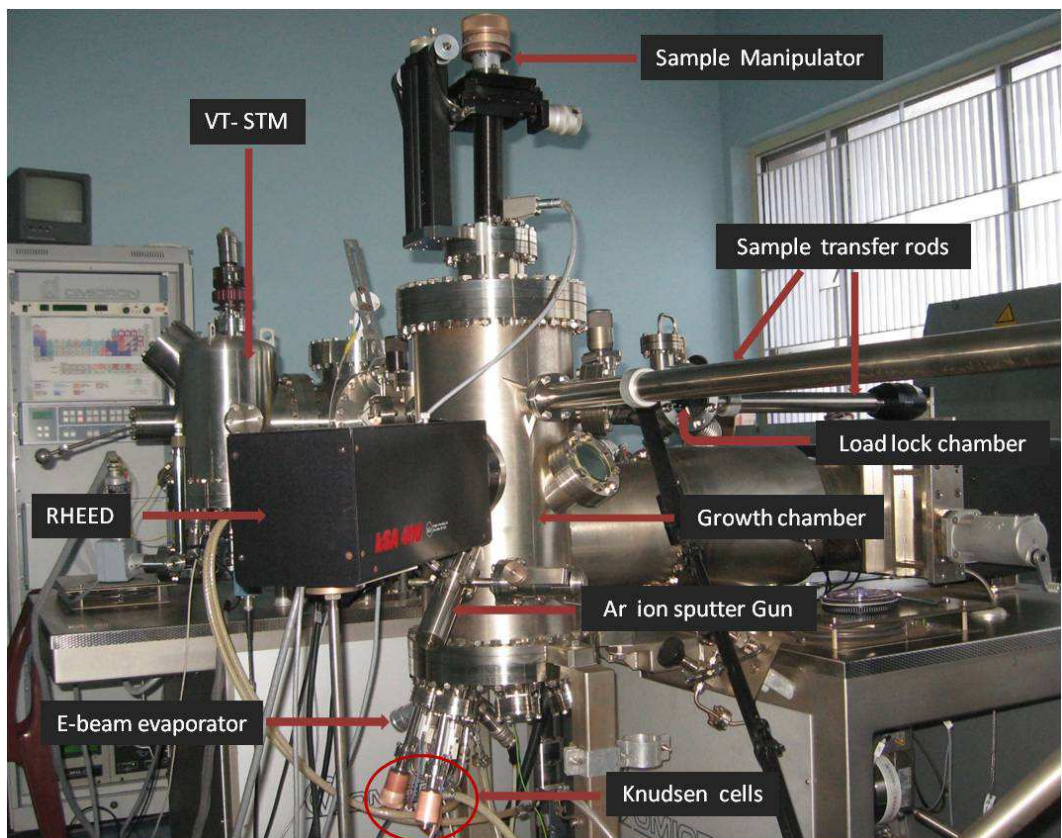


Figure 2.2: A custom-designed compact MBE system (MBE chamber diameter: 250 mm) and a UHV variable temperature scanning tunneling microscope (VTSTM) attached to it.

significantly influencing the growth chamber vacuum. Magnetic transfer rods are used to transfer the sample to main chamber and to STM chamber. The main elements of growth chamber are: sources of molecular beams (Three Knudsen cells and an electron beam evaporator); a manipulator for heating, translating and rotating the sample; shutters to occlude the molecular beams; gauge to measure chamber base pressure and molecular beam fluxes; a RHEED (reflection high energy electron diffraction) gun and screen to monitor film surface structure. Thickness is measured by a quartz microbalance. Sample cleaning is done by resistive heating followed by direct heating. It has an option for Ar sputtering as well. Three Knudsen cells contain Au, Ag and Ge sources. Electron beam evaporator is used for Si deposition. In STM chamber (VTSTM), the temperature range available is -248°C to 1227°C . The best base pressure achieved in the MBE chamber is 3×10^{-11} mbar and that in the VTSTM chamber is 1×10^{-10} mbar.

2.2.3 Low vacuum annealing setup

The low vacuum annealing setup used for this work is a tube furnace connected to a rotary pump. The vacuum inside the chamber is about $\approx 10^{-2}$ mbar and the maximum temperature it can go upto 1400°C with heating rate 1°C to 10°C . The heating element used in this set up are SiC rods. The temperature is controlled by the honeywell DC-1040 temperature controller with 10 steps programmable and automatic control. The heating zone inside the tube is about 10 cm. The same chamber is used for the growth of oxides by connecting one end of the tube to the oxygen cylinder.

2.3 Characterization techniques

In-situ study of thermal behaviour of gold nanostructures has been done mainly by transmission electron microscope (TEM). Scanning transmission electron microscope (STEM) with its major accessories has also been used to do structural characterization at room temperature. Single tilt hot-stage holder was used in carrying out *in-situ* annealing studies. Characterization of samples was also done using SEM based EBSD. All the above tools will be discussed briefly in the following sections.

2.3.1 Transmission electron microscopy

In the advancement of materials science and engineering, it is necessary to observe, analyze and understand the phenomena occurring on a small size scale. The transmission electron microscope (TEM) is a powerful and versatile instrument which permits characterization of materials[80, 79, 81]. It offers variety of information obtained from different modes such as bright field (BF) and dark field (DF) imaging, selected area diffraction (SAD) and high resolution lattice imaging (HREM). BF and DF imaging are used to characterize defects and domain structures. SAD with combination of tilting of crystal in the microscope allows reconstructing the reciprocal space and in that way obtain information about the crystal structure and identifying different phases. HREM allows under certain conditions to directly visualize the projected crystal potential. The first TEM was built by two German scientists, M. Knoll and E. Ruska, in 1932 [82]. Nowadays, TEMs have become widely available.

In a TEM, a high-energy (~ 200 keV) electron beam is transmitted through the specimen. During transmission, the electrons interact with the specimen, giving rise to signals containing information about the internal structure and chemistry of the specimen. Electron diffraction patterns and lattice images are two forms of data which give an insight of crystallographic information in TEM. Lattice images are interference patterns between the direct beam and diffracted beams, viewed in direct space, and are obtained by high-resolution TEM (HRTEM) imaging. In the images, the spacing of a set of fringes represents the lattice spacing. If one looks at a more detailed manner, then the image or diffraction phenomena are aspects related to the scattering of incident electrons from the specimen atomic potentials. For direct information of defect structure on the atomic scale, an HRTEM is particularly useful with low spherical aberration coefficient(or corrected aberration coefficients), given that this is the typical spacing between atoms in solids [80].

In selected area diffraction pattern(SAED), the sample is illuminated with a parallel electron beam to ensure the focusing of the transmitted and diffracted beam onto the back focal plane of the objective lens. A specific area of the sample is selected by an SAED aperture that is in an *image plane* conjugate with the sample in the electron optic system of the TEM. The inserted SAED aperture creates a virtual aperture in the sample plane, giving a selected area that is about $0.4 \mu\text{m}$ or greater, in diameter[79]. A few hundred nanometers is therefore the typical lateral size of the region sampled by SAED in TEM.

Instrumentation

A transmission electron microscope consists of an illumination system, specimen stage and imaging system analogous to a conventional light microscope. A schematic diagrams of illumination section, sample stage and imaging section is shown in Figure 2.3(a). An electrostatic lens in the form of Wehnelt cup is used after the filament to converge the maximum number of emitted electrons. Illumination section consists of electron source, acceleration column and condenser lenses. The role of the illumination system in TEM is to project an electron beam on the part of the specimen that is observed. In this thesis, most of the TEM measurements have been carried out using JEOL 2010 TEM operating at 200 keV with LaB₆ thermionic emission type gun. Here, high voltage is generated in a separated power supply unit using Cockcroft-Walton technique and is coupled to the acceleration column. Following the acceleration column, condenser lens system is available. Electrons are generated in the electron gun by thermionic emission. (Any material that is heated to a high enough temperature will emit electrons when they have enough energy to overcome the work function according to $J = AT^2 e^{-\frac{\phi}{kT}}$, (where ϕ is the work function, J is the current density at the tip and A is the Richardson's constant). After leaving the electron gun the electrons are accelerated towards the anode and enter the column. Since the velocity of the electrons close to the speed of light the wavelength of the electrons has to be corrected for relativistic effects:

$$\lambda = \frac{2m_0eE}{h^2} \sqrt{1 + \frac{eE}{2m_0c^2}} \quad (2.2)$$

For 200 keV electrons, λ is equal to 0.0025 nm. It accelerates towards the anode at the top of the column and focuses at the specimen with the condenser lenses. The function of the condenser lens system is to provide a parallel or convergent beam of electrons at the specimen surface. In practice, this is not possible and the beam always possesses a certain kind of convergence when imaging at high resolution, usually in the range of 1 mrad for LaB₆ emitters (for our machine, it is ~ 0.68 mrad). Using different size of condenser aperture one can change the illuminated area on the specimen. Just below the sample (2-5 mm), Objective lens (OL) is situated. The combination of intermediate and projector lenses do the final image magnification. After the objective lens, objective aperture and selected area diffraction aperture are placed (shown in (Figure 2.3(b),(c))). Finally the magnified image forms at phosphor screen. To record the image or diffraction pattern, photographic film and/or charge coupled

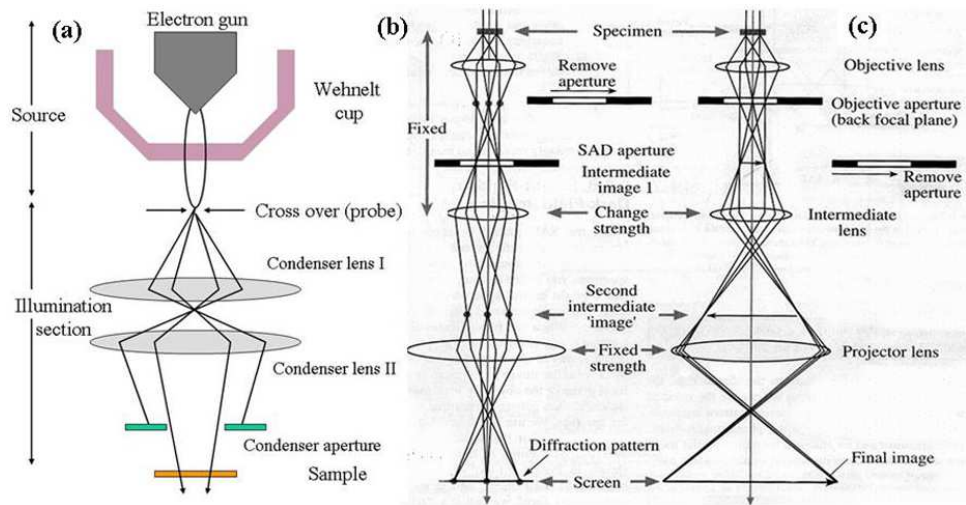


Figure 2.3: A schematic diagram of (a) Filament and illumination part, (b) Diffraction pattern formation and (c) Image formation [79].

device (CCD) can be used. The light generated on the phosphor screen is channeled to the CCD through the optical fiber and the CCD output is connected to the computer using image processing system. As electron is very highly interacting particle, the vacuum maintained inside the column of TEM, is 10^{-8} mbar. Three parameters are important for the best TEM imaging: the brightness, source size and energy spread of the electrons. The brightness is defined as the current density per solid angle and is conserved when the beam passes an (ideal) electron lens. Accelerating the electrons results in a less diverging beam and increases the brightness. The source size is the area from where the electrons seem to originate. Due to some electron-optic effects the source size is not always equal to the actual emitting area on the tip and is then referred to as the virtual source size. High resolution TEM demands for a planar coherent electron wave, since high-resolution images are formed by phase contrast.

Interaction of electrons with the specimen

After entering the specimen most of the electrons are elastically scattered by the nuclei of the atoms in the specimen. Some electrons are inelastically scattered by the electrons in the specimen (figure 2.4). Compared to X-ray or neutron diffraction the interaction of electrons with the specimen is huge and multiple scattering events are common. For thick specimens at lower resolutions an incoherent particle model

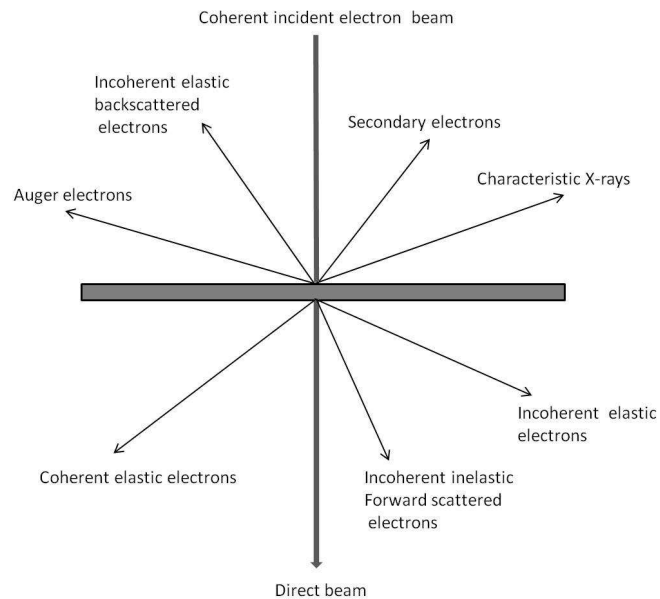


Figure 2.4: A schematic diagram of different processes taking place during electron–solid interaction.

can describe the interaction of the electrons with the specimen. However, with thin specimens at high resolution, this description fails because the wave character of the electrons is then predominant. The electrons passing the specimen near the nuclei are somewhat accelerated towards the nuclei causing small, local reductions in wavelength, resulting in a small phase change of the electrons. Information about the specimen structure is therefore transferred to the phase of the electrons. For the formation of high resolution images, only the elastically scattered electrons are of importance. The inelastic scattered electrons contribute mostly to the background of the image. The energy loss spectrum of the inelastic scattered electrons contains valuable information of the chemical composition of the specimen. This information can be extracted by observing the electron energy loss spectrum (EELS). The details of EELS will be discussed later in this chapter. The inelastic scattered electrons also produce Kikuchi lines in the electron diffraction pattern that is helpful for accurate crystallographic alignment of the crystals in the specimen.

Imaging and Diffraction

The conventional TEM image formation for thick specimen is very similar to the projector principle. In this case, an incoherent particle model can describe the interaction of the electrons with the specimen. Specimen contains variation in thickness and density. So the electrons will lose more energy when it transmits through the thicker and denser region and hence it will appear as darker object. Same way, the thinner and rarer region will appear as brighter object. This is called thickness contrast imaging. Contrast in TEM also depends upon the crystallinity of the specimen known as *diffraction contrast*. However, for thin specimen at high resolution, this description fails because the wave nature of the electrons is then predominant. If the specimen is thin enough and crystalline, then elastic scattering is usually coherent and these electrons now contribute to the image formation. After the exit of electrons (elastically transmitted coherent electron beams), the diffraction spots and image are used to form at back-focal plane and image plane of OL, respectively. The diffraction pattern can be understood by taking the Fourier transformation (FFT) of the wave function of electron at the back focal plane of OL. One more time FFT of this wave function at back focal plane of OL gives the high resolution (HR) lattice image. The HR image will form due to interference between the direct and diffracted beams depending on the phase difference between these two. So the highly diffracted beams are used to cut down by the objective aperture. The resolution and the details of image formation are governed by the contrast transfer function (CTF).

To retrieve structural information of the specimen from the micrographs it is necessary to calculate the trajectory of the electron wave through the specimen. In the kinematical approximation, multiple scattering of the electrons in the sample is ignored resulting in an undisturbed central beam. This approach already fails at a small thickness or a single atom. In dynamical calculations all the scattered beams and their mutual exchange of intensity during the course of multiple scattering in the specimen are taken into account. It is possible to do full dynamical calculations but these are soon limited by the available computing power. Using the fact that the vast majority of the electrons are scattered in a forward direction with small diffraction angles Cowley and Moodie devised the multislice approximation[83].

In this thesis work, two kinds of TEM systems have been used. Majority of HRTEM and *in situ* has been carried out using JEOL 2010 TEM operating at 200 keV (Fig. 2.5). The OL pole piece is an ultra high resolution pole piece (UHR-URP22) with a

spherical aberration coefficient (C_s) of 0.5 mm, which helps to achieve a point-to-point resolution of 0.19 nm. For imaging as well as real-time studies, a charge-coupled-device (CCD) based detector with 40 ms time resolution and with 4008×2672 pixels (Model 832, Gatan Inc.) has been used. In this thesis work, STEM, Electron energy loss spectroscopy (EELS) and EDS were carried out with 300 keV electrons in the Cs-corrected FEI Titan 80/300 system at the University of Bremen, Germany. The probe diameter was 0.2 nm during HAADF and STEM-BF mode.

Sample preparation

Sample preparation is the most important part of the TEM characterization. As the electrons transmit through the specimen, the specimen has to thin down to the electron transparency (< 100 nm) for conventional TEM and even lesser (< 10 nm) for HRTEM. There are two types of samples to be prepared depending on the interest of study. Cross-sectional TEM (XTEM) sample is required to probe the interface and/or bulk solid while planar TEM specimen preparation is required to probe the surface morphology.

Figure 2.6 and 2.7 show the schematic diagrams of one of the methods to prepare both planar and cross sectional TEM sample preparation respectively.

Planar specimen

For Planar TEM sample preparation, we cut the sample into 3 mm disc using ultrasonic disc cutter and thin down to ~ 100 nm using the South Bay Technology (SBT) made lapping and polishing system (LPS-Model-910). Here, the mechanical thinning starts with a rough emery paper with larger grit size and ends with an emery paper with finer grit size. Then the specimen is again thinned (down to 30-40 μm) and polished by diamond paste and alumina suspension in Gatan made dimple grinder (DG) system (model 656). In this process, the edge remains thicker but center part becomes dimpled. The final electron transparency is achieved by ion milling with the Gatan made precision ion polishing system (PIPS) (model 691). During PIPS, 3.5 keV Ar ion beam is used to sputter the material from the specimen in grazing incidence (4° - 7°) (Fig. 2.6).

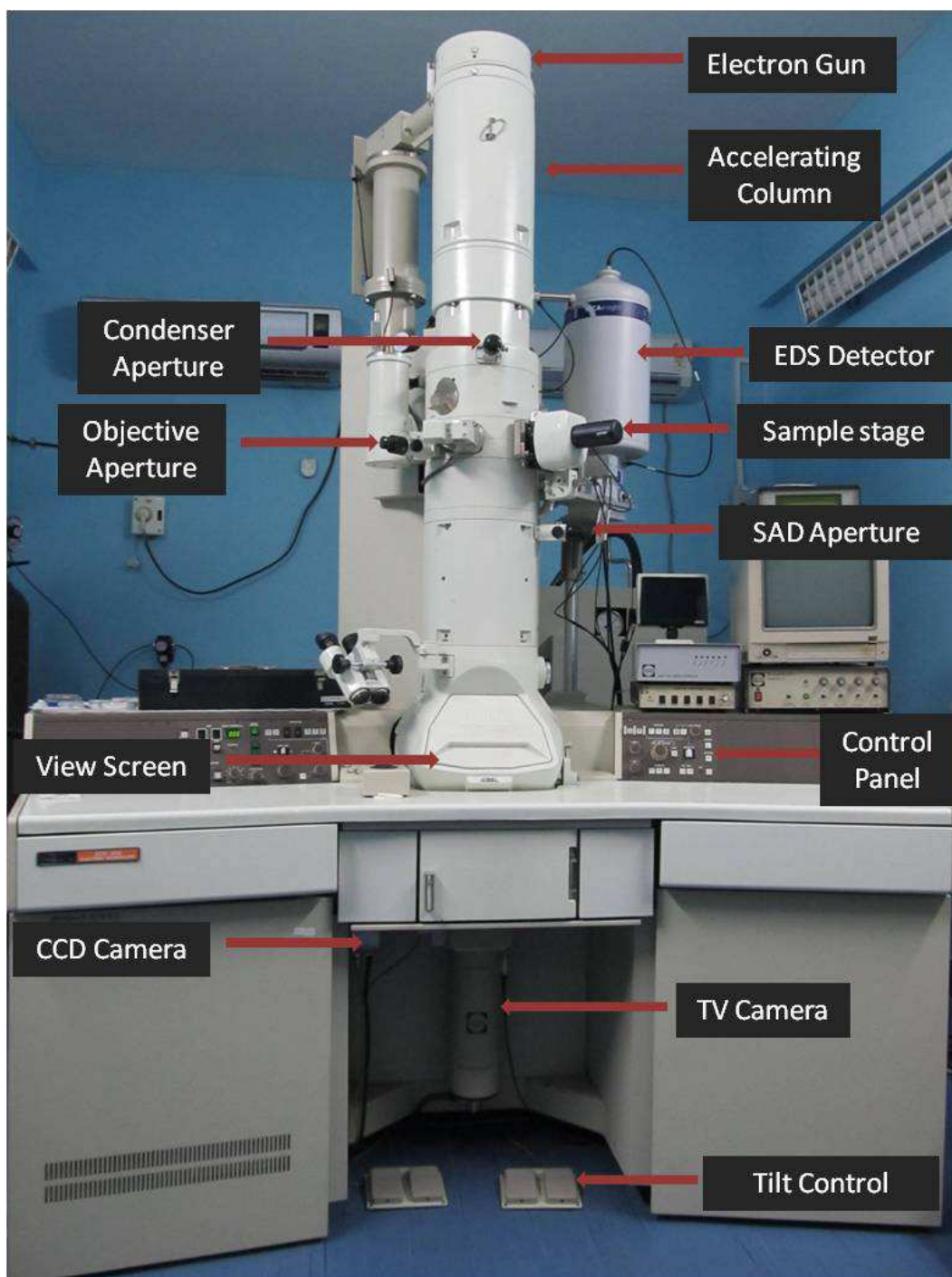


Figure 2.5: 200 keV JEOL HRTEM installed at Institute of Physics, Bhubaneswar.

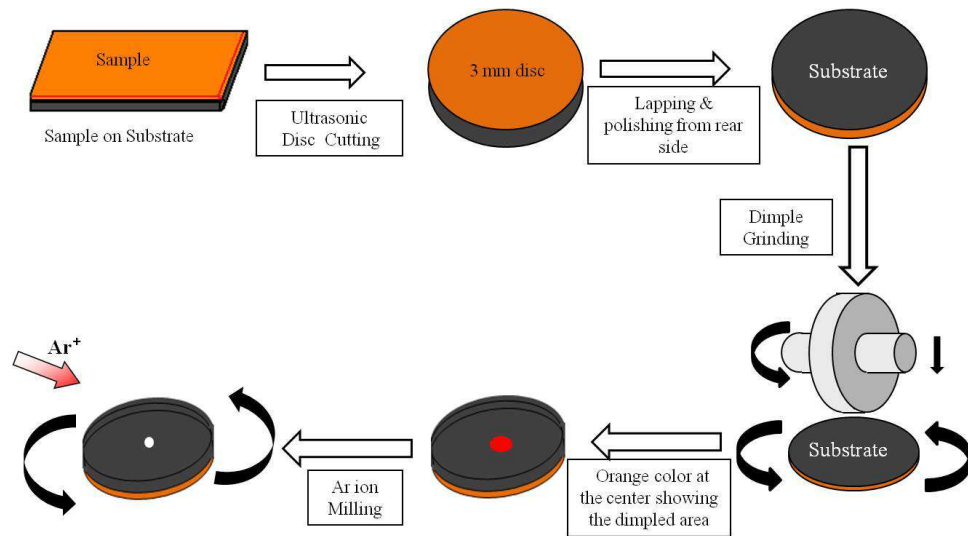


Figure 2.6: A schematic diagram of procedure to prepare a typical planar TEM specimen.

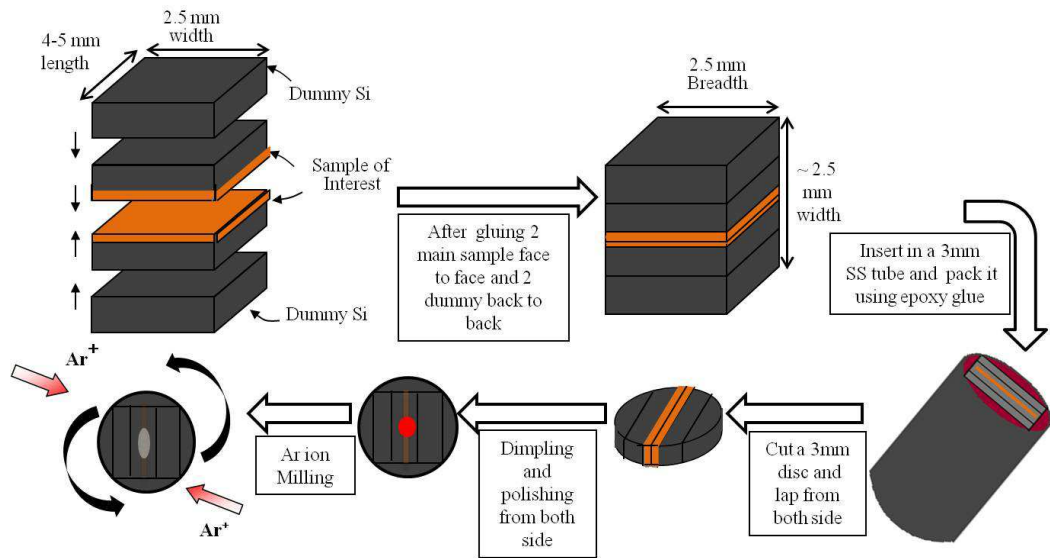


Figure 2.7: A schematic diagram of procedure to prepare a typical cross-sectional TEM specimen.

Cross-sectional specimen

For Cross-sectional TEM sample preparation, we cut the as deposited sample into two rectangular pieces of size (2.5×3) mm² each using SBT made Abrasive Slurry saw (model 850). Then the pieces were glued face to face using Gatan G1 epoxy as thin as possible. It will ensure an optimal ion milling rate i.e. if the glue quantity will be too high, the ion mill will remove it quicker than the sample resulting a sharp hole with a sharp edge, opaque to electron beam. Again the above assembly is glued with two silicon dummy pieces with similar dimensions. Then it was put in stainless steel tube having inner and outer diameter 2.5 mm and 3 mm respectively. Then we made a 1 mm slice out of it using SBT made Low speed diamond wheel saw (model 650). After that the mechanical thinning (using LPS and dimple grinder) was done followed by 3.5 keV Argon ion milling to make it electron transparent. We repeated the procedure for thinning as required for planar specimen. But in this case one needs to perform those steps for both sides of the sample excluding dimpling for one side. The procedure of cross-sectional specimen is depicted pictorially (Fig. 2.7).

Hot-stage holder

Many phenomena occur at elevated temperatures and they are of fundamental interest. The use of specimen heating during TEM observation allows the possibility to study direct phase transformations, such as nucleation and growth, dissolution processes etc. *In-situ* TEM is a powerful method to observe phase transformation, order-disorder phenomenon in nano materials by varying specimen temperature. In this thesis work, *in-situ* experiments have been done by using Model 628 UHR *single tilt heating holder* procured from Gatan. Inc. It is custom designed to fit small high resolution pole piece gaps. This is associated with a Model 901 smart set hot-stage controller. It is a side entry furnace type single tilt holder, where the specimen can be heated up to 1000°C, accurate to a couple of degrees (Figure 2.8).

The furnace (made up of tantalum) is mounted on the spring loaded 3 insulating ceramic mounts which accommodate expansion or contraction during heating or cooling. Tantalum is used, because of its high temperature stability and resistance to solid state welding to most technical materials including silicon. The furnace contains a miniature encapsulated heater that is spot welded to two terminal posts in the specimen tip. Both sides of the heater circuit are connected via copper wires to a 5 pin

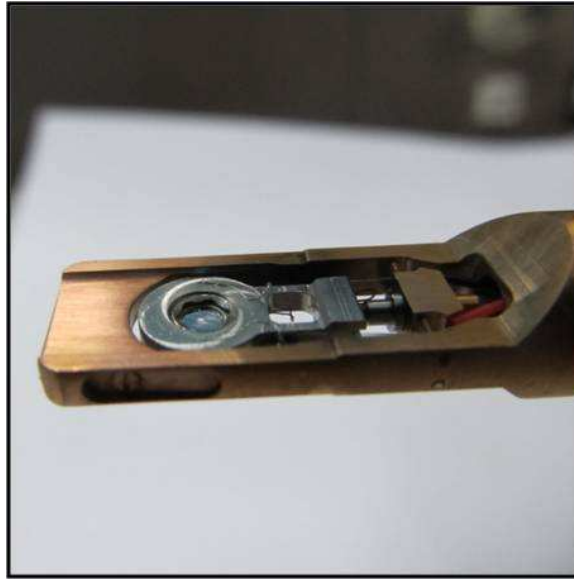


Figure 2.8: Single tilt hot stage holder installed at IOP, Bhubaneswar (Model 628, Gatan, Inc.).

vacuum feed-through, mounted at the end of the specimen rod. The temperature is measured by platinum-rhodium thermocouple, spot welded to the furnace body. The thermocouple leads are anchored by terminals in the specimen tip and are then fed along the axis of the specimen rod to the five pin vacuum feed through. Above 500°C , the water circulation automatically starts driven by the controller. Recirculation of distilled water from a stainless steel tank to the heating holder is performed through two polyurethane tubes of length 260 cm each. Water cooling basically helps in extending the operating range and to reduce the specimen drift by maintaining a local constant temperature heat sink.

2.3.2 FIB-SEM-Cross beam system

The combination of field emission scanning electron microscopy (FESEM) and focused ion beam (FIB) is a future key technology for semiconductor and material science related applications. A scanning electron microscope (SEM) is a microscope that uses electrons instead of light to form an image. Since their development in the early 1950's, scanning electron microscopes have developed new areas of study in the medical and physical science communities. The focused ion beam (FIB) technique was mainly developed during the late 1970s and the early 1980s. Modern FIB systems are

becoming widely available in semiconductor research and processing environments, as well as in failure analysis and chip-design centers. The technology enables localized milling and deposition of conductors and insulators with high precision, hence its success in device modification, mask repair, process control and failure analysis and also the preparation of specimens for transmission electron microscopy (TEM).

The experimental setup used for this thesis work is a cross-beam system coupling a Carl Zeiss, Neon 40 scanning electron microscope (SEM, Gemini Column) and a Canion 31 focused ion beam (FIB, Orsay Physics), equipped with gas injection system (GIS, Orsay Physics), STEM detector, Four Quadrant Back scattered electron detector (Carl Zeiss) and EDS detector (INCA, Oxford) [figure 2.9]. The two beams are focused on the same point of the sample. Both beams coincide at a crossover point 5 mm below the objective lens of the SEM. The working distance (WD) for the FIB in this coincidence point is 12 mm. The geometrical layout and arrangement of the two columns enables perpendicular tilt of the sample to the ion beam in the coincidence point. To provide full eucentric tilt at all operating conditions a 6-axis motorized eucentric specimen stage is used. This allows real time simultaneous FIB machining and non-destructive non-contaminating SEM imaging at high resolution. The sample may be tilted between 0° and 54° to face perpendicularly the ion or the electron beam. At 0° tilt, imaging at normal incidence with the electron beam is possible while at 54° , imaging and machining with the FIB is performed. Both imaging techniques are based on the collection of secondary electrons. The FIB column operates at an accelerating voltage of Ga^+ ions ranging from 2 to 30 kV with a minimal Gaussian beam diameter around 7 nm. The beam current can be varied from 1 pA for the lowest current to 50 nA. Our FIB system can be used for imaging, milling and deposition (using Gas Injection System). One Kleindiek Micromanipulator is attached inside the specimen chamber for TEM lamella preparation (for lift out). The system is fitted with a computer controlled gas injection system that can handle up to five different gases for metal and insulator deposition or enhanced and selective etching. The GIS (Gas injection system) is composed of five distinct lines for gas injection. Gas flows from a reservoir through a capillary. Temperature of reservoirs and capillaries are independently controlled. The needles at the end of the capillaries are mounted on a micro stage table. Thus they can be precisely positioned close to the working area ($< 100 \mu\text{m}$) in order to create a local high gas pressure. A turbo molecular pump ensures

a dynamic pumping and the base pressure in the chamber is 10^{-6} mbar. To avoid damages and contamination by Ga^+ ions, all the tunings such as focus and alignment can be systematically performed in the neighborhood of the working area. Our cross beam system can also be used for both e-beam and ion beam lithography (ELPHY Quantum lithography system, Raith).

Now, we discuss the working principle of SEM and FIB individually.

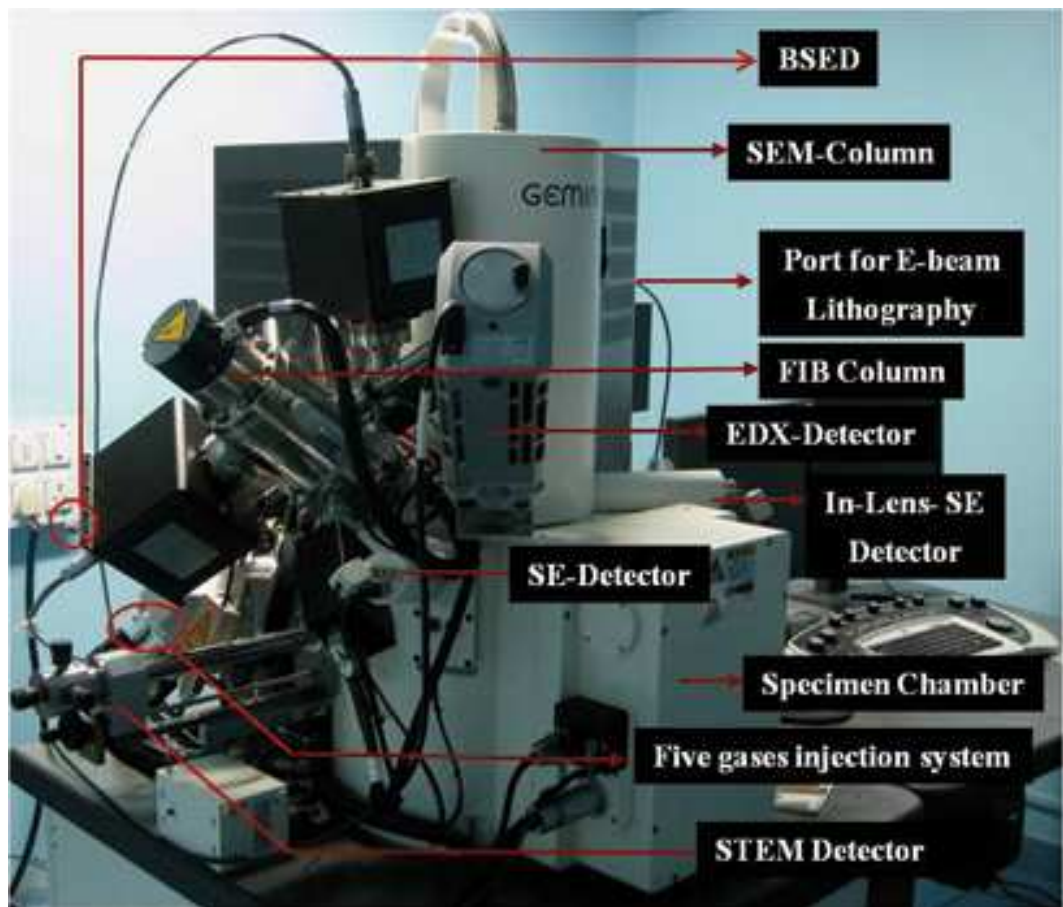


Figure 2.9: FIB-SEM crossbeam system installed at Institute of Physics, Bhubaneswar.

Scanning Electron Microscopy (SEM)

The microscope used in this work is a Zeiss Neon 40. This microscope is equipped with a field emission gun, GEMINI electron-optics, a lateral secondary electron (SE) detector (*Everhart-Thornley*), a backscatter detector, an in-lens SE detector. The

main characteristic of the GEMINI optics is the use of a beam booster and an objective lens which acts as a combined electrostatic/electromagnetic lens. The electrons generated at the gun tip are accelerated to the set acceleration voltage as they are accelerated towards the anode. However, the beam booster, which is installed directly after anode, is always at a potential of an extra 8 kV when the set acceleration voltage is ≤ 20 kV. When low voltages are used, this arrangement will ensure that the energy of the electrons in the beam path will always be 8 kV higher than the set acceleration voltage and will reduce the influence of magnetic stray fields on the electron beam. Before the electron beam exits the objective lens, the electrostatic lens reduces the potential by an opposite applied 8 kV. The main advantage of this technique is that a stable beam is obtained even at low acceleration voltages. In addition to acting as a retardant towards the electrons ejected from the electron column, the electrostatic lens will act as a collector for the electrons generated at the sample surface. The sample electrons are accelerated and focused back up the beam path, where the in-lens SE detector is positioned (annular detector). The combination of the electrostatic lens and the in-lens detector results in a very high detection efficiency for the in-lens detector even at low (< 1 kV) acceleration voltages [88].

Image Formation

Image formation in the SEM is dependent on the acquisition of signals produced from the electron beam and specimen interactions. These interactions can be divided into two major categories: elastic interactions and inelastic interactions. Elastic scattering results from the deflection of the incident electron by the specimen atomic nuclei or by outer shell electrons of similar energy. This kind of interaction is characterized by negligible energy loss during the collision and by a wide-angle directional change of the scattered electrons. Incident electrons that are elastically scattered through an angle of more than 90° are called backscattered electrons (BSE), and yield a useful signal for imaging the sample. Inelastic scattering occurs through a variety of interactions between the incident electrons and the electrons and atoms of the sample, and results in the primary beam electrons transferring substantial energy to that atom. The amount of energy loss depends on whether the specimen electrons are excited singly or collectively and on the binding energy of the electron to the atom. As a result, the excitation of the specimen electrons during the ionization of specimen atoms leads to the generation of secondary electrons (SE). In addition to those signals

that are utilized to form an image, a number of other signals are produced when an electron beam strikes a sample, including the emission of characteristic x-rays, Auger electrons and cathodoluminescence (figure 2.10). Basically, when primary electrons interact with the sample, the primary electrons cause either secondary electrons (SE's) or backscattered (BSE's) to be emitted from the sample, which are mainly used for image formation. As a result of inelastic interactions of the primary electrons with the sample, the secondary electrons are emitted from the sample with energy less than 50eV [89]. The energy distribution of the backscattered electrons has a peak just below the primary electron energy and a tail towards zero. As the secondary electrons are lower in energy than the backscattered electrons, they can be separated from the high energy backscattered electrons with an electric field. Because of the low energy of the secondary electrons, they only escape from the topmost layers of the sample and hence carry information from these layers. A secondary electron image thus gives information about the topography of the sample. The higher energy backscattered electrons can escape from deeper in the sample. The number of backscattered electrons depends on the atomic number of the sample. Hence a backscatter electron image gives information about the composition of the sample.

Most commonly an *Everhart-Thornley* detector (E-T detector) is used to detect the electron signals in the scanning electron microscope. The E-T detector consists of a Faraday cage covering a scintillator, a light guide and a photomultiplier. The Faraday cage is placed outside the detector and either a negative or a positive bias voltage can be applied to it. When a negative bias voltage is applied, all secondary electrons are rejected and hence only the backscatter signal is detected. When a positive bias voltage is applied to the Faraday cage, the secondary electrons are attracted to the detector. The positive bias voltage causes the trajectory of electrons emitted from the sample over a large solid angle to be deviated towards the detector. In the detector the electrons are accelerated to the scintillator where they induce light emission. The light is guided to the photomultiplier tube amplifying the signal and converting it into an electric current which can be read out on a screen.

Focused Ion Beam (FIB)

The structure of the column is similar to that of a scanning electron microscope, the major difference being the use of a gallium ion (Ga^+) beam instead of an electron beam. A vacuum of about 1×10^{-7} mbar is maintained inside the column. The basic

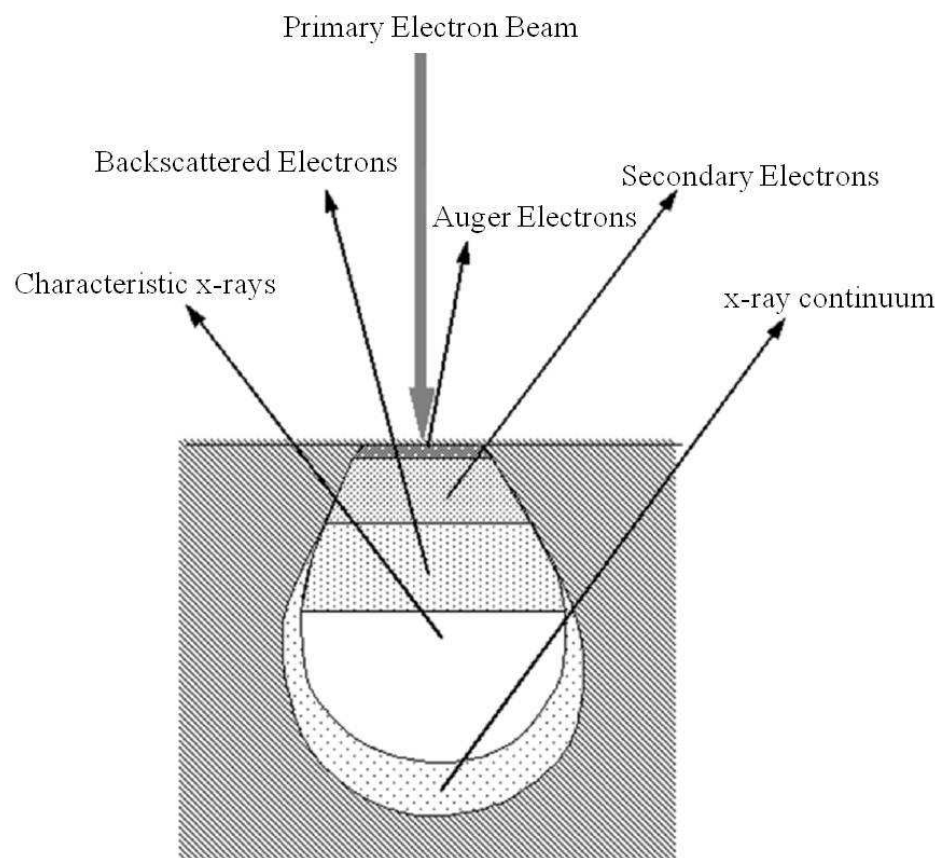


Figure 2.10: A schematic diagram of different processes taking place during electron–solid interaction

components of a FIB system are normally an ion source, an ion optics column, a beam deflector and a substrate stage. The ion beam is generated from a *liquid-metal ion source* (LMIS) by the application of a strong electric field. This electric field causes the emission of positively charged ions from a liquid gallium cone, which is formed on the tip of a tungsten needle. A typical extraction voltage is 7000 V. The extraction current under normal operating conditions is $2\mu\text{A}$. After a first refinement through the aperture, the ion beam is condensed in the first electrostatic lens. The upper *octo pole* then adjusts the beam stigmatism. The ion beam energy is typically between 2 and 30 keV, with beam currents varying between 1 pA and 50 nA. Using the variable aperture mechanism, the beam current can be varied, allowing both a fine beam for high-resolution imaging on sensitive samples and a heavy beam for fast and rough milling. Blanking of the beam is accomplished by the blanking deflector and aperture, while the lower *octopole* is used for raster scanning the beam over the sample in a user-defined pattern. In the second electrostatic lens, the beam is focused to a fine spot, enabling a best resolution in the sub 10 nm range. All operations such as manipulating the stage, controlling valves for gas delivery, turning on and off pumps and manipulating the ion beam are carried out via software. A system of vacuum pumps is needed to maintain the vacuum inside the column and the work chamber. A rotary pump is used in combination with a turbo pump for pumping the work chamber. The ion column is additionally provided with one or two ion pumps.

2.3.3 Electron Backscatter Diffraction Technique (EBSD)

The *electron backscatter diffraction* (EBSD) is an additional characterization technique to SEM which provides quantitative micro structural information about the crystallographic nature of the inorganic crystalline materials such as metals, minerals, semiconductors and ceramics. It reveals size and orientation of grains, grain boundary character, texture and phase identity of the sample under the beam.

EBSD patterns are generated on the phosphor screen by backscattered diffraction of stationary beam of electrons (with energy 10 - 30 KeV) from the crystalline material. When the primary beam interacts with the crystal lattice, low energy loss backscattered electrons are channeled and subjected to path differences which leads to form a diffraction pattern by constructive and destructive interference. The diffraction pattern consists of kikuchi bands in which the band width is related to many parameters such as electron energy, working distance etc. Electron backscattered pattern

(EBSP) is analyzed with a stationary beam on a point on the sample. It is uniquely defined by the parameters such as lattice parameters of the particular crystal, its orientation in space, the wavelength of the incident electron beam and the proximity of the EBSP detector to the sample. Specialized computer software analyzes the EBSP by detecting a number of Kikuchi bands using an optimized *Hough transform*[90]. The software determines all possible orientations with each phase and reports the best fit as the identified phase and orientation, which helps in indexing the EBSP. EBSD mapping can be performed by considering the phase and orientation at each pixel and the sampling step size between points with the use of basic RGB coloring scheme. For example, In inverse pole figure (IPF)for cubic phases, full red, green and blue are assigned to grains whose $\langle 100 \rangle$, $\langle 110 \rangle$ and $\langle 111 \rangle$ axes respectively, are parallel to the surface-normal direction, where as for intermediate orientations, colors are assigned by an RGB mixture of the primary components. EBSD data processing software can generate an enormous variety of additional visual and analytical information, including overall preferred orientation (texture), distribution of grains in specific orientations, phase distribution and distribution of grain boundaries. Details about various aspects of EBSD technique can be found in reference [91].

2.3.4 Scanning Transmission Electron Microscopy (STEM)

In STEM, the image formation process is completely different. The probe is sharply focused onto the specimen plane with a diameter in the sub-nanometer range. The signal on the (ring-shaped) high angle annular dark field (HAADF) detector comes from electrons scattered to large angles well above 30 mrad. Local information is finally retrieved by mapping the HAADF signal against the position of the probe. Therefore, the probe is rastered over the specimen. The single most important feature of a STEM instrument is its versatility: atomic resolution images, diffraction patterns from nanometer regions and nanometer scale spectroscopy data can be obtained either simultaneously or sequentially from the same region of the specimen [92, 93].

High Angle Annular Dark Field Imaging (HAADF)

The HAADF detector is an annular detector of scintillator material coupled to a photomultiplier tube. The main difference between TEM-DF mode and STEM-DF mode is that, in TEM case, only a fraction of scattered electrons are allowed to enter the objective aperture, where as in STEM, the images are formed by collecting most

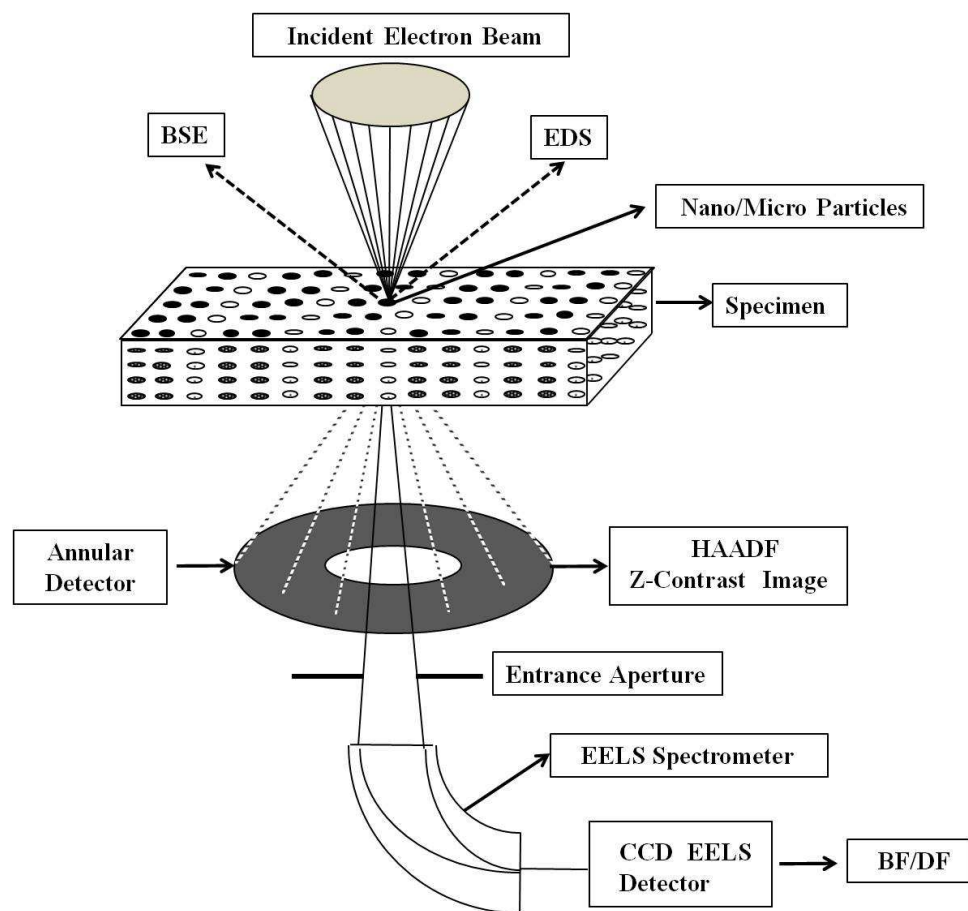


Figure 2.11: Schematic diagram of detector geometry for a STEM [94].

of the electrons on the annular dark field (ADF) detector. In case of HAADF, the inner and outer radius are larger than the ADF which detects the electrons that are scattered to higher angles and contribution of incoherent Rutherford scattering makes the images less noisy. These radii can both vary over a large range, but typically the inner radius would be in the range of 30–100 mrad and the outer radius 100–200 mrad. Here, the contrast depends on Z^2 of the material. So, HADDF imaging is also called *z-contrast imaging*. As the scattering angle increases, the scattered intensity from an atom approaches the Z^2 dependence that would be expected for Rutherford scattering from an unscreened Coulomb potential. In practice, this limit is not reached and the Z exponent falls to values typically around 1.7 [95] due to the screening effect of the atom core electrons. This sensitivity to atomic number results in images in which composition changes are more strongly visible in the image contrast than the high-resolution phase-contrast imaging. As the center of the detector is a hole, electrons below the inner radius can pass through the detector for use either to form a BF image or to form an electron energy-loss spectrum (figure 2.11).

X-ray Energy dispersive spectroscopy(XEDS)

An incident electron is inelastically scattered at an atom of the specimen and excites, say, a core electron. An electron from a higher orbital fills the empty states in lower orbital. The energy difference is released in form of photons (when the core level electron of high enough atomic number is knocked out, the emitted photons would be in the X-ray regime), whose energy is characteristic for the transition in the respective target atom. The X-rays are detected spectrally resolved (the number of counts in a given energy width of typically few eV/channel) with an appropriate energy dispersive detector, like Si(Li) or SDD (silicon drifted detector). To create an elemental map, an EDX spectrum is recorded for each scan point in STEM mode. The energy windows can be selected around certain spectral peaks, so that the respective peak intensity can be mapped against the position of the STEM probe. In this thesis, both the STEM based and SEM based energy dispersive spectrometry (EDS) measurements were used.

Electron energy loss spectroscopy(EELS)

Another method to investigate the chemical composition of a material is electron energy loss spectroscopy (EELS). It is the analysis of the energy distribution of the

electrons emanating from the sample. The principle of signal development is as follows: An incident electron is inelastically scattered by an atom of the specimen, for example, it excites a core electron of an atom in the specimen. This energy loss is characteristic for the scattering atom and can thus be used for elemental analysis. To measure the energy loss, an imaging filter such as, post-column Gatan Image Filter(GIF), has been used which works roughly as follows: Electrons transmitted through specimen will pass the magnetic prism, where they are dispersed according to their energy loss by the Lorentz force. Finally, a CCD camera detects the electrons. An energy-selecting slit may be inserted to select electrons that have suffered a certain energy loss (energy window). By applying a potential to the drift tube the energy window can be selected. A sequence of lenses is then used to form an image using these electrons in the so-called energy-filtered TEM (EFTEM) mode. In *spectroscopy mode*, the spectral energy distribution of the electrons can be visualized. It can provide information on the electronic structure, oxidation states and chemical composition on an atomic or sub nanometer scale (figure 2.11). The combination of XEDS and EELS with HAADF imaging technique can provide detailed information on the composition, chemistry and electronic and crystal structure of nano scale systems with atomic resolution and sensitivity.

In this thesis, STEM, Electron energy loss spectroscopy (EELS) and EDS were carried out with 300 keV electrons in the Cs-corrected FEI Titan 80/300 system at the University of Bremen, Germany. The probe diameter was 0.2 nm during HAADF and STEM-BF mode.

2.3.5 Rutherford Backscattering Spectrometry

Rutherford Backscattering Spectrometry (RBS) is an analytical technique used to determine the structural and compositional details of a material by analyzing the backscattered high energy ions. It is based on classical scattering in a central-force field. Aside from the accelerator, which provides a collimated beam of MeV particles (usually He^+ or He^{++} ions), the instrumentation is simple. Semiconductor nuclear particle detectors are used that have an output voltage pulse proportional to the energy of the particles scattered from the sample into the detector. The technique is also the most quantitative, as MeV Helium ions undergo close-impact scattering collisions that are governed by the well-known Coulomb repulsion between the positively

charged nuclei of the projectile and target atom. More about various aspects of RBS technique can be found in ref.[97].

Kinematic factor

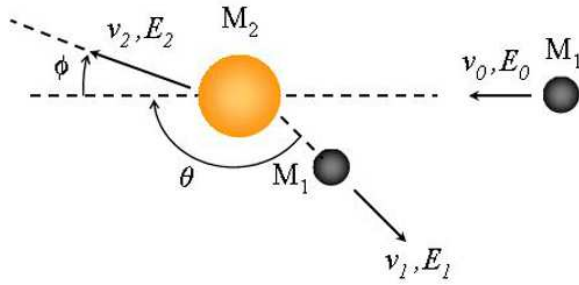


Figure 2.12: A schematic diagram of the interaction of two particles [97].

The ratio of the projectile energy after a collision to the projectile energy before a collision is defined as the kinematic factor (K_{M_2}). When a projectile with mass and energy M_1 and E_0 collides elastically with a stationary particle (target atoms) of mass M_2 ($M_2 > M_1$), energy will be transferred from the projectile to the target atoms. If the projectile energy (E_0) is much larger than the binding energy of the target atoms, but less than the energy required for nuclear reactions and resonances, then the kinematic factor for this system shown in figure 2.12 can be expressed as:

$$K_{M_2} = \frac{E_1}{E_0} = \left[\frac{M_1 \cos\theta + (M_2^2 - M_1^2 \sin^2\theta)^{1/2}}{M_1 + M_2} \right]^2 \quad (2.3)$$

Thickness analysis

In a real experiment, instead of particle-particle collision, a beam of light positive ions (He ions or protons) are incident upon a target material. Relative number of backscattered ions from a target atom that are directed towards a certain solid angle $d\Omega$ is termed as differential scattering cross section.

$$\frac{d\sigma}{d\Omega} = \frac{1}{Nt} \frac{dQ/d\sigma}{Q} \quad (2.4)$$

where N is the atomic density of the target atoms and t is its thickness. σ is called average differential scattering cross section and can be defined as,

$$\sigma = \frac{1}{\Omega} \int_{\Omega} \frac{d\sigma}{d\Omega} d\Omega \quad (2.5)$$

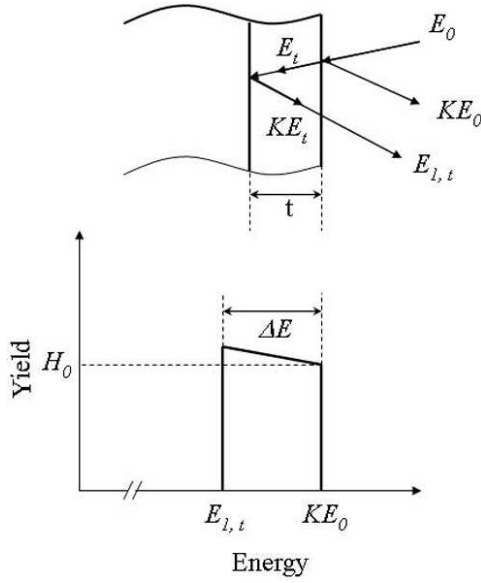


Figure 2.13: A schematic diagram of the RBS spectrum for a thin film [97].

and the differential scattering cross-section for an elastic collision between two atoms is given by Rutherford's formula,

$$\frac{d\sigma}{d\Omega} = \left[\frac{Z_1 Z_2 e^2}{4E_0} \right]^2 \frac{4}{\sin^4\theta} \frac{\left[1 - \left(\frac{M_1}{M_2} \sin\theta \right)^2 \right]^{1/2} + \cos\theta}{\left[1 - \left(\frac{M_1}{M_2} \sin\theta \right)^2 \right]^{1/2}} \quad (2.6)$$

where Z_1 and Z_2 are the atomic numbers of the projectile and target atom respectively. From the above equations, simple way get the thickness is dividing the term Nt by the atomic density N . In other words, the total no of detected particles can be written in terms of the height of the spectrum as $H_i = \sigma(E_i)QN.dt$, when the beam is falling normally onto the sample. Here, i denotes the number of equally smallest slabs for which backscattered energy can resolute, that means $t = i.dt$ and $\sigma(E_i)$ must be calculated at each backscattered energy E_i . Now, the total number of counts (area under the curve) is $A = \sum_i H_i$. In figure 2.13, H_0 denotes the total number of counts at energy KE_0 . So total no of counts is given by,

$$A = H = \sum_i H_i = \sum_i \sigma(E_i)\Omega QN.dt = \sigma\Omega QNt \quad (2.7)$$

The value of A can be obtained by taking the area under the spectrum.

Instrumentation

RBS instrumentation can be broadly divided into three parts: accelerator, target chamber and energy analyzer. In the first part, H or He ions are generated through ionization process. Then, these ions are accelerated using the accelerator upto an energy of 1–3 MeV. Selection of the required isotope is done by passing the beam through a mass analyzer. Finally, the collimated beam falls on the sample (target chamber). In the target chamber, a surface barrier detector (SBD) is used to detect backscattered projectiles kept at a very high angle ($\geq 150^\circ$). The sample is connected with the current integrator to get the total number of incident ions (total charge accumulated on the target). The energy related output from SBD goes through the energy analyzer. It consists of preamplifier, amplifier, analog to digital converter and multi channel analyzer (MCA). Finally, the output of MCA can be fed to the computer, where the resulting RBS spectrum can be stored. For the present thesis work, we have used 45° degree beam line of the 3 MV tandem Pelletron accelerator (9SDH2, NEC, USA) facility at IOPB [98]. Surface barrier detector was placed at 160° at a distance of about 11 cm from the sample holder. For the RBS measurements, 1.35 MeV He^+ ions were used and RBS simulation was carried by SIMNRA software package [99].

Chapter 3

Temperature-dependent electron microscopy study of Au thin films on Si(100)

3.1 Introduction

In this chapter, the variation in the temperature dependent behavior of gold nanostructures on Si(100) surfaces in presence and absence of native oxide layer are studied *in-situ* using a hot stage holder in high vacuum(HV) condition (inside TEM).

As the dimensions of electronic devices decrease with increasing packing density, the thickness of metal layers decreases continuously. An understanding of the growth of metal thin film on a semiconductor becomes important both from fundamental and practical points of view. The interaction of metal films with silicon has attracted considerable attention because of its importance in semiconductor technology. Metal nanoparticles on surfaces are being used effectively in nanofabrication, as catalysts for carbon nanotube growth [100, 101], catalysts for the vapor-solid-liquid (VLS) growth of inorganic nanowires [102, 103, 104], and for nano electronics applications [105, 106, 107]. Formation of nano-metal silicides, used as Schottky barriers and ohmic contacts in devices, is of particular interest in the emerging area of nanoscience and nanotechnology. The mechanism of these interactions, the range of temperatures required and the resulting composition of Au–Si alloy depends on whether these gold nano islands interact directly with the substrate or they will have to deal with a

barrier like native oxide layer before, they could interact with substrate. Either of the processes may give rise to various kinds of self assembled nano/micro structures depending on the symmetry of the substrate. The role of nanosilicides is important in many ways and hence a deeper understanding at atomic scale for the silicon/metal interfaces is indispensable [108]. Recently, fabrication of micro/nanoscale pits on Si substrates with long range ordering and reliable shape control via a facile vapor transport method assisted by Au nanoparticles has been achieved [109]. The resulted pits in the shape of triangles, squares and, wires were obtained on Si(111), (100) and (110) substrates, respectively [109]. How the desorption takes place to form regular shaped pits would be interesting to study. This paper addresses a part of this problem as we focus on the desorption of gold at high temperatures from the regular shaped gold silicide structures.

Self-assembly is an attractive nanofabrication technique because it provides the means to precisely engineer the structures on the nanometer scale over large sample areas. Self-organizing nano crystal assemblies have already shown the degree of control necessary to address the challenges of building nanometer-scale technologies [110]. A systematic study of such processes has implications on modern day semiconductor technology. Studies of processes going on at the Si/metal interfaces at low temperatures have been well attempted by several groups [110, 111, 112, 113, 114, 115, 116, 117, 118, 119]. Most of these studies were done under UHV conditions and on systems where there was no oxide layer in between the metal film and the silicon substrate. Many of them have reported the formation of various metastable gold silicides due to the inter mixing of silicon and metal. There have been numerous interesting studies on the mechanism of relaxation of strain in such epitaxial layers. Strained epitaxial layers are inherently unstable and have interesting properties. It has been reported that the dislocation formation and the shape transition are the important processes by which relaxation of strain occurs [26, 27, 28, 29]. In recent years, it has been recognized that shape changes such as island formation constitute a major mechanism for strain relief [26, 28]. Tersoff and Tromp reported that a strain-induced shape transition may occur [26]. Below a critical size, islands have a compact symmetric shape. For larger sizes, they adopt a long thin shape that allows better elastic relaxation of the island's stress [26].

Metal silicide thin films on Si(100) have been studied in great detail for more than two decades due to the possibility of obtaining self-aligned epitaxial metal-semiconductor interfaces [118, 27]. Sekar *et al.* [28, 29] reported the formation of silicide when a ≈ 100 nm Au film deposited on Br-passivated Si(111) was thermally annealed. The annealing treatment of the as-deposited Au/Si at eutectic temperature ($\approx 363^\circ\text{C}$) gave rise to silicide of composition close to Au_4Si as inferred from Rutherford backscattering spectrometry (RBS) studies. Mundschau *et al.* reported the formation of triangular islands, when sub monolayer gold was deposited epitaxially on Si(111) substrate under UHV conditions [120]. Vacuum annealing of thick and continuous gold films deposited on passivated Si(110) surface showed the formation of high aspect ratio gold silicides (Au_4Si) wire like structures around $\approx 363^\circ\text{C}$ [43]. Earlier, we showed the formation of well-aligned low aspect ratio gold silicide nanostructures that were grown under UHV conditions at temperatures in the range $600^\circ - 700^\circ\text{C}$ in the absence of native oxide at the interface [121, 122]. Using real time *in situ* high temperature transmission electron microscopy (with 40 ms time resolution), we showed the formation of high aspect ratio (≈ 15.0) aligned gold silicide nanorods in the presence of native oxide at the interface during *in situ* annealing of gold thin films on Si(110) substrates [123]. This was explained using an oxide mediated liquid-solid growth mechanism. For other substrate surfaces, such as Ni(100) substrate, homo- and hetero-epitaxial growth has been studied, in which E. Kopatzki *et al* have reported the formation of nickel nano squares/rectangles of average size 2 nm [124]. Similarly, Frank *et al* have reported the formation of rectangles/squares in the homo epitaxial system of Ag on Ag(100) substrate [125]. For gold on Si(100) substrates, a detailed study on the preferred orientation growth of gold under N_2 atmospheric conditions was carried out and found that structures reorient themselves at higher temperatures [126]. The knowledge of real time shape variations and structural phase transitions in Au/Si system would help to properly understand silicide growth at nano scale and would form a basis for appropriate applications that are based on the use of gold silicide islands as catalysts. As the Si(100) substrate is used for many electronic applications in semiconductor industry, it will be very useful to understand nucleation, growth of gold silicide nanostructures and desorption as a function of temperature.

In this chapter, we present the experimental observation of the growth of aligned gold

silicide nano-structures during *in-situ* thermal treatment in a TEM heating stage for gold deposited on Si(100) surfaces with and without an oxide layer at the interface. Followed by this, *ex-situ* STEM measurements and high resolution electron microscopy measurements confirm the presence of gold in these rectangular shaped silicide structures and also show depletion of gold due to desorption of gold silicide at high temperatures[127].

3.2 Experimental methods

A thin Au film of thickness ≈ 2 nm was deposited on n-type Si(100) of resistivity 10–20 Ω cm, by the molecular beam epitaxy (MBE) method under UHV (base pressure 2×10^{-10} mbar) conditions [128]. The Si(100)substrates were loaded into the MBE chamber and degassed at 600°C for about 12 hours inside the chamber, followed by flashing for about ~ 2 minutes by direct heating at a temperature of 1200°C. In this process, native oxide was removed and a clean Si(100) surface was obtained. On such ultra clean surfaces, ≈ 2.0 nm thick gold films were grown epitaxially by evaporating Au from a Knudshen cell. Deposition rate was kept constant at ≈ 0.14 nm min⁻¹. During the growth, the chamber vacuum was 6.2×10^{-10} mbar. The thickness monitor was calibrated with RBS measurements. After the deposition, the sample was taken out of MBE chamber. We have also deposited Au films of about 5.0 nm thickness on n-type Si(100), by the thermal evaporation method under high vacuum (4×10^{-6} mbar) conditions. For this case, native oxide was kept intact and the thickness was monitored using a quartz crystal monitor. Planar TEM specimens were prepared from the above samples. Disks of ≈ 3 mm diameter were cut using an ultrasonic disc-cutter followed by lapping until it reached $\approx 100\mu\text{m}$ thickness. Using a dimple grinder, samples were further thinned down to $\approx 25\mu\text{m}$ at the center. Finally, electron transparency was achieved at low energy Ar⁺ ion milling. Temperature dependent TEM measurements were done with 200 keV electrons. A single tilt heating holder (GATAN 628UHR, that has a tantalum furnace and can heat the specimen up to 1000°C) was used. The temperature is measured by a Pt/Pt-Rh thermocouple and is accurate within a couple of degrees. The holder has a water cooling system to avoid over heating of the sample surroundings and the specimen chamber, while keeping only the sample at a specified temperature. Real time measurements were

carried out using a CCD camera (GATAN 832) in which real time movies can also be recorded. For the ≈ 5 nm Au on Si(100) system, temperature dependent TEM measurements (*in-situ*, real time) were carried out using 200 keV system (TEM at IOPB) and *ex-situ*, room temperature (RT) and high resolution measurements were carried out using STEM and high resolution TEM (HRTEM) measurements using 300 keV electrons in the Cs-corrected FEI Titan 80/300 system.

3.3 Results and discussions

In-situ heating experiments were carried out at a ramp rate of 7°C min^{-1} . At each set of temperatures, the specimen was kept for about 30 minutes to achieve a stable temperature. We discuss here about the 2 nm Au on Si(100) system without the native oxide barrier at the interface and 5 nm Au on Si(100) with the native oxide layer [127].

Without native oxide(MBE grown)

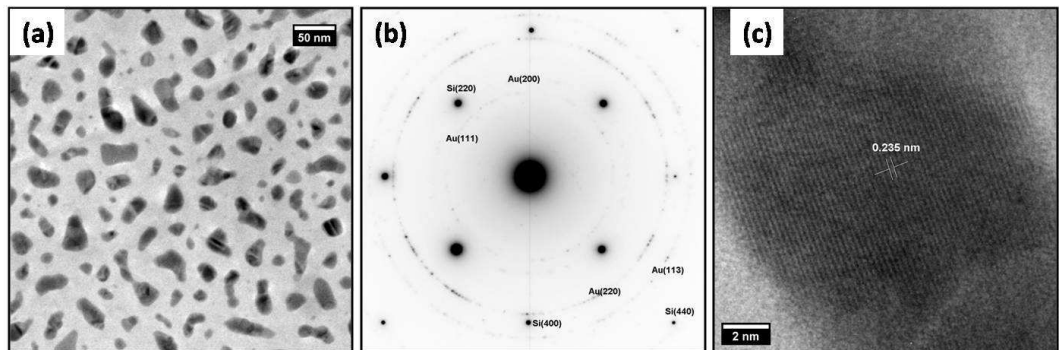


Figure 3.1: As deposited MBE sample showing (a) gold nanostructures with typical size of about ~ 24 nm (b) SAD pattern showing reflections of both Si and Au and corresponding (c) high resolution image of one of the islands which is showing the d-spacing of Au(111). [127].

As shown in figure 3.1(a), the gold islands have irregular shaped isolated structures in *as-deposited* system grown using MBE. The selected area diffraction (SAD) pattern shown in Figure 3.1(b) confirms the polycrystalline nature of gold films. A close look at the diffraction pattern suggests the existence of some texturing, as more reflections

from (220) plane can be observed. A high resolution TEM taken on nanostructures shows lattice spacing ($0.235 \text{ nm} \pm 0.005 \text{ nm}$) corresponding to elemental gold (Figure 3.1(c)) from one of the isolated island structures. Typical size of the island structures was found to be $\approx 24 \text{ nm}$ (Fig. 3.1(a)).

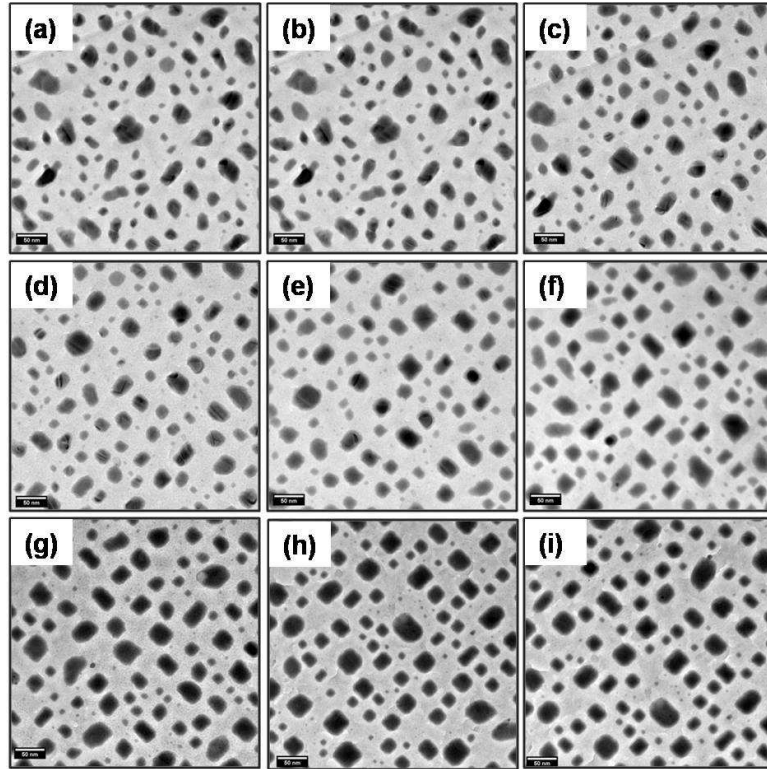


Figure 3.2: Bright field transmission electron micrographs depicting real time morphological changes during the *in-situ* heating. (a), (b), (c), (d), (e), (f), (g), (h) and (i) show the morphology at 200°C , 300°C , 325°C , 350°C , 363°C , 400°C , 510°C , 600°C and 700°C , respectively. With increasing temperature, growth of rectangular nanostructures can be seen [127].

Figure 3.2 depicts bright field (BF) images at various temperatures (200°C , 300°C , 325°C , 350°C , 363°C , 400°C , 510°C , 600°C and 700°C) [127] and figure 3.3 shows SAD patterns taken at various temperatures (325°C , 350°C , 363°C , 510°C , 600°C and 700°C). At 200°C , as shown in Figure 3.2(a), an almost similar morphology was found as in the *as-deposited* case. This shows that the system was quite stable without any inter-diffusion among the gold nanostructures below 300°C (Fig.3.2(a) and (b)). Fig.3.2(c) depicts a BF image taken after the system was kept stable at 325°C .

Interestingly, the shape of nanostructure appears to start having definite symmetries (like 4-fold) at these low temperatures. During the observation, we noted that some rectangular structures started forming at many places. The real time SAD pattern at 325°C (i.e., while the system was kept at this temperature) is shown in figure 3.3(a). The SAD pattern confirms the presence of silicon and un-reacted gold in the system. This shows that silicide formation is not a necessary condition to have well defined and symmetric structures. In-plane diffusion depending on the substrate orientation appears to play a major role in various shape formations of these gold nanostructures. It is well known that *bulk* Au-Si system has a eutectic phase at 363°C. The temperature was increased by smaller intervals ($< 25^\circ\text{C}$) around the *bulk* eutectic temperature. Figure 3.2(d) depicts a BF image taken at 350°C. At this temperature, a larger number of nano structures having rectangular shapes were formed. As the temperature was increased to 363°C and then to 400°C (Fig. 3.2(e), 3.2(f)), the coverage area of rectangular shaped nano structures increased. Also some of the structures were of square shape. The SAD pattern taken at 363°C (Fig. 3.3(c)) showed signature (compared with the case at 325°C) of un-reacted gold at this temperature. We did not take SAD pattern after cooling the specimen to room temperature (RT) at this stage and hence it is not possible to comment on eutectic phase formation. It is important to note the studies by Ijima *et al* on the dynamic behaviour of ultra-fine gold particles (~ 2 nm) at the atomic resolution using a HRTEM equipped with real time video facility [129]. They observed that particles continually changed their shapes, orientations and internal atomic arrangements within a time interval of one tenth of a second. The *in-situ* diffraction patterns were found to be diffused, giving an impression that the particles are in liquid phase. But, after cooling down to room temperatures, high resolution TEM showed a regular arrangement of atoms in individual particles [129]. In our studies, at lower temperatures ($< 363^\circ\text{C}$), gold nanostructures were relatively stable at these temperatures. Cooling to RT could help us in a proper determination of silicide formation at these low temperatures ($< 363^\circ\text{C}$).

Real-time *in-situ* heating measurements were continued at 400°C (BF image at Fig. 3.2(f)), 510°C (Fig. 3.2(g)), 600°C (Fig. 3.2(h)) and 700°C (Fig. 3.2(i)). More aligned nano-rectangles/squares were formed at these higher temperatures. The average ratio of length to breadth, defined as *aspect ratio*, has been determined by using many bright field images taken at each temperature: 325°C, 350°C, 363°C, 510°C, 600°C

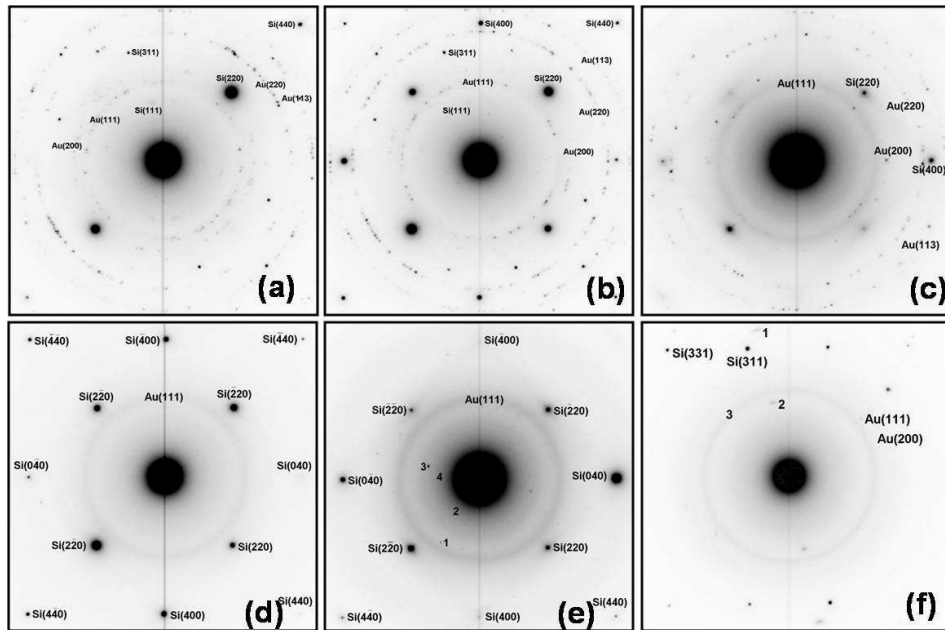


Figure 3.3: *In-situ* SAD patterns taken at various temperatures during heating of 2.0 nm Au/Si(100) system. (a), (b), (c), (d), (e) and (f) show the real-time diffraction pattern at 325°C, 350°C, 363°C, 510°C, 600°C and 700°C respectively [127].

and 700°C. In determining the aspect ratios, the longer side of the rectangles was taken as length. The average length, average aspect ratio, the percentage of nanostructures having square/rectangle shapes and the coverage of the gold at various temperatures are tabulated in Table 3.1. At 325°C, the aspect ratio was found to be 1.30 ± 0.02 and the average length was about 19 ± 1.0 nm. Interestingly, even at this stage (about 36% of the nano-structures were having rectangular shape). As the temperature was increased, the average length and percentage of nano rectangles increased but the average aspect ratio decreased. At 365°C, the average aspect ratio and length was found to be 1.18 ± 0.01 and 24 ± 1.0 nm. At 400°C, average length was increased slightly and the aspect ratio was almost same (as at 363°C). This indicated that there was a small change in one of the side. The percentage of nano rectangles was found to be 69% at this temperature. After 510°C onwards, the average length, average aspect ratio and percentage of particles having rectangle /square shape were almost constant. At 700°C, the average aspect ratio and length was found to be 1.13 ± 0.02 and 26 ± 1.0 nm, respectively and the percentage of particles having rectangle/square shape was 82% [127]. This is an interesting point of observation.

The aspect ratio larger than 1.0, is attributed to some kind of shape transformation. Such shape transformation occurs as a part of release of strain at the interfaces or within the island structures. During the silicide growth at high temperatures, higher aspect ratio silicide could be formed so as to reduce the strain energy, which is often explained by coincidence site lattice matching mechanism. In the present case, the variation in the aspect ratio is about 10–20% over the temperature range, and cannot be attributed to the coincidence site lattice matching mechanism. From fig.3.2, one can also observe that initially the gold nanostructures were having very rough edges and corners. With the increase in temperatures, smoothening of these edges and corners was observed. Ressel *et al* have reported about the behaviour of liquid Au-Si alloys on Si surfaces when ~ 2.0 nm of gold was deposited on Si(111) and Si(100) substrates at 400°C under UHV condition to form the droplets [130]. Detailed and elaborate real time SEM measurements by this group discussed many aspects of wetting phenomena of Au–Si liquid alloys but as the characterization was done using SEM, crystalline quality details of these structures were not discussed [130]. Shape of the droplets changed from circular to hexagonal above 750°C for the Au/Si(111). But, in the case of Au/Si(100) droplets were octagonal when solid and on melting became rounded at higher temperatures. The authors attributed this to the anisotropy in the line tension between solid/liquid/gas lines. With increasing temperature the entropic effects reduce the free energy difference between straight and curved steps leading to a rounding of the shape [130].

In the following, we discuss the SAD and high resolution transmission electron microscopy (HRTEM) results that are obtained for a system at different temperatures and at room temperature (after cooling from 700°C)[127]. Real time SAD patterns showed the diffraction spots of single crystalline silicon and rings of gold. Apart from this, a few extra spots and ring were also found which match neither with silicon nor gold. Interestingly, from 325°C to 350°C, no extra spots other than pure silicon spot and gold ring were seen for real time SAD (Fig. 3.3(a), 3.3(b)). After 363°C onwards, diffuse ring of d-spacing 0.235 nm were observed along with silicon spots (Fig. 3.3(c)). This d-spacing value (0.235 nm) matches with both gold and gold silicide phases. At 510°C, the SAD pattern shows the single crystalline spots of silicon and the diffuse ring of d-spacing 0.235 nm (Fig. 3.3(d)). More careful analysis reveals that the edges of the nano rectangles are aligned along $\langle 110 \rangle$ and $\langle 1\bar{1}0 \rangle$ direction with respect to the silicon substrate. At 600°C, few extra reflections other than silicon and gold spots

Temperature	Average length (in nm)	Average aspect-ratio	% of particle having rectangular/square shape	% of area covered by gold
325°C	19 ± 1.0	1.3 ± 0.02	36	23.5
350°C	20 ± 1.0	1.2 ± 0.01	45	23.4
363°C	24 ± 1.0	1.18 ± 0.01	58	23.6
400°C	27 ± 1.0	1.18 ± 0.02	69	23.6
510°C	25 ± 1.0	1.12 ± 0.01	80	23.9
600°C	25 ± 1.0	1.12 ± 0.01	81	24
700°C	26 ± 1.0	1.13 ± 0.02	82	24

Table 3.1: Average length of the nanostructures, the aspect ratio, the percentage of having rectangular/square shape and the coverage of the gold at various temperatures is mentioned in the tables. [127].

were observed (Fig. 3.3(e)) which were found to match with at least three reported phases of gold silicides. The spot nos.1, 2, 3 and 4 corresponds to a d-spacing of 0.253 nm, 0.453 nm, 0.356 nm and 0.469 nm respectively. When compared with the reported phases these lattice spacing match with several phases like Au_5Si_2 , Au_5Si , Au_7Si , Au_2Si and Au_3Si . Similarly at 700°C, spot nos. 1 and 2 and ring no 3 corresponded to a d-spacing of about 0.147 nm, 0.261 nm and 0.294 nm respectively (Fig. 3.3(f)). They matched with the phases of Au_5Si_2 , and Au_5Si .

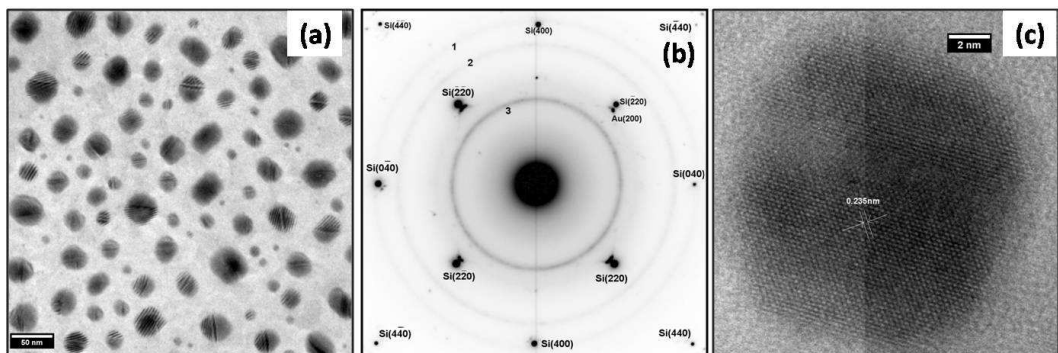


Figure 3.4: (a) Bright field image taken at room temperature after the sample was heated up to 700°C, (b) selected area diffraction showing the presence of mixed phase of silicide and (c) high resolution transmission electron micrograph of single nano rectangles.[127]

Figure 3.4(b) gives the SAD pattern obtained at room temperature (RT) after cooling down the sample from 700°C. Apart from Si and Au reflections we found a few extra rings which were found to match with at least four reported phases of gold silicide. Ring no. 1, 2 and 3 corresponds to a d-spacing of about 0.133 nm, 0.156 nm and 0.261 nm respectively [127]. On comparing them with the reported phases, these spacing match with several phases like Au₅Si, Au₃Si, Au₇Si and Au₅Si₂. Many diffraction patterns of gold silicides have been presented over the years [131, 132, 133, 134, 135, 136]. Hultman *et al.* rightly pointed out that when comparing the observed data with reported phases of gold silicides, surprisingly there is a good agreement between the d-values for at least 8–12 strongest reflections of all the alloys [137]. Looking at the constancy of lattice spacing of strongest lines, they doubt whether these diffraction patterns arise from different phases or they represent various degrees of ordering of super lattices of one fundamental structure. Because, the fundamental lines are similar for all reported phases except Au₅Si₂. As in our case, lack of symmetry further adds to the difficulty of assigning one definite phase to the obtained diffraction pattern. It should be noted that the minimum size of the SAD (SAD aperture) available with our system is bigger than a single silicide/island. Hence the SAD pattern shows these features (representing various reflections). Figure 3.4(a) and 3.4(c) shows the bright field image of the nano structures and the high resolution image of a single nano rectangle. From the bright field image one can observe that some moire-fringes are present on the nano rectangles and that the corners of the rectangles are rounded [127]. Due to the different bonding strengths along two facets the migration barrier experienced by the gold atoms along the length of the rectangle and around the corners differ, which causes the rounding of the corners [138]. In summary, for 2 nm Au on clean Si(100) surfaces, ordered and symmetric structures were formed at higher temperature. The diffraction data suggest the formation of nano silicide structures i.e. interfacial diffusion occurs along with the shape transformation at higher temperatures.

With native oxide(PVD grown)

We now present the experimental results on second case where a thin native oxide layer is present at the interface of Si(100) substrate and 5.0 nm Au film. Figure 3.5(a) and 3.5(b) show the bright field images of the thermally grown as deposited gold nano structures for this system and the corresponding selected area diffraction

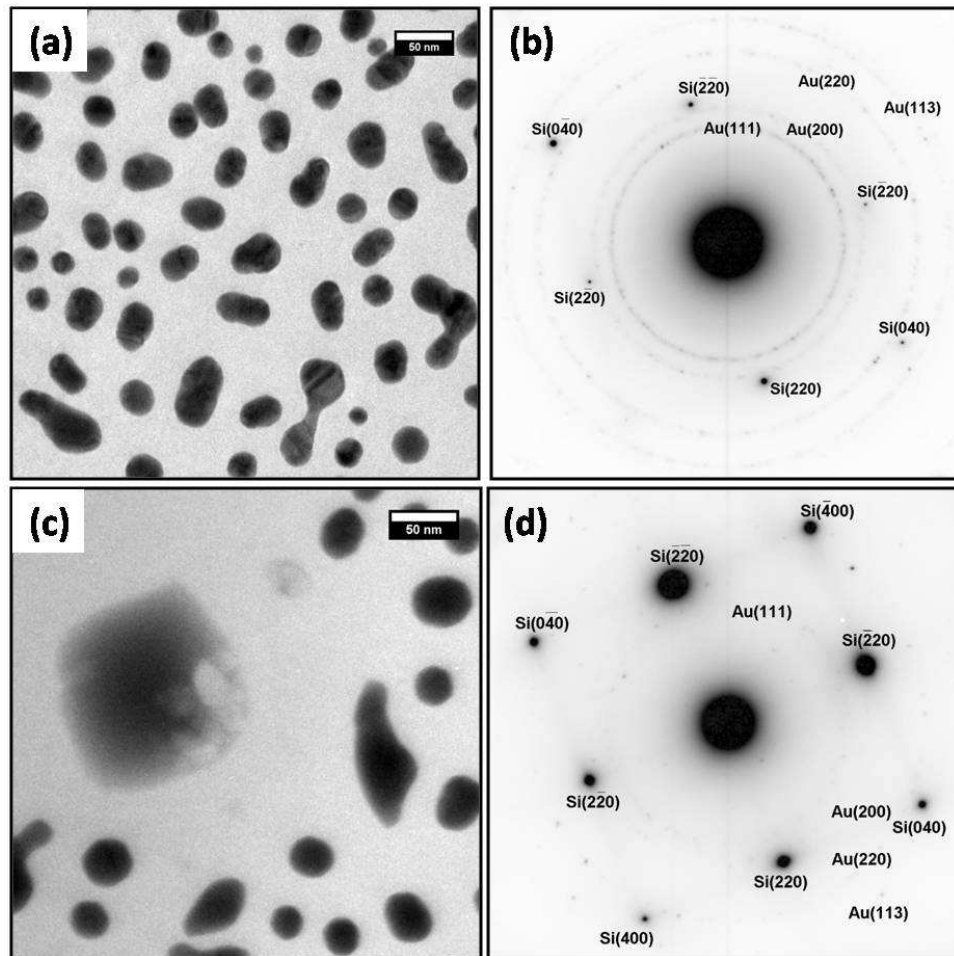


Figure 3.5: (a) Showing *as-deposited* thermally grown nanostructures 5 nm Au/SiO₂/Si(100) system, (b) corresponding SAD pattern showing the reflection of Au and Silicon, (c) BF transmission electron micrograph at 850°C and (d) corresponding selected area diffraction pattern [127].

pattern. Due to non-wetting nature of gold on native oxide covered silicon substrate, isolated nanostructures of gold are formed on the surface (as shown in Fig. 3.5(a)). The average size of these gold nanostructures 34 ± 1.0 nm has a coverage area of 24%. The coverage area remained the same throughout the temperature range (up to a temperature of 700°C) showing no loss of gold from the surface [127]. Comparing this with MBE grown structures (i.e., 2 nm Au case grown in UHV conditions), where the average size for the nanostructure is 27 ± 1.0 nm. The nano structures were also found to be isolated (i.e. not-connected network) in case of native oxide at the interface. While carrying out the real-time imaging during the annealing procedures on this system (5 nm Au/SiO₂/Si(100)), no appreciable change in morphology was observed until 750°C . The native oxide at the interface hinders the inter-diffusion and hence the reaction rate for interacting with bulk silicon is reduced [123]. During MBE growth on clean surfaces, at relatively lower temperatures, the Au–Si interface allows inter-diffusion and in-plane diffusion in the system. When the specimen (system with oxide layer) was annealed at 800°C , agglomeration was observed at some locations. At 850°C , square/rectangular structures having average size 110 ± 1.0 nm were found along with the un-reacted gold particles (Fig. 3.5(c)). Contrast between the rectangular structure and some un-reacted gold particles can be clearly seen. It indicates the formation of some Au–Si compositions. Selected area diffraction shows the single crystalline silicon background and some weak polycrystalline rings of Au (Fig. 3.5(d)). Desorption of gold from the rectangular gold silicide structure can also be seen at one corner in Figure 3.5(c).

Similar structure is shown with a high resolution STEM in Figure 3.6. STEM images were used to determine the nature of these rectangular structures. The STEM-high angle annular dark field (HAADF) image shown in Figure 3.6(a) depicts a rectangular gold silicide structure. This shows the expected Z-contrast, so that the Au appears brighter than the Si substrate. Interestingly, at one corner we observe a decrease in the contrast value where a rectangular hole-like structure in larger island is observed. This suggests loss of gold atoms at this location. To analyze the local distribution of Au in these structures, STEM- X-ray energy dispersive spectrometry (XEDS) elemental mapping has been carried out for the whole structure shown in Figure 3.6(a). Figure 3.6(b) shows the Au elemental distribution and the Figure 3.6(c) depicts the Si elemental distribution. These maps not only confirm that the island consists of

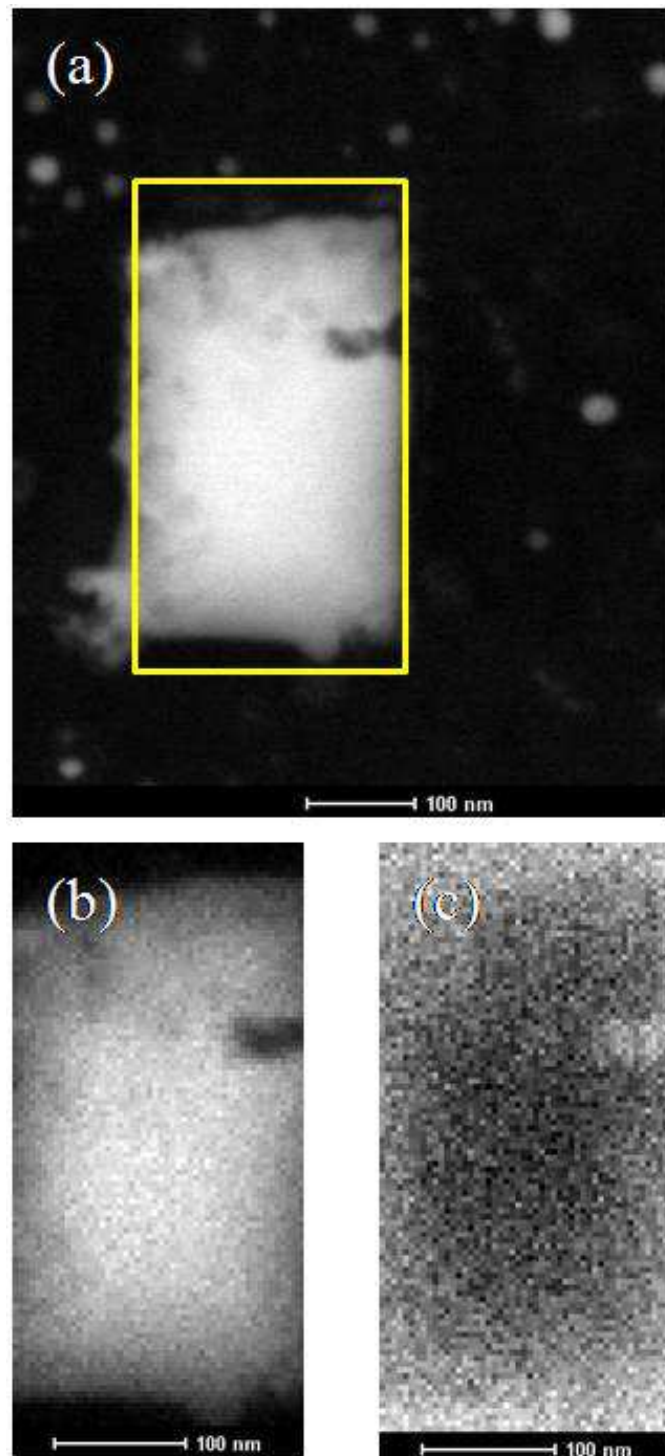


Figure 3.6: (a) STEM– HAADF image on one of gold silicide structure. This shows formation of a hole like structure: (b) the elemental mapping formed with Au x-ray signals, (c) with Si x-ray signals in the STEM-XEDS mode [127].

Au, but also that Au-depletion takes place at the island edges. The apparent Au-depletion in Figure 3.6, can be attributed to the melting induced desorption of gold from these silicide island structures. Figure 3.7(a) depicts a STEM – HAADF image of one gold silicide structure which developed hole like structures and 3.7(b) is a TEM bright field image of the same structure shown in figure 3.7(a). One of the main issues in this study is to understand where and how the gold silicide desorbs and forms a pit like structure. As reported by Wang *et al* [109], the pits can be used to grow different kind of structures. Figure 3.8 depicts a high resolution lattice image taken at 300kV using a Cs corrected microscope. It is to be noted that we could not succeed in taking lattice image from the same structure using 200 keV electrons (Figures 3.2 - 3.5 are carried out with 200 keV systems) as the structure appeared to be very thick. This demonstrates the importance of high energy electron microscope. The lattice spacing values suggest the presence of decomposed (or un-reacted) gold (with a lattice spacing of 0.235 nm) and a possible meta-stable phase of gold silicide(a value of 0.261 nm corresponding to $\text{Au}_5\text{Si}_2(123)$ plane). Although lattice image from the center of the hole like structure is not evident, fast Fourier transform of area at the center showed some crystalline nature. More detailed studies are necessary to understand the evaluation of the hole like structures.

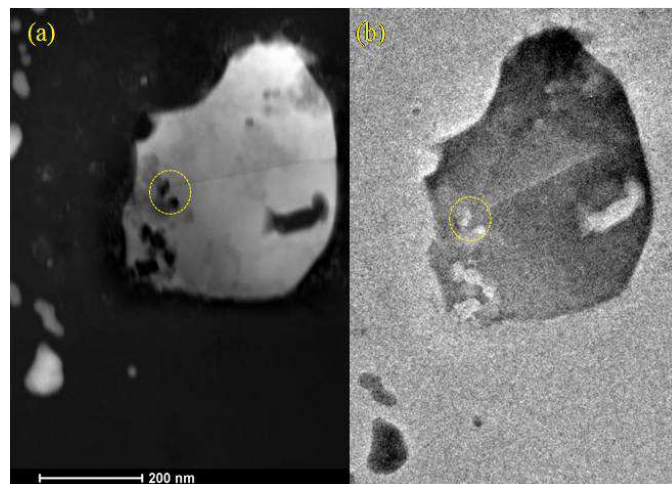


Figure 3.7: (a) STEM–HAADF image on one of larger gold silicide structure. This shows formation of many holes like structures inside (b) the TEM bright field image of same structure that was shown in (a)[127].

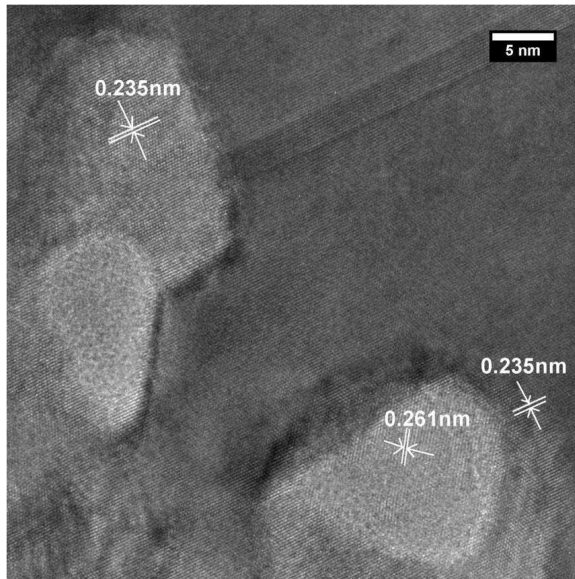


Figure 3.8: The lattice image taken from the area shown with circles in figure 3.7(b)[127].

3.4 Conclusions

We showed that it is possible to grow symmetric (4-fold) gold silicide nano structures when grown under ultra high vacuum condition and on clean Si(100) surfaces and annealed *ex-situ* in a heating stage in TEM even at relatively low temperatures. Real time high temperature studies showed evaluation of these structures and the area coverage value and the aspect ratio of these structures were found to increase at higher temperatures. For system with oxide at interface, no symmetric structures were found until $\approx 750^\circ\text{C}$. At these higher temperatures, due to desorption of native oxide present at the interface, rectangular structures were formed. We observed desorption of gold and /or gold silicide structures and formation of symmetric hole like structures in some cases. In this chapter, all the annealing experiments were done inside the high vacuum chamber. In the next chapter, how the presence of a native oxide layer at the interface influences the formation of faceted nano/micro structures inside low vacuum chamber will be presented.

Chapter 4

Growth of Oriented Au Nanostructures: Role of Oxide at the Interface

4.1 Introduction

In chapter 3, thermal behavior of gold nanostructures were studied *in-situ* by doing annealing experiment under high vacuum (HV) condition. In this chapter, the annealing experiment are performed under low vacuum (LV) condition to investigate the role of oxide at the interface of gold nanostructures and Si substrate in the formation of highly oriented faceted gold nano/micro structures.

It is well known that, crystalline silicon substrate's surface has an oxide layer (SiO_x), typically of a few nm thick. The layer thickness depends on the orientation of the substrate as well. There are several types of oxides depending on their mode of growth, *viz*: thermal oxide, CVD oxide, anodized oxide etc. of various thicknesses due to their importance in microelectronics industry. SiO_2 is widely used as gate insulators in the fabrication of metal oxide semiconductor devices, masking layer, isolation dielectric and as passivation layer [139]. In the case of MOS devices, current passes through the SiO_2/Si interface and passivation by the oxide layer is important for the operation of such devices. It also acts as an insulation between individual devices on the same Si substrate. Thin oxide film also acts as a capacitor, charge storage capacity being inversely proportional to thickness of the oxide layer. As a

passivation layer, they provide good dielectric properties, low surface recombination velocity, controlled immobile charge density and device stability at the elevated temperatures under bias or operating conditions [140]. Further, inter-diffusion behaviour of a metal (overlayer) - semiconductor (substrate) system is strongly influenced by the presence/absence of an oxide layer at the interface. The reaction between oxygen and silicon surfaces is one of the widely studied system, the reason being the important role the SiO_2/Si interface plays in the performance of Si based electronic devices. It would be interesting to study these interfaces to understand their chemical and physical nature [141, 142, 143]. It is known that utility of such systems in microelectronics, gas sensors etc., is greatly influenced by the interplay between strain energy and surface energy at surfaces and interfaces. The morphology (dimension, shape and number density) of 3D islands grown could be controlled by tuning the thickness and growth environment (for example temperature and vacuum).

In recent years, Au nano/microstructures were studied actively due to their variety of applications in the emerging area of nanotechnology [144, 145, 24]. For example, the gold nanostructures have been used for tuning the surface plasmon resonance from the visible to the near *IR* range of the spectrum by changing the dimensions or shape of nanostructures [146]. In spite of generally being considered chemically inert in its bulk form, ultra-fine gold nanoparticles are known to be active catalysts (more so when supported by an oxide surface) [147]. As a result, various methods of preparation of gold nano/micro structures (spheres, rods, trapezoids, wires, triangles, squares etc) have been well reported [121, 122, 123, 127, 120, 29]. Recently, Sanjeev *et al* have studied the structural evolution of Au films on Si(100) and Si(110) substrates in N_2 atmosphere and found that the resulting structures reorient themselves at higher temperatures [148]. Previous reports suggest the formation of faceted gold nanostructures, such as tetrahedrons, octahedrons, decahedrons and icosahedra structures. Surface energy anisotropy has been incorporated to understand the facet formation, crystal nucleation, growth and surface dynamics [149, 150, 151, 152, 153, 154, 155]. The correlation of surface energy anisotropy with the equilibrium crystal shape has been extensively studied over the last century, since the foundations were laid by Wulff [156]. Equilibrated metal particles were previously used to study the surface energy anisotropy of several face-centered cubic metals such as gold [157, 158, 159]. Ruffino *et al* have studied the effect of surrounding environment on the equilibrium

shape of nano gold structures using HRTEM and surface energy calculation by inverse *Wulff* construction method [160].

In this chapter, we discuss the influence of a native oxide and thermally grown oxide layer at the interface of Au/Si(100) systems, in the formation of highly oriented Au nanostructures at high temperatures. In this study, we have used a high vacuum (HV) based physical vapor deposition method and ultra high vacuum (UHV)-molecular beam epitaxy (MBE) facilities to grow various thicknesses of Au film on different surface conditions of the substrate such as with or without native/thermally grown oxide layer at the interface of gold and silicon substrate. The resulting systems were characterized by various electron microscopy methods such as, field emission gun based scanning electron microscopy (FEGSEM) at low and high energies, (scanning) transmission electron microscopy ((S)TEM) in combination with electron energy loss spectroscopy (EELS).

4.2 Experimental Section

Gold thin films of various thicknesses (5.0 nm, 11.7 nm and 50.0 nm) were deposited on Si(100) substrates while keeping the native oxide layer by thermal evaporation method under high vacuum conditions. To check the role of oxide layer thickness, an oxide layer of 50.0 nm thickness was thermally grown (using dry oxidation method) on Si(100) substrate and followed this by depositing a 50.0 nm Au thin film by HV thermal evaporation method (hence forth these systems are denoted as Au/SiO_x/Si). To have a cleaner interface (i.e. without oxide at the interface), an 11.7 nm thick Au film was deposited on Si(100) under ultra high vacuum (UHV) conditions with a base pressure of 2×10^{-10} mbar. For this purpose, we have used molecular beam epitaxy (MBE) system where in the surface was cleaned by flashing the substrate at a temperature of about 1200°C [127]. This procedure resulted in not having a native oxide present at the interface of Au and Si (hence forth these systems are denoted as Au/Si). The *as-deposited* Au/SiO_x/Si and Au/Si systems were annealed in the low vacuum furnace ($\approx 10^{-2}$ mbar) at $\approx 975^\circ\text{C}$ for 30 minutes. Cross-sectional TEM (XTEM) specimens were prepared using mechanical thinning followed by low energy Ar⁺ ion

milling. For scanning transmission electron microscopy (STEM) based EELS measurements, specimens were prepared using focused ion beam. The TEM characterization of the above samples was done with 200 keV electrons. SEM (scanning electron microscopy) measurements were carried out with 1.0 - 20 kV electrons (Neon40, Cross Beam, Carl Zeiss) and the scanning TEM (STEM) measurements were done using 300 keV electrons in the Cs-corrected FEI Titan 80/300 system. SEM based Electron backscatter diffraction (EBSD) measurements were done to study the orientation of the resulted structures. More details about the experimental procedure is given in chapter 2.

4.3 Results and discussion

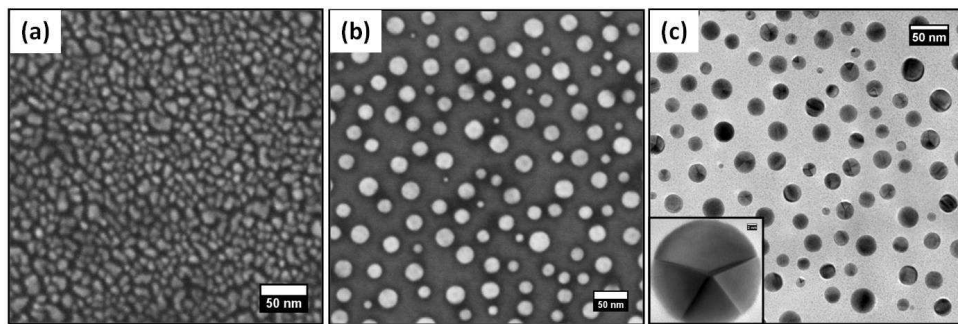


Figure 4.1: (a) SEM image of *as-deposited* samples of 5 nm Au/SiO₂/Si(100) (b) SEM image taken at *RT* after annealed upto 975°C (c) corresponding bright field TEM image (inset figure shows the HRTEM image of one of the multiply twinned decahedral gold structure).

A detail description on the formation of faceted structures at higher temperature has been presented in this section.

Figure 4.1(a) shows the bright field TEM image of *as deposited* 5.0 nm Au thin film on Si(100) substrate. The thin film seems to be continuous with almost 50% surface coverage. Fig. 4.1(b) and 4.1(c) depict the SEM and TEM micrograph of the above sample which was thermally annealed at $\approx 975^\circ\text{C}$ under low vacuum condition respectively. Formation of gold nanostructures could be seen with an average diameter of 17.3 ± 1.2 nm. The *inset* figure shows the HRTEM image of one of the multiply twinned decahedral gold structure. To study the interface of the above

mentioned sample, cross-sectional TEM (XTEM) analysis has been done. In figure 4.2(a), the XTEM image of the *as-deposited* sample clearly shows the presence of ~ 2.0 nm thin native oxide layer at the interface between gold nano structures and the silicon substrate. The High resolution XTEM image in Figure 4.2(b) shows the d-spacing of Au(111). Fig. 4.2(c) shows the bright field XTEM image of the gold nano structures annealed at $\approx 975^\circ\text{C}$ and corresponding HRTEM image (Fig.4.2(d)). The average height of 21.8 ± 1.1 nm. It is to be noted that the planar TEM images suggest the formation of spherical nano particles, where as the XTEM image reveals the beginning of the facet formation [161]. To understand the role of thickness of the gold film, similar studies were carried out for 11.7 nm Au/SiO_x/Si(100) and 50 nm Au/SiO_x/Si(100) as well.

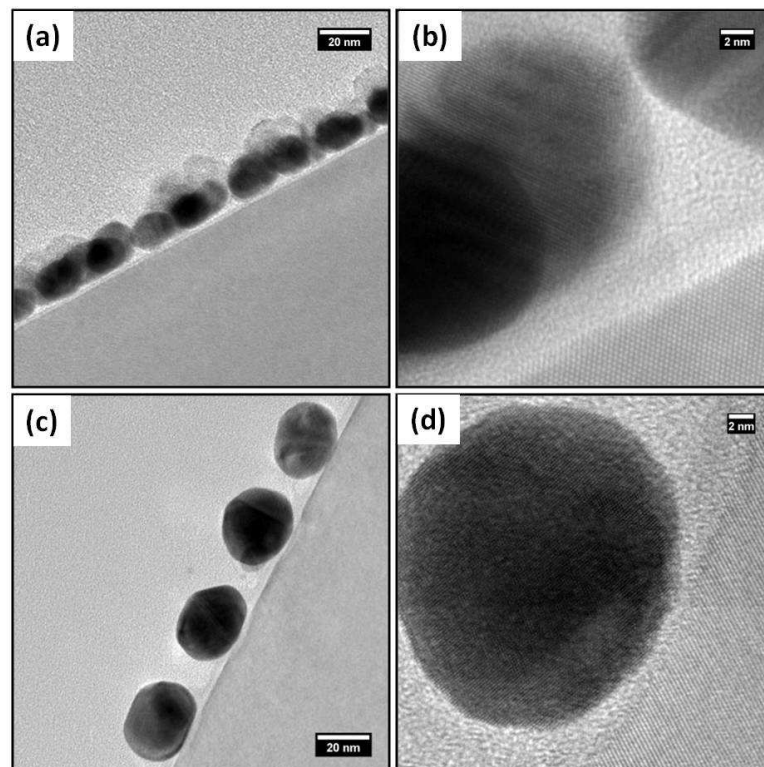


Figure 4.2: (a) BF XTEM image of *as-deposited* samples 5 nm Au/SiO₂/Si(100) and (b) corresponding HRTEM image. (c) shows the XTEM image of the 5 nm Au/SiO₂/Si(100) taken at *RT* after annealed upto 975°C and (d) corresponding HRTEM image.

4.3.1 Formation of oriented Au Structures

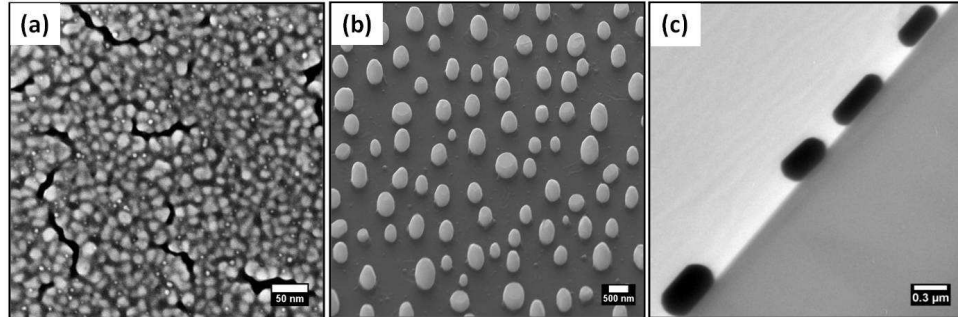


Figure 4.3: (a) SEM image of *as-deposited* samples 11.7 nm Au/SiO₂/Si(100) (b) SEM image taken at *RT* after annealed upto 975°C and (c) corresponding XTEM image.

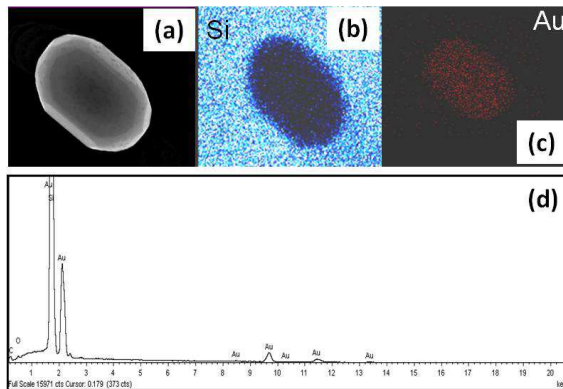


Figure 4.4: SEM image of 50nm Au/SiO₂/Si(100) heated upto 975°C (a) elemental mapping which shows the presence of substrate silicon (b) and Au (c) and corresponding EDX spectrum (d).

As deposited 11.7 nm Au/SiO_x/Si(100) system shows almost a continuous layer with a surface coverage of $\sim 99\%$ (Fig. 4.3 (a)). Annealing under low vacuum conditions for about 30 minutes leads to the formation of multi-faceted three-dimensional (3D) gold structures with an average size of 248 ± 13.1 nm (Fig 4.3(b)) and an average height of 210 ± 9.6 nm (Fig 4.3(c)). The *as-deposited* 50 nm/SiO_x/Si(100) system shows almost a continuous layer (Fig.4.5(a)) and formation of well oriented faceted 3D gold structures with average size 530 ± 18.6 nm (4.5(b)) and average height 291 ± 11.6 nm (fig 4.5(c)) were observed upon annealing under the above mentioned condition. The inset image of Fig. 4.5(b) shows the high resolution SEM image (taken at 5 keV electron energy), where facets can be clearly seen. It is to be noted that, in both of the above systems height of gold particles is lower than their width. Figure 4.5(c) shows a cross-sectional TEM image of one of the faceted structures and

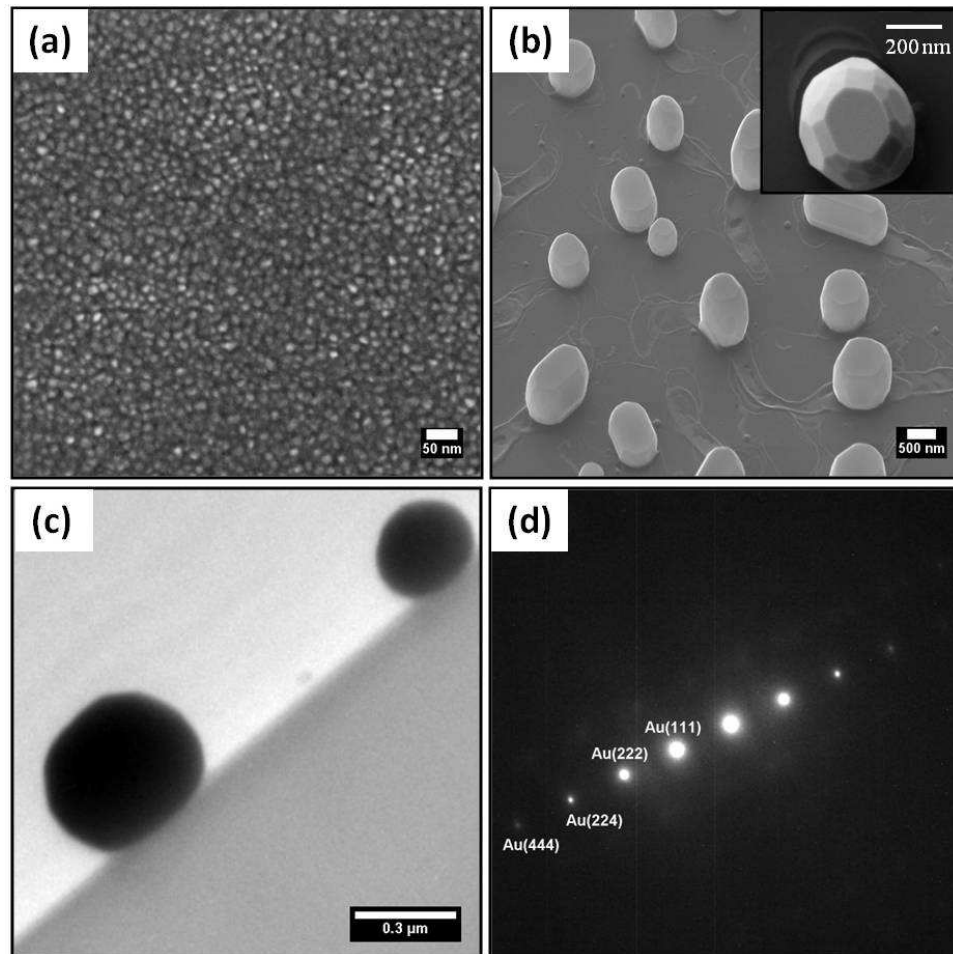


Figure 4.5: (a) SEM image of *as deposited* samples 50 nm Au/SiO₂/Si(100), (b) SEM image taken at *RT* after the sample was annealed upto 975°C (inset figure shows SEM image taken at 5 KeV electron energy), (c) corresponding XTEM image and (d) SAD pattern taken on one of the Au island.

the figure 4.5(d) depicts selected area diffraction (SAD) taken on a single structure. The spots correspond to a d-spacing of 0.235 nm, 0.118 nm, 0.058 nm and 0.083 nm which matched with the (111), (222), (444) and (224) planes of Au [162]. It indicates that gold islands were crystalline in nature. SEM based elemental mapping (Fig. 4.4(a)–4.4(c)) and the corresponding EDX spectrum (fig. 4.4(d)) show the presence of Au in the faceted structure and Si from the substrate [161].

4.3.2 Role of Vacuum level and interfacial oxide

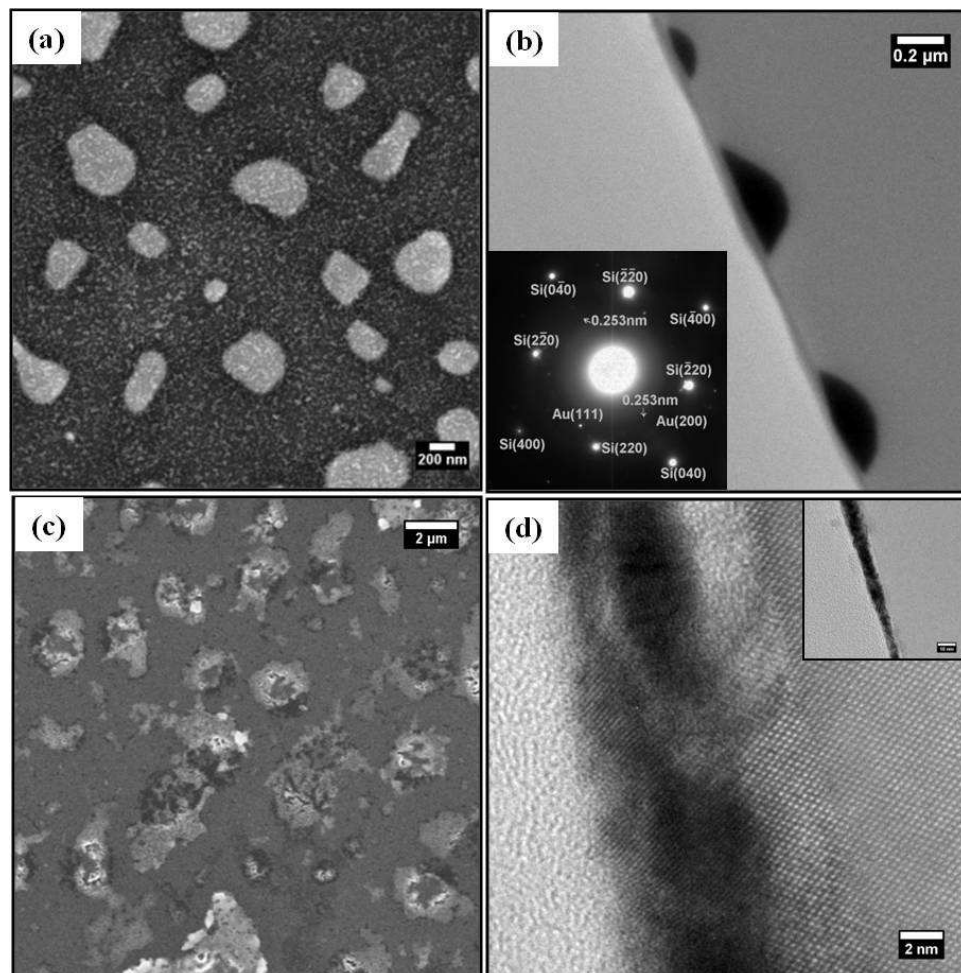


Figure 4.6: SEM image shows the (a) 11.7 nm Au grown by MBE (without native oxide at the interface) method which is annealed upto 975°C inside LV and (b) corresponding XTEM image (inset figure shows the SAD pattern) (c) thermally grown (with oxide) 11.7 nm Au annealed upto 975°C inside HV and (d) corresponding XTEM image .

To study the effect of the absence of any oxide layer at the Au/Si interface was demonstrated by carrying out similar studies on the third system, 11.7 nm Au/Si(100). Native oxide layer was removed at high temperature under UHV conditions (as explained in the experimental section) and a 11.7 nm Au thin film was deposited in the MBE system. This system was subjected to similar low vacuum annealing treatment and no formation of multifaceted 3D gold structures was observed (SEM image shown in Fig. 4.6 (a)). Instead, some fractal type of textures were formed along with irregular gold islands (Fig. 4.6 (a)) indicating that the interfacial oxide plays an important role in the formation of faceted particles. It should be noted that, for MBE grown 2nm Au under high vacuum annealing condition, (figure 3.1 and figure 3.2) well aligned rectangular gold silicide structures were formed at 500°C. The detail about the role of vacuum level on the morphology of gold structures during annealing would be discussed in chapter 5. Figure 4.6(b) depicts a XTEM image of the above sample which shows the interfacial diffusion of gold into the substrate silicon. In the *inset* figure, SAD pattern shows extra spots along with the spots of Au and substrate silicon. The d-spacing 0.253 ± 0.005 nm neither matches with gold nor silicon. This confirms formation of some kind of gold silicide. It matches with several of the reported gold silicide phases like Au_2Si , Au_3Si , Au_5Si_2 and $\text{Au}_{0.81}\text{Si}_{0.19}$ [136]. To check the role of vacuum, both 11.7 nm Au/SiO₂/Si(100) and 50 nm Au/SiO₂/Si(100) systems were annealed inside the HV chamber. Formation of faceted 3D gold structures were not observed in both the cases (Figure 4.6(c), Figure 4.7(a) and (b)). Figure 4.6(d) shows the XTEM image of the interface for the HV annealed 11.7 nm system. The d-spacing at the interface (0.226 nm) matches with the several of the reported gold silicide phases *viz.* Au_2Si , Au_3Si , Au_5Si , Au_5Si_2 , Au_7Si and $\text{Au}_{0.81}\text{Si}_{0.19}$ [136]. Similarly, for 50 nm HV annealed case, the HRTEM shows the d-spacing of 0.262 nm which matches with Au_5Si_2 and Au_3Si phases of gold silicide (fig. 4.7(c)). It is seen that the faceted 3D gold structures are not formed whenever there is interfacial diffusion. The detail about the role of vacuum level in formation of gold silicide will be discussed in chapter 5. In MBE grown case, there is no oxide layer at the interface. Hence, at higher temperature, both interfacial diffusion and the surface energy minimization processes occur. Due to the competition between the above two processes, equilibrium shape is not achieved by the system. Whereas in oxide case, no alloy formation has been seen (figure 4.5(d)). The oxide at the interface inhibits the process of silicide at the interface and helps in growing faceted Au structures [161].

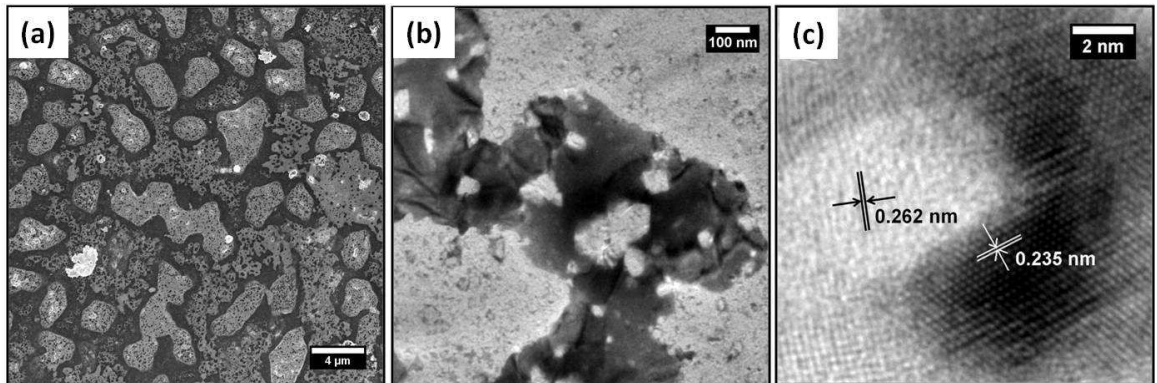


Figure 4.7: (a) SEM image of thermally grown 50 nm Au heated upto 975°C inside HV (b) corresponding Bright field TEM image and (c) the HRTEM image shows the presence of gold silicide.

To investigate the effect of thickness of the interfacial oxide, 50 nm SiO_x layer was thermally grown on Si substrate and following this a 50 nm thick Au film ($\sim 50\text{nm}$) was deposited under high vacuum conditions. This system, i.e., 50nm Au/50nm $\text{SiO}_x/\text{Si}(100)$ was subjected to low vacuum annealing for 30 minutes as explained earlier. Formation of 3D faceted islands has been observed, interestingly similar to earlier system (Fig 4.9). The inset figure shows the high resolution SEM image (taken at 5keV electron energy), where facets can be clearly seen. This result revealed that the thickness of the oxide layer does not seem to affect the facet but presence of oxide is necessary for the formation of facets [161].

In the following, we present results on the variation of the native oxide layer thickness at the Au and Si interface. Figure 4.8(a) depicts a STEM image taken from 50 nm Au/2 nm $\text{SiO}_x/\text{Si}(100)$ annealed at $\approx 975^\circ\text{C}$ under low vacuum conditions. Fig. 4.8(b) shows one of the corners of the faceted structure at a higher magnification. EELS scans (integrated counts in EELS oxygen data) have been taken from region (i) and region (ii). The full-width at half maximum (FWHM) of the oxygen peak varies from 3.5 nm to 6.6 nm (Figs. 4.8 c (i) and 4.8 d (ii)). This confirms the effective barrier role of an oxide layer inhibiting the Si out diffusion and Au inter-diffusion. The interface between (Fig. 4.8(a)) the Si substrate and the Au microstructures appears to be sharp without any Au diffusion into Si. But, for Au films grown under MBE

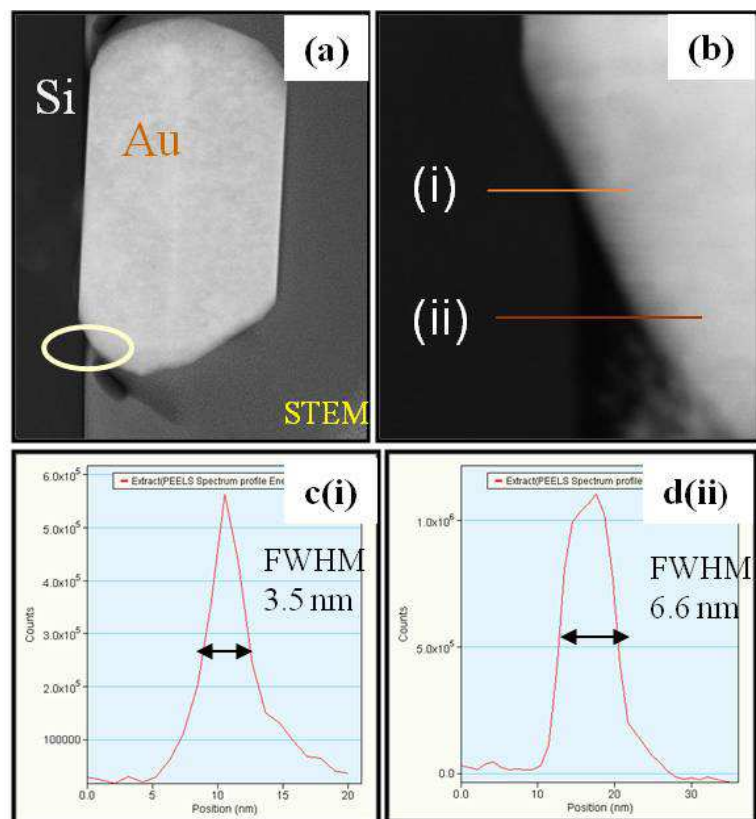


Figure 4.8: (a) STEM image from 50 nm Au/SiO_x/Si(100) annealed at 975°C. (b) is the region taken at higher magnification from a selected area in (a). Fig. c(i) is from the Oxygen EELS line scan from region (i) and d(ii) is from the region (ii) shown in (b). Width of the variation of oxide layer thickness can be seen in (c) and (d)[161].

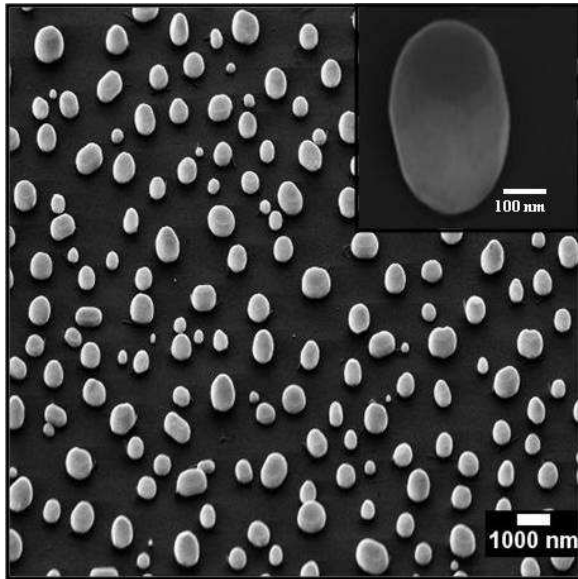


Figure 4.9: SEM image of 50 nm Au/thermally grown 50 nm $\text{SiO}_x/\text{Si}(100)$ substrate annealed at 975°C under low vacuum ((inset figure shows SEM image taken at 5 KeV electron energy.)

conditions, gold inter-diffusion was found to be very prominent (Fig. 4.6(b)) and this reduces the effect of later-diffusion of Au on the oxide surface and hence no oriented structures of Au are seen for the films that are grown under MBE conditions [161].

4.3.3 Study of orientation of the Faceted Gold structures

To study the orientation of the resulted structures, SEM based EBSD measurements were performed. SEM based EBSD orientation mapping (figure 4.10 (a)) shows that the top surface of almost all the particles exhibit (111) facet which well matches with our XSEM data. The inverse pole figures are shown in (figure 4.10(b) and 4.10 (c)). Each point on inverse pole figure is colored according to an automatically color coded unit triangle of the inverse pole figure. In figure 4.10(a), red color is assigned to [001] direction, blue to [111] and green to [101] direction. The surface with their (111) axis normal to the surface of the sample is blue in color. The purple color is assigned to the direction [112] i.e. between the [001](red) and [111](blue) direction. The preferred orientation of Au on silicon is along (111) direction. It can be noticed that some orientation are along (100) direction i.e. the orientation of the facet adjacent to the substrate. Figure 4.11(a) depicts the SEM image taken at 54° which shows that top surface of the facets are almost parallel to the silicon substrate. The XSEM images in Figure 4.11(b) were taken by focused ion beam (FIB) serial sectioning. The angle

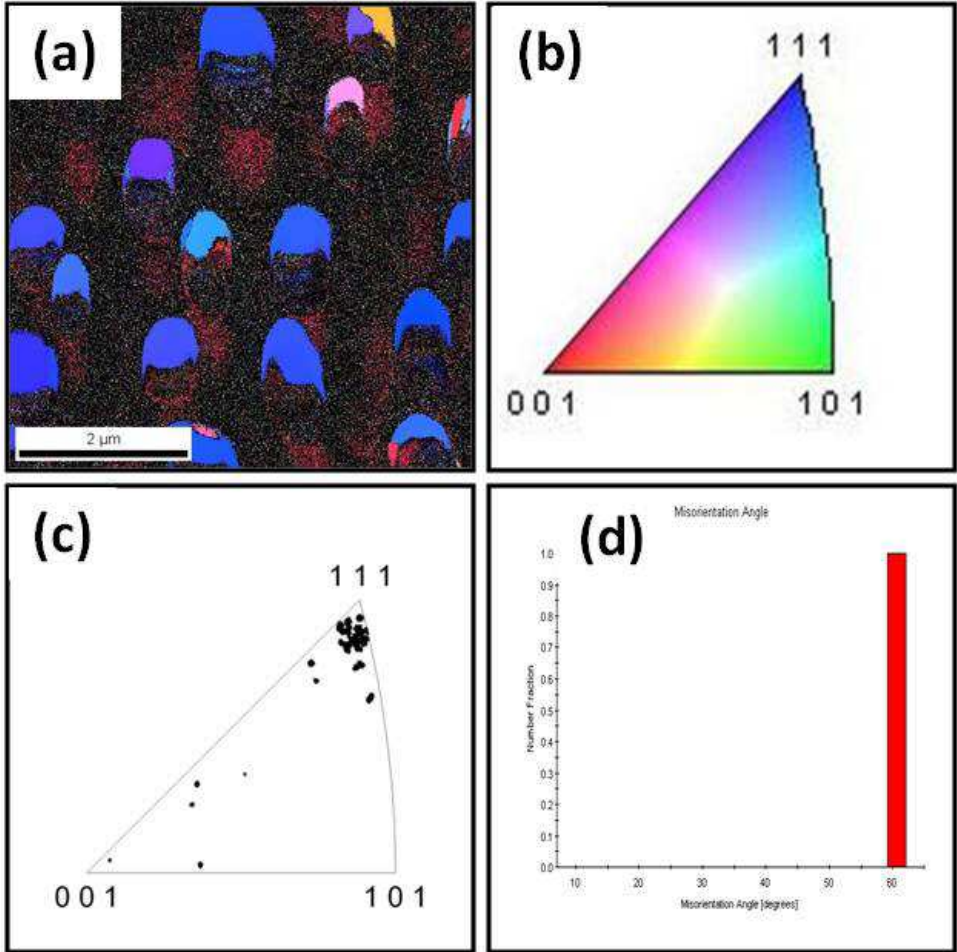


Figure 4.10: (a) SEM based EBSD orientation mapping in 50 nm Au/SiO_x/Si(100) annealed at 975°C, (b) and (c) corresponding inverse pole figures (d) histogram plot of the misorientation angle *V*s number fraction [161].

of contact between a typical faceted island and the substrate was found to be $126.3^\circ \pm 5^\circ$ ($180^\circ - 54.7^\circ$).

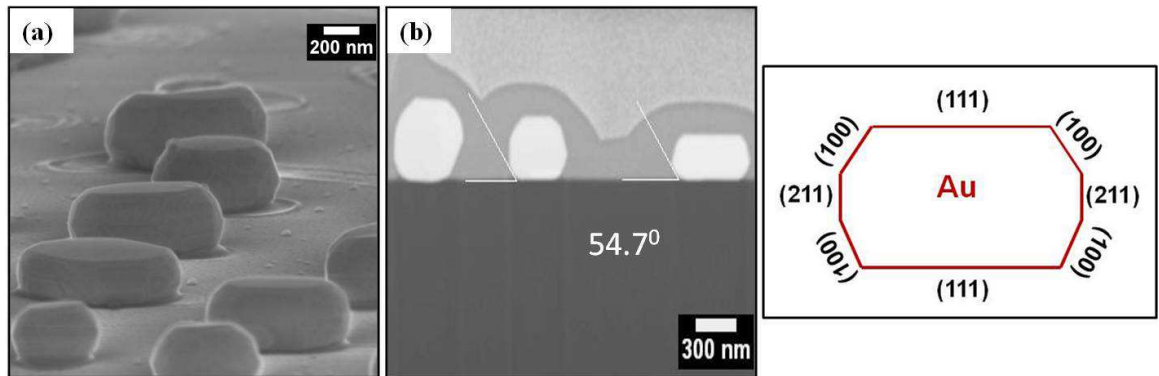


Figure 4.11: (a) SEM image taken at 54° tilt from 50 nm Au/SiO_x/Si(100) annealed at 975°C , (b) corresponding XSEM image showing the contact angle between the faceted structure and the silicon. The schematic diagram shows the planes of the facets.

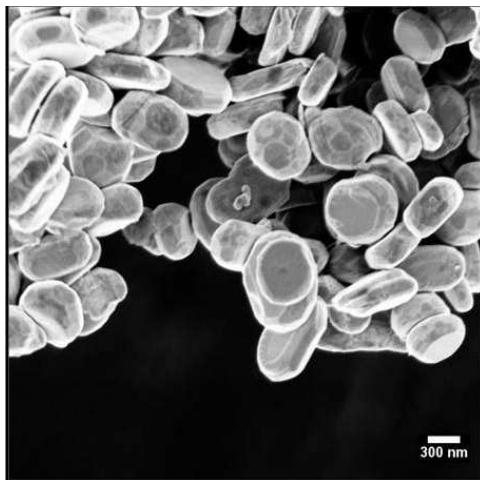


Figure 4.12: SEM image of the faceted gold particles on the carbon coated copper grid which are transferred from the silicon substrate by simple scratching method.

We have also calculated the angles between the faceted planes by averaging measurements taken on 30–40 particles. Almost all the faceted particles are bounded by (111), (100) and (211) planes which match with the studies done by L.D. Mark [151, 152]. It can be clearly seen in the schematic diagram. Our earlier SAD image (figure 4.5(d)) supports the above result. This can be explained by the fact that the surface energy of FCC metal has minimum for (111) orientation [163]. Furthermore the EBSD measurements provided the histogram distribution plot of number

of fraction *vs* misorientation angle which shows that all the particles prefer the (111) orientation (figure 4.10(d)). Due to high contact angle, the faceted particles are easily scrubbed from the substrate. It has been studied that for a large thickness, the elastic energy is proportional to the volume and dominates the surface contribution, so that the adsorbate tends to separate from the substrate and form a single big cluster almost detached from the substrate. This state obviously minimizes the elastic energy, and therefore the total free energy [164, 165]. In our system also the sub micron structures are less adhere to the silicon substrate and are easily detachable. Figure 4.12 shows the SEM image of the faceted gold particles on the carbon coated copper grid which are transferred from the silicon substrate by simple scratching method. Because of the decoupling from the substrate, it is very essential to fabricate this nano/micro structured material of well-defined shapes in controlled way for the actual applications of these structures.

4.4 Conclusions

In summary, we reported a simple procedure to fabricate well oriented gold nanostructures by annealing Au/SiO_x/Si(100) systems under low vacuum and at high temperature. The shape of the oriented structures could be tuned by varying initial thickness of gold film: formation of faceted gold structures were observed in the case of higher gold thicknesses as opposed low thickness where formation of only spherical nanoparticles were seen. It was also shown that the oriented microstructures cannot be fabricated without oxide layer at the interface (using MBE method). Electron microscopy methods were used to determine the morphological and crystalline nature of these structures. Similar experiments done in a high vacuum condition did not show any formation of faceted structures. This emphasizes the fact that low vacuum plays crucial role in the formation of 3D faceted gold structures. The detail study of effect of vacuum level on the formation of gold silicide structures will be discussed in the next chapter.

Chapter 5

Structural modification of gold silicide structures in Au/Si(100)system: Role of vacuum level and surface oxide

5.1 Introduction

In the previous chapters (3 and 4), growth of gold/gold silicide structures were investigated by annealing different thicknesses of gold films on Si(100) substrates under both high vacuum (HV) and low vacuum conditions. In this chapter, role of vacuum level on the formation of gold silicide structures and their shape, when a ~ 2.0 nm/Si(100) system with oxide and without oxide at the interface are annealed at high temperatures under different vacuum conditions would be presented.

The major issue in nanotechnology is the development of conceptually simple synthesis technique for the mass fabrication of nano scale structures. At this level, the conventional top-down approach becomes expensive and complicated process. One of the alternative methods is to make use of the self assembly growth procedure. Understanding of self assemble growth of nanostructures require a detailed knowledge that is based on the principle of microscopic pathways of diffusion, nucleation and aggregation. On surfaces, the hierarchy in the migration barriers as well as the non uniform strained fields induced by mismatched lattice parameters can be translated

into geometric order and well defined shapes and length scales of the resulting aggregates. One of the challenges in the self assembly growth process is to understand the nucleation process with atomic scale spatial resolution in real time sequence. Dynamic *in-situ* TEM studies involving a capability of variable temperature and with tens of millisecond time resolution play a key role in understanding the growth kinetics. In this work, we present the formation of nano gold silicides at an early stage in case of a ~ 2.0 nm thick gold film deposited on Si (100) with native oxide at the interface. Our results show that the oxide at the interface inhibits the gold reaction with silicon substrate and this resulting in formation of spherical gold nanostructures for annealing in low vacuum conditions [172].

The control of the morphology (dimensions, shape, and number density) of nano islands is essential for exploiting their properties in many fields like optical applications or biosensors based on the use of surface plasmon resonances or nano catalysis in which the catalytic action depends on both shape of the nano islands and the nature of the substrate [24]. It is important to note that the average size distribution and interparticle separations of the Au NPs are very important for controlling the diameters and spacing in catalytic growth of nanowires [166]. Thus, for tailoring the physical and chemical properties and their uses, the shape, size and composition must be controlled [24]. However, controlling the shape of nano particles grown by thin film technologies is generally difficult due to its dependence on kinetic and thermodynamic parameters which are stochastic in nature [167]. This approach usually requires thermal activation through heating the support. In this work, we deal with the formation of nano-gold silicide structure at high temperature and various vacuum conditions. Gold nano crystals with various shapes (rods, needles, triangle, trapezium, spheres and squares *etc.*) have been reported using various methods [123, 121, 161, 127, 28]. Also, much progress has been made in recent years in the understanding of island shapes in epitaxial growth systems. The spontaneous formation of nano-objects during epitaxial growth offers the advantage of defect-free structures obtainable very quickly. Depending on fundamental growth parameters such as surface temperature and deposition rate, the deposited atoms form aggregates that may have a variety of shapes. In this chapter, for thermally grown samples (with oxide at the interface) case, we report the role of vacuum conditions on the evaluation of various morphological changes that occur for the nano gold particles on Si (100) annealed at high

temperatures. Our results also show the enhancement in the thermal decomposition of underlying native/thermal oxide layer on Si(100) due to the presence of gold nanostructures grown on top of the native oxide. Some important aspects of such decomposition on Si (111) and Si(100) systems have been reported [168]. At elevated temperature and high vacuum conditions, silicon oxide thin films known to decompose by the overall reaction $\text{Si (s)} + \text{SiO}_2 \text{ (s)} \rightarrow 2 \text{SiO (g)}$ [44, 45]. In this process, voids are formed in the oxide layer exposing the substrate silicon. It has been reported that presence of a metallic thin film enhances such decomposition [169, 170, 171]. When such decomposition takes place during low vacuum conditions, one has to deal with simultaneous growth of oxide layers as well. This would contribute to play important role in controlling the inter-diffusion and reaction of gold with silicon. These effects are also reported in this work for a ~ 2.0 nm gold deposited on native oxide silicon substrate [172].

Also, for the MBE grown case(without oxide at the interface), role of vacuum level has been studied for 2nm Au/Si(100) system . More precisely, effect of vacuum on surface diffusion and effect of surface oxides on the corner rounding have been studied. The aim of this work is to set an optimum growth and annealing condition to control the surface diffusion and hence the morphology of the gold structures for the real applications. The finer variation at the edges of the gold nanostructures,like rounding of corners has been reported in this work [173].

5.2 Experimental methods

Gold films of ~ 2.0 nm thickness were deposited by thermal evaporation method under high vacuum ($\approx 4 \times 10^{-6}$ mbar) conditions on n-type Si (100) substrates (*system-A*). For these systems, thin native oxide with thickness of ~ 2.0 nm has been observed using cross-sectional TEM measurements. Planar TEM specimens were prepared from these samples. *In-situ* heating experiments were carried out by using a GATAN hot-stage TEM holder. Real time measurements were acquired using a CCD camera in which real time movies can also be recorded with 25 frames s^{-1} (40 ms resolution). The sample was annealed inside the TEM chamber (HV) up to 850°C (*system-A1*). Another *as-deposited* sample was annealed in a low vacuum furnace ($\approx 10^{-2}$ mbar)

at $\approx 850^\circ\text{C}$ for 30 minutes (*system-A2*). For *system-B*, A thin Au film of thicknesses 2.0 nm was deposited on n-type Si (100), by the molecular beam epitaxy (MBE) method under UHV (base pressure $\approx 2 \times 10^{-10}$ mbar) conditions[128]. The Si (100) substrates were loaded into the MBE chamber and degassed at $\approx 600^\circ\text{C}$ for about 12 hours inside the chamber, followed by flashing for about 3 minutes by direct heating at a temperature of $\approx 1200^\circ\text{C}$. In this process, native oxide was removed and a clean reconstructed Si (100)-(2 \times 1) surface (figure 5.5 (a)) was obtained. On such ultra clean surfaces, gold films of different thicknesses were grown epitaxially by evaporating Au from a Knudsen cell. Deposition rate was kept constant at ≈ 0.14 nm min^{-1} . During the growth, the chamber vacuum was 6.2×10^{-10} mbar. The thickness monitor was calibrated with RBS measurements. After the deposition, the samples were taken out of MBE chamber and annealed at 500°C in three different vacuum conditions: (*system-B1*) low vacuum (LV) external furnace (10^{-2} mbar), (*system-B2*) high vacuum (HV), (*system-B3*) UHV (10^{-10} mbar) chamber (MBE chamber). All above three cases, samples were exposed to air (for half an hour) before annealing. To study the effect of oxides we did the *in-situ* heating inside the UHV chamber without exposing to air (*system-B4*). Planar TEM sample was prepared out of that annealed specimen for further TEM measurements with 200 keV electrons.

5.3 Results and discussions

5.3.1 With oxide at the interface

Figure 5.1(a) depicts a bright field (BF) planar TEM micrograph for ~ 2.0 nm thick Au film grown on Si (100) substrate with a 2.0 nm thin native oxide at the interface between the Au nanostructures and the substrate. Irregular shaped gold nanostructures were seen with $\approx 18\%$ area coverage of gold nanostructures. The selected area diffraction pattern (SAD) taken on a group of nanostructures confirms the polycrystalline nature of the gold films and along with the reflections of substrate silicon (fig. 5.1(b)). The above system was annealed from (room temperature) RT to 850°C inside TEM column using the single tilt heating stage (*system-A1*). We have observed that at 600°C , the surface morphology was almost similar to that of as deposited system (as shown in Fig 5.1(a)). We noted the start of agglomeration of later diffusion of gold particles (kind of Oswald ripening) at 700°C happening at random sites and

this process increased (*i.e.* the number of clusters) with increasing temperature. At higher temperatures, *i.e.*, around 850°C, interestingly, desorption of the presumably gold silicide structures leading to the formation of hole like structures inside big clusters of gold silicide structures has been noted [172]. This can be attributed to the melting induced desorption of gold from these silicide island structures [127]. Interesting observation of nanosized gold particle movement and leading to the formation of nanosized ordered (square or rectangular) gold silicide structures has been seen. The contrast confirms the formation of silicide structures and later on, this is confirmed by the *in-situ* SAD pattern. This was explained based on the selective decomposition of native oxide at high vacuum and temperatures and there upon the gold diffuses towards the exposed silicon surface to form rectangular gold silicide structures [127]. In between these rectangular structures, un-reacted gold particles were still present (dark contrast) (Fig. 5.1 (c)). It should be noted that, in our earlier result (figure 3.5, chapter 3), similar rectangular nano structures were formed with larger size, when 5nm Au/SiO_x/ Si(100) system was annealed under same temperature and vacuum condition. The variation of contrast compared to that of un-reacted gold, indicates the formation of gold silicide. Fig. 5.1 (d) depicts selected area diffraction (SAD) pattern where the ring (arrow marked) corresponds to the d-spacing of 0.253 nm. It matches with both the Au₅Si₂ and Au₃Si phase of gold silicide [174]. It is well known that, at high temperature and good enough vacuum /oxygen free conditions, oxide layer undergoes thermal decomposition. Presence of gold acts as a catalyst for the decomposition to take place. According to Dallaporta *et al* [170], heat of reaction between gold and SiO₂ being positive [175], lack of reactivity requires that Au has to reach the Si/SiO₂ interface so that it forms gold silicide and enhances oxide decomposition process.

Fig. 5.2 shows the real time BF TEM image depicting the growth of nano rectangular/square shaped structures at the expense of gold nano particles. The Images are taken after the temperature was stabilized at 850°C. We presume the time at which the image shown in fig. 5.2 (a) as starting time (t=0.0s). At t=8.0s (fig. 5.2 (b)) there was no change in the morphology of the two nano particles (inside white circle). At t= 8.64s, they joined together (fig. 5.2 (c)). As time progressed, it tried to rearrange itself to get minimum energy configuration [151, 29] which resulted in formation of rectangular/square shaped silicide structures (fig. 5.2 (d) and 5.2 (e)).

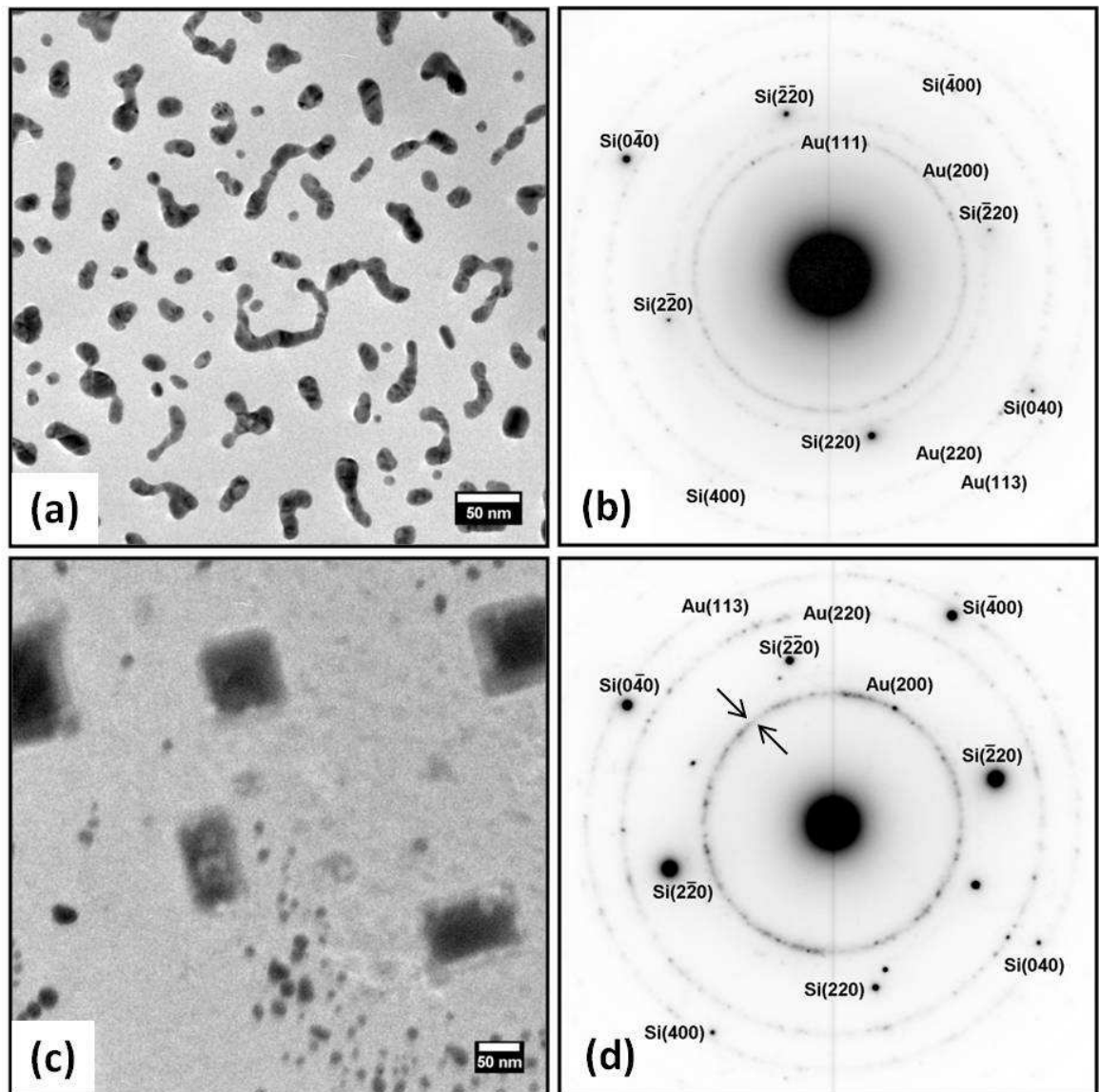


Figure 5.1: (a) BFTEM image of thermally grown *as-deposited* sample 2 nm Au/SiO_x/Si(100) showing nanostructures (b) Corresponding SAD pattern showing the reflection of Au and silicon (c) Bright Field transmission electron micrograph at 850°C (*system-A1*) (d) Corresponding selected area diffraction pattern and the ring (arrow marked) indicates the alloy formation [172].

Interestingly, we do not observe any further agglomeration after $t = 12.12$ s (fig. 5.2 (f)), (even after waiting for more than 20 min)[172]. The reason to such phenomena is not known yet as per our knowledge.

In fig.5.3, BF TEM image depicting the real time morphological changes of gold particle surrounded by group of particles during in situ heating (stabilized at the temp of 850C). Here also, we presume the time at which the image shown in fig. 3(a) as starting time ($t = 0.0$ s). At $t = 0.0$ s, particles denoted by legends A, B, C, D, E, F, G and H were present around the region of interest (*ROI*) structure (inside dotted white line: Fig. 3) at a distance of 18.4 nm, 67.6 nm, 56.3 nm, 28.7 nm, 55.4 nm, 107.4 nm, 132.9 nm and 32.2 nm respectively (fig. 5.3 (a)). After 6.32s, particle 'A' diffused into the *ROI* structure which resulted in increase of the size of the *ROI* structure (fig. 5.3 (b)). All the above 8 particles diffused into the *ROI* structure in 19.08s (fig. 5.3 (c)–5.3(h)). The contrast of the growing *ROI* structure and the gold particle confirms that gold from the particles diffuses into the Au–Si alloy (*ROI*) through a process more like Oswald ripening, similar to the results discussed by Kim et al [199]. Particles from all direction of the *ROI* structure are diffusing due to the square symmetry of the Si (100). Umananda *et al* showed the uni-directional growth of gold silicide rods which is attributed to the selective decomposition of oxide growth on the Si (110) surface [123]. After each intake of the particle, there was a increase in size of the *ROI* structure. After that, particles are not further diffusing and one can see the formation of hole like structures in the *ROI* structure due to the desorption of gold (fig. 5.3 (i)). Interestingly, no growth of gold silicide structure has been observed after the start of formation of hole. In each image frame, the already nucleated island with holes is present near the *ROI* structure without interacting with the nearest particles. At $t = 49.92$ s, more holes were formed in the *ROI* structure. Even after waiting for more than 30 min, there was no such change in morphology of the structure (fig. 5.3 (i)). It shows that the particles become stable after some critical size [172]. All the images shown in figure 5.2 and figure 5.3 are reproduced from the original video.

We now discuss the role of vacuum condition on decomposition and void formation processes. In a bid to study this aspect, the as-deposited sample was *ex-situ* annealed at 850°C for half an hour inside the low vacuum furnace (*system-A2*). Vacuum was kept at about 10^{-2} mbar (low vacuum obtained using a rotary pump). The system

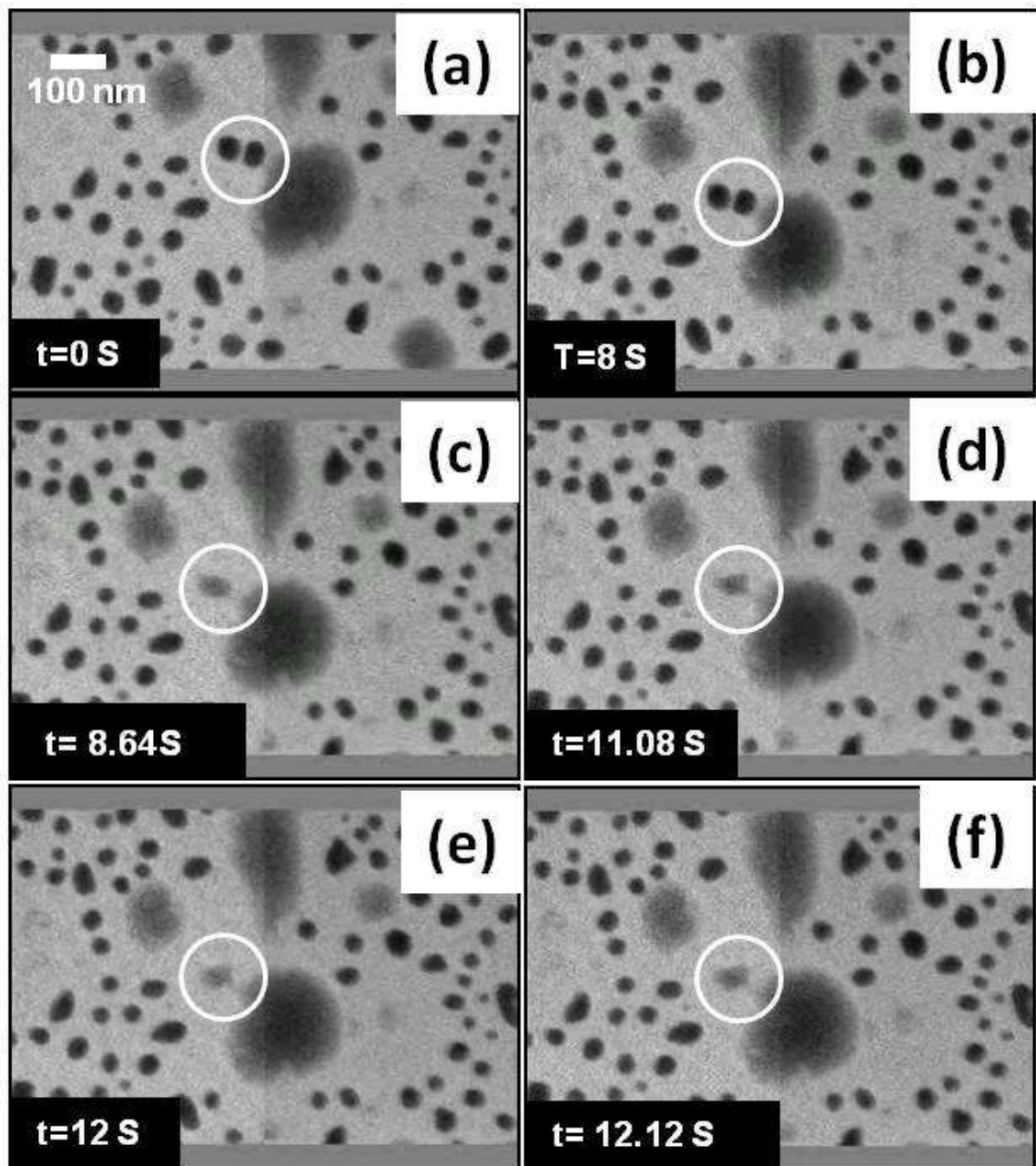


Figure 5.2: Real time bright field TEM image depicting the growth of a nano rectangle at the expense of gold nano particles (at 850°C)[172].

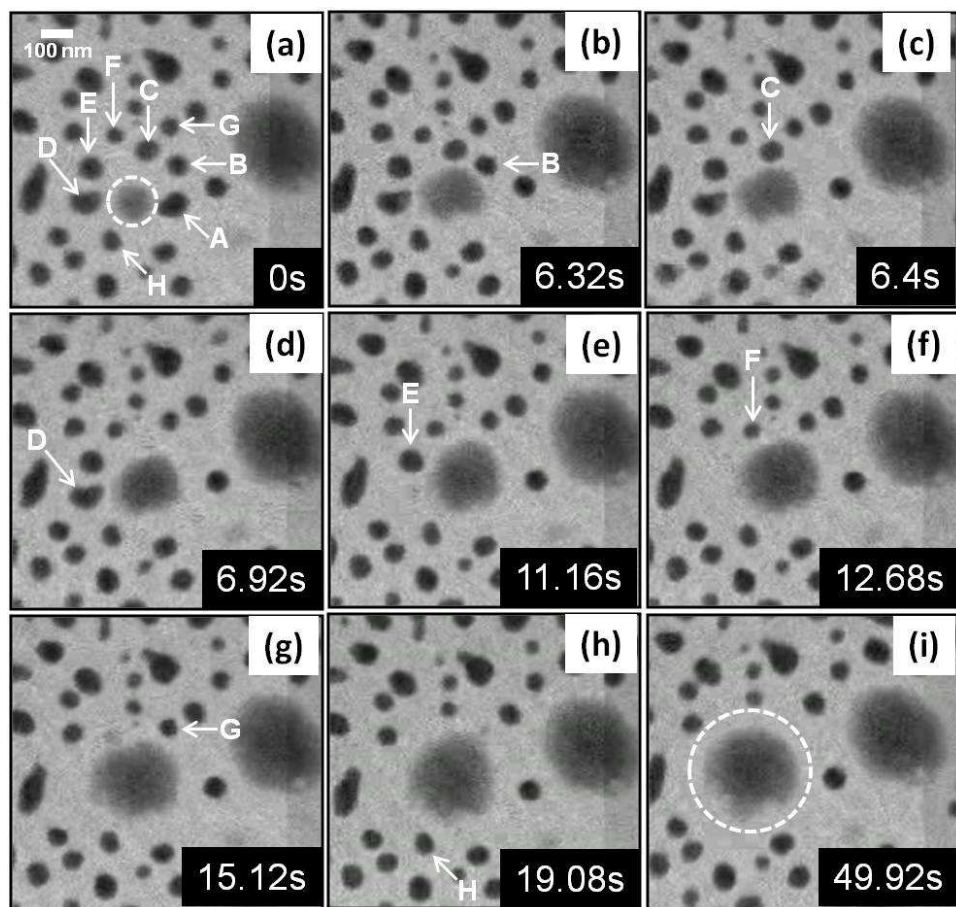


Figure 5.3: Bright field TEM image depicting the real time morphological changes during *in situ* heating (stabilized at the temp of 850°C)[172].

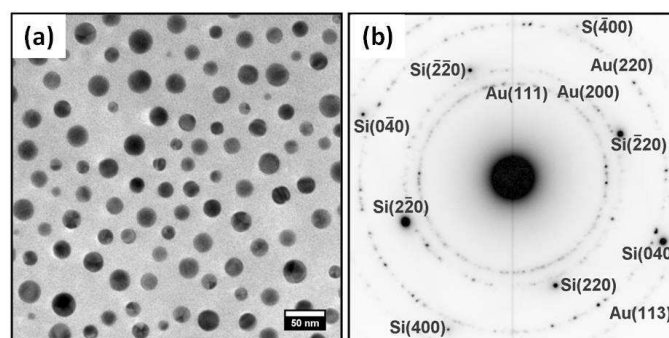


Figure 5.4: (a) 2 nm Au/SiO₂/Si(100) was *ex-situ* annealed (at 850°C) under low vacuum (*system-A2*) and then seen in TEM at RT (b) corresponding SAD showing the reflection of gold and silicon [172].

was allowed to cool down to room temperature (RT) for further TEM measurements. Fig. 5.4 (a) shows the bright field transmission electron micrographs taken at RT after vacuum annealing of 2nmAu/SiO₂/Si(100) system at 850°C. Interestingly, spherical particles of gold are observed with a monotonous size distribution. In the previous chapter (figure 4.1), for 5 nm Au/SiO₂/Si(100) system, we got the bigger sized spherical gold nano particles at 975°C under low vacuum annealing condition. It is very interesting that even after annealing at such a high temperature, formation of aligned structures were not observed as in Fig. 5.1 (c). As explained earlier, at such high temperature, under high vacuum conditions (i.e., in the absence of O₂), thin oxide layers undergo a reaction $\text{Si (s)} + \text{SiO}_2 \text{ (s)} \rightarrow 2 \text{SiO (g)}$, where SiO is a volatile product at high temperatures. This results in selective removal of oxide layer, leading to the growth of aligned structures. But, when the vacuum level is lowered to about 10⁻² mbar (and the vapor pressure of SiO being close to 10⁻¹ mbar at 1200°C [176]), rate of evaporation of volatile SiO will be affected. Also, at lower vacuum, mean free path of atoms/molecules present in the chamber reduces to fraction of a centimeter (which is of the order of kilo meters under UHV conditions) and the time required for the formation of a monolayer decreases to fraction of a milli second (from an hour for UHV). Thus, formation of a monolayer of external impurities (redeposition of SiO₂ here) takes much lesser time [76]. Thus, if the rate of redeposition of oxide exceeds the rate of decomposition, proper selective decomposition of oxide layer might not be possible. As a result, it hinders the growth of any gold reaching the silicon surface in forming aligned silicide structures. The SAD did not show any reflection of gold silicide phase except the signals of polycrystalline gold and the substrate silicon (fig. 5.4 (b)).

5.3.2 Without oxide at the interface

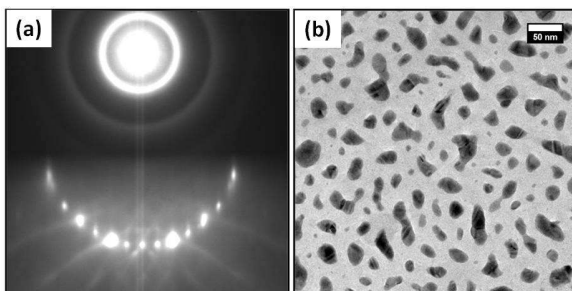


Figure 5.5: (a) Reflection high energy electron diffraction (RHEED) pattern showing clean reconstructed Si100-(2× 1) surface (b) Bright field TEM image shows the as deposited 2nm Au/Si(100) system.

We have already shown that the as deposited MBE grown 2 nm Au/Si(100) system (fig. 5.5 (b)) upon annealing inside the HV chamber (inside TEM) leads to formation of well aligned nano rectangular gold silicides structures [127]. This shape transformation is attributed to the strain relief mechanism and detailed explanation is given in the reference [127]. The effect of vacuum level on the growth of above structures when there is no oxide at the interface has been discussed in this section. To study that, The MBE grown as-deposited samples were annealed at 500°C in different vacuum conditions: HV, LV and UHV as mentioned in experimental details section. For HV (*system- B2*), well aligned nano rectangular structures were formed (fig. 5.6 (a)). The *in-situ* temperature dependent study of the formation of the above rectangular gold silicide structures was already discussed in chapter 3 (figure 3.2). The length (longer side is always considered as length) distribution of the structures was shown in Fig.5.6(b) and average length of the structures was 29.4 ± 1.5 nm. For LV (*system- B1*), same well aligned nano rectangular structures were formed (fig. 5.6(c)) but corners of the rectangles were not sharp. Due to the different bonding strengths along two facets the migration barrier experienced by the gold atoms along the length of the rectangle and around the corners differ, which causes the rounding of the corners [138]. The corner rounding effect is more prominent compare to the *system-B2*. Average length of the structures was 21.9 ± 1.2 nm (figure 5.6 (d)). There was no much change in mean length between *system-B1* and *system-B2*. Whereas for UHV case (*system-B3*), there was increase in mean length (fig. 5.7 (a)) and the structures were not full rectangular like previous case. The average length of the structure was 38.2 ± 1.4 nm (fig. 5.7 (b)). But it is interesting to notice that the corners are very sharp (fig. 5.7 (a)). It should be noted that in all above cases, samples were exposed to air (for half an hour) before doing the annealing experiment [173].

To study the effect of oxide we did the *in-situ* heating at 500°C inside UHV chamber without exposing to air (*system-B4*). Well aligned rectangles with sharp corners (no corner rounding) were formed (fig. 5.7 (c)). In fig. 5.7 (d) the length distribution shows broad distribution having average length 56.4 ± 1.6 nm. Upon air exposure, the native oxide was grown on the inter island regions, which hinder the surface reconstruction; but the Au-Si islands were still intact to the reconstructed 2×1 surface. During UHV annealing (*system-B3*), the islands follow the substrate symmetry due to the absence of native oxide layer at the Au-Si interface. Whereas oxide desorption

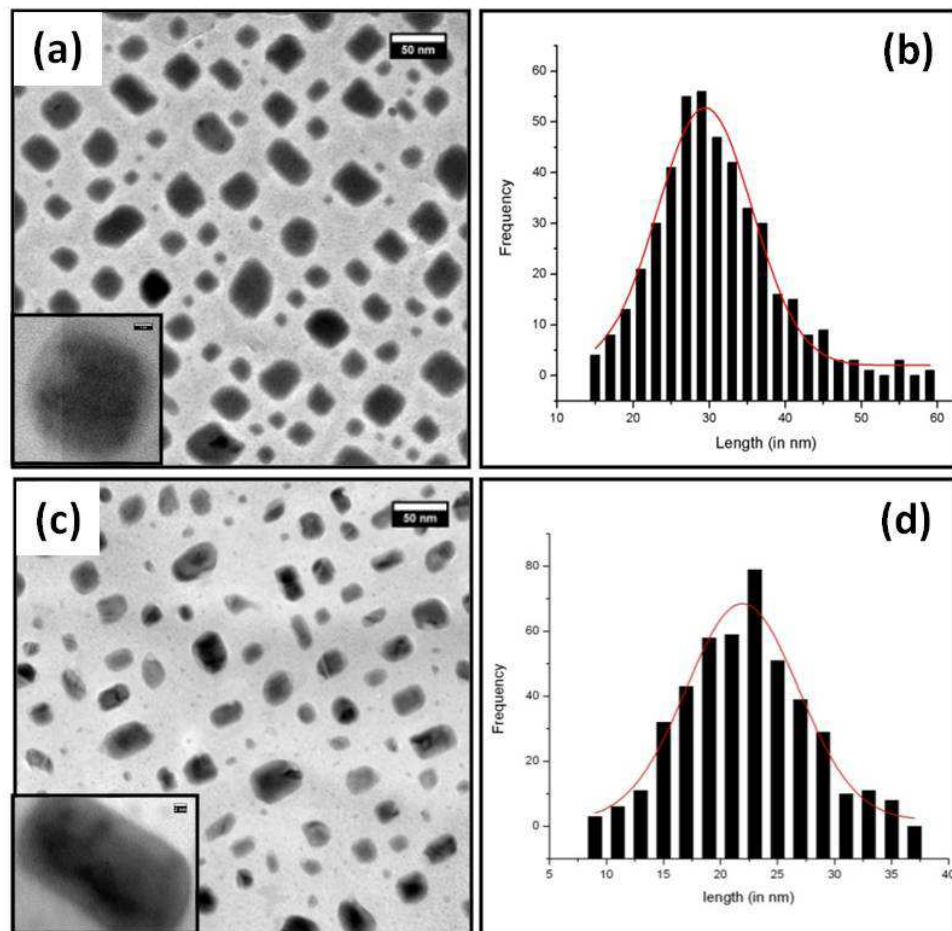


Figure 5.6: Bright field TEM image of MBE grown 2 nm Au/Si(100) system annealed upto 500°C inside (a) HV chamber and (c) LV chamber having average length 29.4 ± 1.5 nm (b) and 21.9 ± 1.2 nm (c) respectively. Inset figure shows the HRTEM image of one of the structures.

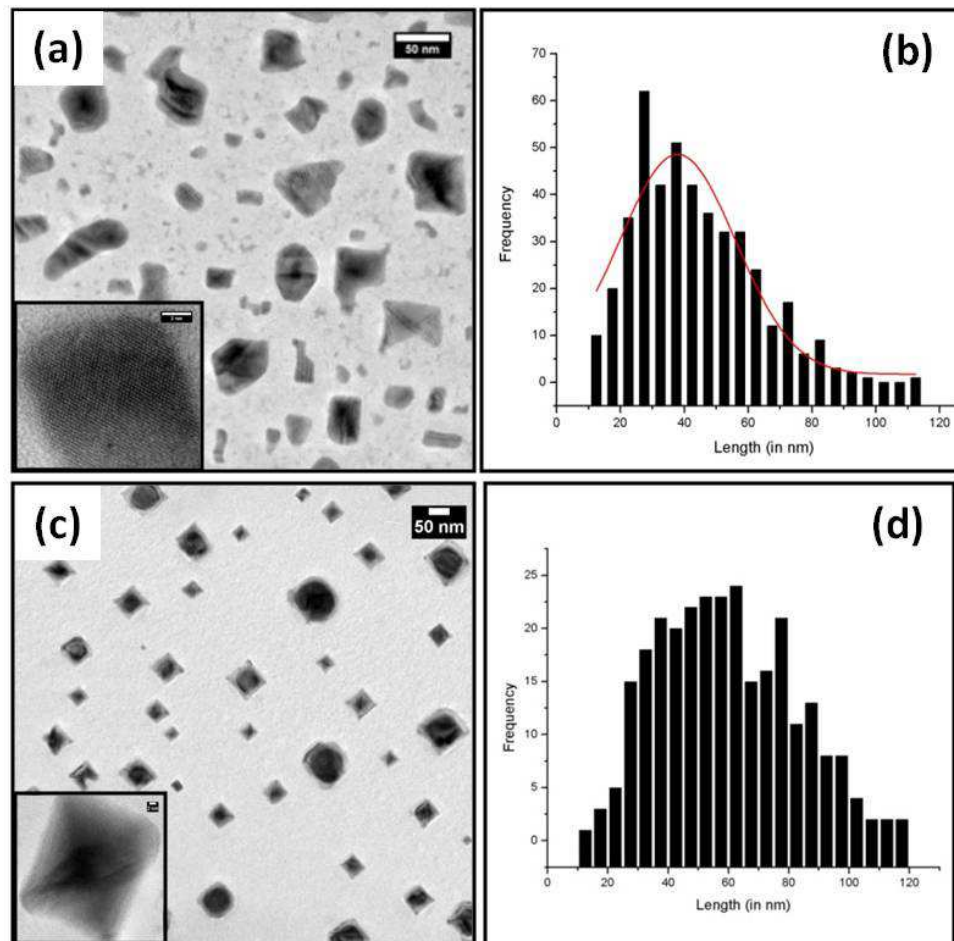


Figure 5.7: Bright field TEM image of MBE grown 2 nm Au/Si(100) system annealed upto 500°C inside UHV chamber (a) (with air-exposed) and (c) without air exposed (*in-situ*) having average length 38.2 ± 1.4 nm (b), 56.4 ± 1.6 nm (d) respectively. *Inset* figure shows the HRTEM image of one of the structures.

starts in the inter island regions, creating unsaturated bonds, which have a great affinity to attract the nearest gold particles. Therefore, the Au-Si islands diffuse towards the oxide desorbed region to minimize the surface energy, which results in the formation of irregular structures. But in contrast to the above case, in the *in-situ* UHV annealing (without surface oxide layer, (*system-B4*), the Au-Si islands form a regular rectangular shape following the 2×1 reconstruction [173].

As mentioned earlier, in LV (*system-B1*) and HV (*system-B2*) annealing case, well aligned rectangular structures were formed on the same air exposed samples unlike in the UHV annealing case (*system-B3*). It has been reported that at LV, HV and UHV, the redeposition of oxide takes about 2.0 ms, 2.0 s and 1 hour respectively to form a monolayer [175, 176, 76]. Thus, if this rate of redeposition of oxide exceeds the rate of decomposition, proper desorption might not be possible. As the oxide desorption is more in UHV compare to HV and LV, the diffusion of Au-Si islands towards the desorbed area is less probable in later cases. So the islands get less deformed in HV and LV annealing, forming a regular stable shape. All the results presented in chapter 3, chapter 4 and chapter 5 are summarized in tabular form in the appendix A. In the next chapter, we present the work wherein these gold silicide nanorectangular structures would be used as template for the growth of Ge.

5.4 Conclusions

In-situ real time measurements were performed on 2nm Au/ SiO_x/Si(100) system under HV annealing condition inside TEM. Aligned nanostructures were observed at elevated temperature. Whereas for similar system, upon annealing externally in low vacuum condition leads to the formation of spherical nano gold particle (no formation of aligned gold nano-structures) establishing the fact that vacuum level plays an important role in the selective decomposition process. Similarly, MBE grown 2.0 nm Au on a cleaned Si (100) under thermally annealing in different vacuum levels (LV, HV and UHV) resulted in aligned nanostructures in all three cases. The variation at the edges of the gold nanostructures like rounding of corners has been demonstrated in this chapter. This can be attributed to the variation in diffusion of gold silicide islands due to the presence of surface oxides. These near-regularly spaced gold silicide nano rectangles on a silicon substrate could serve as a simple chemically reactive template for potential applications in nano electronics and catalysts.

Chapter 6

Nano scale phase separation in Au-Ge system on ultra clean Si(100) surfaces

6.1 Introduction

Thermal behavior of gold nanostructures on Silicon substrates were reported in the previous chapters (chapter 3, 4 and 5) and it was found that the temperature of formation Au-Si composition, and the geometry of the resulting gold silicide structures depend on the presence or absence of a native oxide layer at the Au/Si interface and the orientation of the substrate. In this chapter, the above results will be used to study the behaviour of Ge in presence of gold silicide at different surface conditions.

The importance of the study of surface and interface phenomena has been steadily increasing and now constitutes one of the most significant aspects of the semiconductor industry. Knowledge of surface properties of Si, Ge and Au nanostructures are crucial for rapidly developing area of nanotechnology. Metal nanoparticles on semiconductor substrate, facilitates to exploit the nano-particle properties and to fabricate novel and larger integrated devices. Metal nano-particles exhibit unique electronic, magnetic, photonic and catalytic properties which can be employed for the preparation of new materials for energy storage, photonics, communications, and sensing applications [177, 178]. For example, metal over layers have been exploited to tune the characteristics of epitaxial islands/quantum dots, including their size, density and shape

[179, 180]. Additionally, metallic films such as Au on Si have been instrumental in catalyzing the growth of semiconductor nano wires [181] and nano tubes [182, 183]. Starting in the early seventies, the Au-Si junctions in bulk or thin film samples have been extensively investigated using various surface techniques to understand their crystallographic, chemical and electronic properties [184, 185, 186, 187, 188, 189].

Epitaxially grown self organized nanostructures on silicon have been studied in great detail [118, 122, 121, 27, 120]. The size, shape, and material composition of nanostructures for the future prospective applications of nanostructures in optoelectronic and high density data storage devices have been fabricated using MBE facilities. Also, both the homo-epitaxial and the *hetero-epitaxial* growth of different metals on(100) oriented substrate has been studied by several group [124, 125]. In chapter 3, we showed the formation of aligned gold-silicide-nano rectangular structures, when a $\sim 2\text{nm}$ Au film deposited on Si(100) in absence of native oxide at the interface using MBE method and was thermally annealed inside the TEM chamber (*in-situ* TEM) [127].

Successful implementation of germanium technology will however require an understanding of the solid-state interaction in metal-germanium systems [190, 191, 192]. Ge is of particular interest because it has high mobility for both electrons and holes, making a high-speed complementary field-effect transistor a possibility [193]. Because of the low vapour pressure, Au-Ge alloys are used as catalyst for the growth of Ge nano wires inside the UHV chamber[194].

The effect of size on phase stability and phase transformations is of both fundamental and applied interest. For example, during the nucleation and growth of self-assembled nanowires from nanoscale metal catalysts, the phase of the catalyst determines properties such as the growth rate and the structure of the nanowire. Any size-dependent or growth-rate dependent changes in the catalyst may thus have strong effects on the structures that formed [195, 196, 197, 198, 199, 200, 201]. In last five years, interesting works have been carried out in understanding growth of silicon and germanium nanowire in presence of Au as catalyst and deviation in phase diagram of Au-Si and Au-Ge systems by using *in-situ* TEM methods [195, 196, 197, 198, 199, 200, 201]. Systematic results reported by Sutter *et al.* clearly point out the deviation of Ge solubility from bulk for nano-scale systems (typically less than 50 nm size)[196]. The

systems dealt by Sutter *et al.*, are basically for VLS type growth (free standing *out-of-plane* or encapsulated nanowire growth) and the results showed that the phase diagram would deviate from the bulk [196]. Similar results were shown by Kim *et al.* for Au-Si systems [199]. Cheuh *et al* reported on the post growth engineering of the nanowire structures and composition through the alloying and phase segregation that is induced by thermal annealing in Au-Ge system [202]. In these studies, the authors reported the dependence of the Au concentration of the initial nanowires on the formation of nearly periodic nanodisc patterns to core/shell and fully alloyed nanowires. Electrical measurements showed that alloy structures are having metallic characteristics [202].

In this chapter, we present the experimental observation of growth of aligned bilobed Au-Ge nano-structures during *in-situ* thermal treatment inside UHV chamber for gold deposited on Si(100) surfaces without oxide layer at the interface followed by further deposition of Ge on it. *Ex-situ* electron microscopy measurements (both SEM and TEM) confirm the presence of Au and Ge in these bi-lobed structures. The role of gold silicide in formation of the bi-lobed structures has been clearly demonstrated in this work. Also, we have studied the effect of substrate temperature and the sequence in the material deposition on formation of bi-lobed structures. We also show the formation of Ge nanostructures of rectangular shape on the surface where no bi-lobed structures are present[203]. This work will lead to the study of multi component materials, i.e., assemblies of mixtures of nanoparticles at single Silicon substrate.

The overall concept of the fabrication of the bi-lobed structures with nano alloy of $\text{Au}_x\text{Ge}_{1-x}$ at the inter face is shown in figure 6.1. $\text{Au}_x\text{Si}_{1-x}$ nano structures are first grown by MBE and followed by thermal annealing at 500°C under UHV condition (figure 6.1(a)). This facilitated in the formation of $\text{Au}_x\text{Si}_{1-x}$ alloys at the surface. Following this process, Ge is deposited at the substrate temperature of 500°C on this pre-patterned Au-Si surface, forming bi-lobed structures (figure 6.1(c)). Where as only Ge deposition on the Si substrate at 500°C will result in formation of Ge nanostructures (figure 6.1(b)).

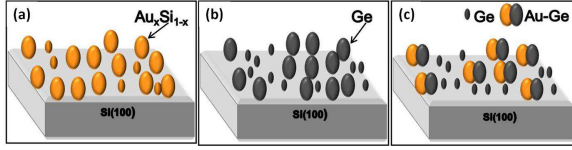


Figure 6.1: Schematic diagrams showing (a) the formation of gold silicide, (b) Ge nano structures and (c) Au-Ge bi-lobed structures on a Si substrate.

6.2 Experimental details

For this present study, we have prepared seven types of samples. For the first case (*sample A*), a thin Au film of thickness of about ≈ 2.0 nm on n-type Si(100) of resistivity $10\text{-}20 \Omega\text{cm}$, by MBE method under ultra high vacuum conditions [128]. Si(100) substrates were loaded into the MBE chamber and degassed at $\approx 600^\circ\text{C}$ for about 12 hours inside the chamber and followed by flashing for about 2 minutes by direct heating at a temperature of $\approx 1200^\circ\text{C}$. In this process, native oxide was removed and a clean Si(100) surface was obtained. On such ultra clean surfaces, ≈ 2.0 nm thick gold films were grown epitaxially by evaporating Au from a Knudsen cell. Deposition rate was kept constant at $\approx 0.14 \text{ nm min}^{-1}$. Table 6.1 gives an overall view about the specimen used in this work. Thermal annealing of the *as-deposited* sample(*sample A*) was carried out inside the UHV chamber at temperature of 500°C with a ramp rate of 7°C min^{-1} (*sample B*). For the third case (*sample C*), we deposited a 2.0 nm gold on Si(100) sample in the MBE chamber as explained above (like *sample A*) and about ≈ 2.0 nm Ge was further deposited at a typical deposition rate of 0.6 ML/min (where one ML corresponds to $6.78 \times 10^{14} \text{ atoms cm}^{-2}$ for a Si(100) surface) at a substrate temperature of 500°C . For fourth case (*sample D*), we have deposited 2.0 nm Ge on the Au patterned (after cooling the sample B to RT) surface while the substrate is at *room temperature*(RT). For fifth case, ≈ 2.0 nm Au was first deposited followed by 2.0 nm Ge, while the substrate was kept at RT. After the deposition of Au and Ge at RT, the specimen was annealed for 30 minutes at 500°C (*sample E*). For sixth case (*sample F1, F2, F3*), a 5.0 nm thick Ge film was deposited (instead of 2.0 nm) using same procedure as above on 2.0 nm Au deposited surface(like *sample A*) with various substrate temperatures: 400°C (*F1*), 500°C (*F2*) and 600°C (*F3*). During the growth, chamber vacuum was $\approx 6.2 \times 10^{-10}$ mbar. The post-growth characterization of the above samples were done with the field emission gun based scanning electron microscopy (FEGSEM) measurements with 20 kV electrons

Name of the sample	Details of the Experimental conditions
Sample A	2.0 nm Au/Si(100) as-deposited
Sample B	2.0 nm Au/Si(100) annealed at 500°C
Sample C	2.0 nm Ge /Sample B
Sample D	2.0 nm Ge /Sample B at RT(Room Temperature)
Sample E	[2.0 nm Ge /2.0 nm Au/Si(100)] annealed at 500°C
Sample F1	5.0 nm Ge /[2.0 nm Au/Si(100) annealed at 400°C]
Sample F2	5.0 nm Ge /[2.0 nm Au/Si(100) annealed at 500°C]
Sample F3	5.0 nm Ge /[2.0 nm Au/Si(100) annealed at 600°C]
Sample G	Sample A annealed at 400°C inside HV chamber

Table 6.1: Summary of the samples [203].

using a Neon 40 cross-beam system. Both cross-sectional and planar TEM specimens were prepared from the above samples. For seventh case (*sample G*), *As-deposited* MBE grown 2.0 nm Au /Si(100) (like *sample A*) was *in-situ* annealed (up to 400°C) inside the TEM using single tilt heating holder with the ramp rate of 7°C min⁻¹. The temperature is measured by a Pt/Pt-Rh thermocouple and is accurate within a couple of degrees. The holder has a water cooling system to avoid over heating of the sample surroundings and the specimen chamber, while keeping only the sample at a specified temperature. The summary of all the above samples are presented in Table 6.1. TEM measurements were performed with 200 keV electrons and scanning TEM (STEM), high resolution TEM measurements were done using 300 keV electrons in the Cs-corrected FEI Titan 80/300 system. The Rutherford backscattering (RBS) measurements were carried out using our 3 MV tandem Pelletron accelerator (9SDH2, NEC, USA) facility at IOPB[98]. During the measurements, 2.0 MeV He⁺ ions were used.

6.3 Results and discussion

Figure 6.2(a) depicts a bright field TEM micrograph of *as deposited* 2.0 nm Au Film on Si(100) without native oxide at the interface (*sample A*). Irregular and isolated gold nanostructures of average size/length 29.3 ± 1.4 nm were formed [203]. It should be noted that the error bars shown here is the error in determining the peak value not the distribution variation. The selected area diffraction pattern (SAD) taken on

a group of nanostructures confirms the polycrystalline nature of the gold films (figure 6.2(b)). A high resolution (HR)TEM taken on a single isolated nanostructure shows the lattice spacing corresponding to elemental gold (inset figure 6.2(a)). The *as-deposited* sample was annealed *in-situ* inside the UHV chamber at 500°C for 30 minutes (*sample B*). Following this annealing in UHV, *ex-situ* TEM measurements (at room temperature) showed rectangles/squares nanostructures aligned along set of planes (110) direction with respect to the silicon substrate (Figure 6.2(c)). The size distribution of the rectangles /squares was already shown in chapter 5 (figure 5.7 (d)). This shape transformation is attributed to the strain relief mechanism [127]. Inset of figure 6.2(c) depicts the bright field HRTEM image of one of the nano island. Figure 6.2(d) and 6.2(e) shows the corresponding selected area diffraction(SAD) pattern taken on group of rectangles/squares and cross-sectional HRTEM image of single rectangles, respectively[203]. SAD shows the single crystalline silicon background and some weak polycrystalline rings of gold along with the dotted ring which corresponds to a d-spacing of about 0.226 nm which matches with the several phases such as Au₅Si₂, Au₅Si, Au₇Si [204]. Figure 6.2(f) shows the SAD pattern taken at RT from the same sample but heated upto 400°C(*sample G*). There was no signal of silicide formation at 400°C. It should be noted that this annealing was carried out using *in-situ* TEM heating stage. More discussion on the effect substrate temperature which plays an important role in formation of gold-silicide nano alloy structures and helps to form Au-Ge bi-lobed structures will be discussed later sections in this chapter.

The average ratio of length along $\langle 110 \rangle$ to length along $\langle 1\bar{1}0 \rangle$ direction, known as "aspect ratio" was determined using several frames like figure 6.2(c). The length distribution along $\langle 110 \rangle$ shows the Gaussian distribution and the average length is 48.1 ± 1.1 nm (figure 6.3(a)). The average aspect ratio has been estimated by fitting the histograms with Gaussian distribution and the average value is 0.998 ± 0.001 indicating that the islands are predominately compact in shape (figure 6.3(b))[203]. In our earlier work [127], we had shown that above 510°C, the average length (25.1 ± 1.6 nm) and aspect ratio (1.12 ± 0.01) values were saturated during the *in-situ* thermal annealing inside the TEM (high vacuum chamber). The percentage of particles having rectangular/square shape was 80%. But here (in UHV annealing), one can clearly see that the almost all the particles are become squares/rectangles having decreased average aspect ratio and increased average length [203]. When a ≈ 2 nm Ge was

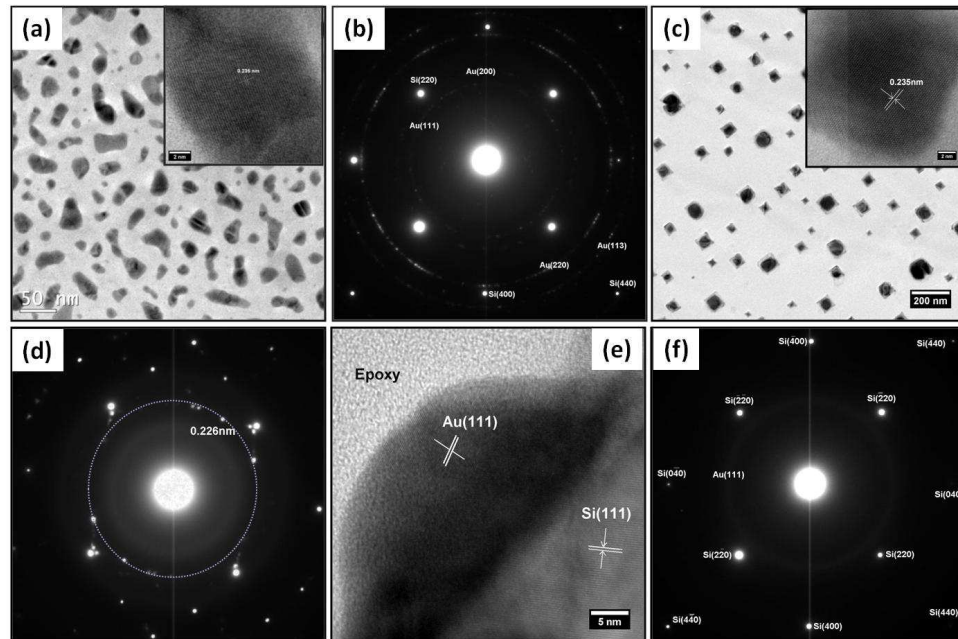


Figure 6.2: (a) *As-deposited (sample A)* showing gold nanostructures with corresponding high resolution image of one of the islands which is showing the d-spacing of Au(111) in the inset (b) SAD pattern showing reflection of both Si and Au, (c) bright field TEM image taken for the sample that was annealed at 500°C in UHV chamber (*sample B*) with corresponding high resolution image of one of the single islands (*inset*), (d) SAD pattern showing the formation gold silicide along with the reflection Au and Si for the sample B, (e) bright field high resolution XTEM image of one of the nanostructure (*sample B*) showing inter-diffusion of Au into Si. (f) Depicts a SAD pattern taken at RT for the sample that was annealed *in-situ* TEM at 400°C (*sample G*) and then cooled to RT. This shows no gold silicide formation at 400°C [203].

further deposited (*sample C*) using MBE system on the above rectangular/square patterned surface at substrate temperature 500°C inside the UHV chamber, bilobed nanostructures of Au and Ge were formed [203]. This means that, Au-Si nanalloys are used as seeding positions for Au-Ge lobe-lobe structures.

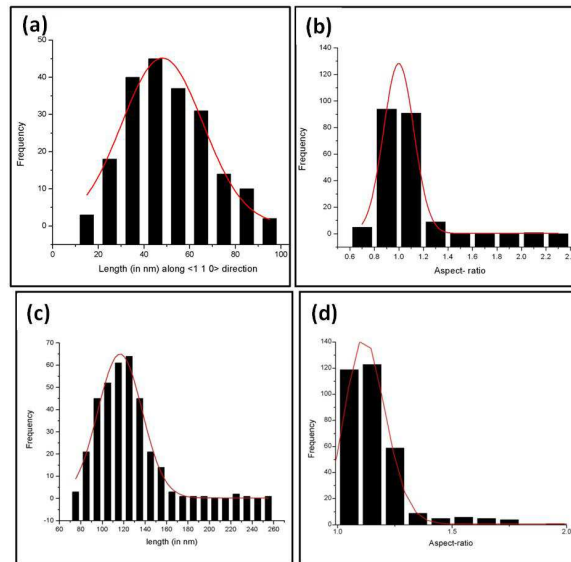


Figure 6.3: Length distribution(fitted with Gaussian distribution) along $\langle 110 \rangle$ direction, of the sample shown in Fig. 6.2(c) which shows an average length of 48.1 ± 1.1 nm and (b) corresponding aspect ratio distribution and average aspect ratio is 0.99 ± 0.01 (here the histograms are fitted with Gaussian distribution to estimate the mean aspect ratio) (c) length distribution(fitted with Gaussian distribution) of the sample shown in Fig. 6.4(a) (for several frames) which shows the average length is 116 ± 1.8 nm and (d) corresponding aspect ratio distribution and average aspect ratio is 1.12 ± 0.03 (here the histograms are fitted with log-normal distribution to estimate the mean aspect ratio) [203].

In figure 6.3(a), SEM image shows the bi-lobed nanostructures of Au and Ge, where the bright contrast is the gold and other one is for the Ge. As gold is higher Z material, more secondary electrons are emitted from the Au region than from Ge region and this causes the contrast difference between gold and germanium in SEM images. The average length and aspect ratio of the bi-lobed (including both Au and Ge) structures is 116 ± 1.8 nm and 1.12 ± 0.03 respectively. The length distribution is fitted with Gaussian distribution and the aspect ratio is fitted with log normal distribution to estimate the average value (figure 6.3(c), 6.3(d)). In addition to the

bi-lobed structures, one can see the formation of rectangular shaped Ge nanostructures having typical size ~ 3.0 nm (figure 6.4(a)). In figure 6.4(c), SEM images taken at 54° tilt have been shown. This shows a three dimensional nature of the Au-Ge nanostructures. Figure 6.4(b) and 6.4(d) depicts high resolution XTEM of the epitaxially grown Ge nano structures and Au-Ge bilobed structures on the silicon substrate respectively. It shows the diffusion of gold into the silicon substrate, where as there was not appreciable diffusion of Ge[203]. This is further confirmed with Rutherford backscattering spectrometry RBS method (figure 6.6(d)). The RBS results would be discussed in the following paragraph.

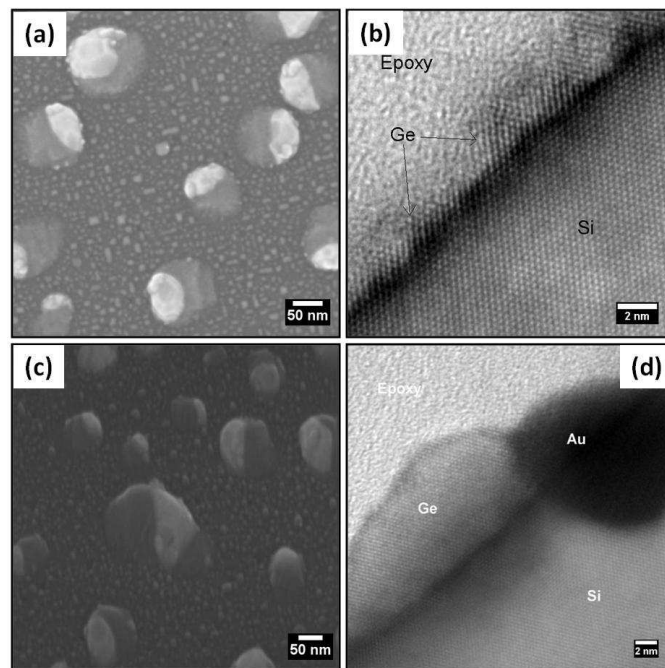


Figure 6.4: (a) SEM image taken at 0° tilt (c) 54° tilt; (b) depicts a XTEM image of epitaxially grown Ge nano structures and (d) for Au-Ge bilobed structures (*sample C*) [203].

We now discuss on the detail structure of bi-lobed structures and the interface between the Au lobe and Ge lobe. The bright field (BF) TEM image in figure 6.5(a) depicted one of the bilobed structures and the corresponding HRTEM image is shown in figure 6.5(b). At the Au-Ge junction (dotted circle) using high resolution images [203], the d-spacing has been found to be of about 0.332 nm and 0.279 nm. These lattice spacing do not match with the Au, Ge or Si but matches quite well with the

(224) and (324) plane of tetragonal phase of $\text{Au}_{0.6}\text{Ge}_{0.4}$ [205]. According to bulk Au-Ge phase diagram, the above composition is formed at 520°C which is comparable with our growth temperature. Also, the lattice spacing value of 0.279 is close to (200) planes of $\text{Si}_{0.25}\text{Ge}_{0.75}$. We need to carry our more studies to come to a conclusion on the interfacial structure (i.e. whether it is Au-Ge or Si-Ge). It should be noted that deviations in the nano-scale phase-diagram to bulk phase diagram are reported by Sutter *et al.*[196].

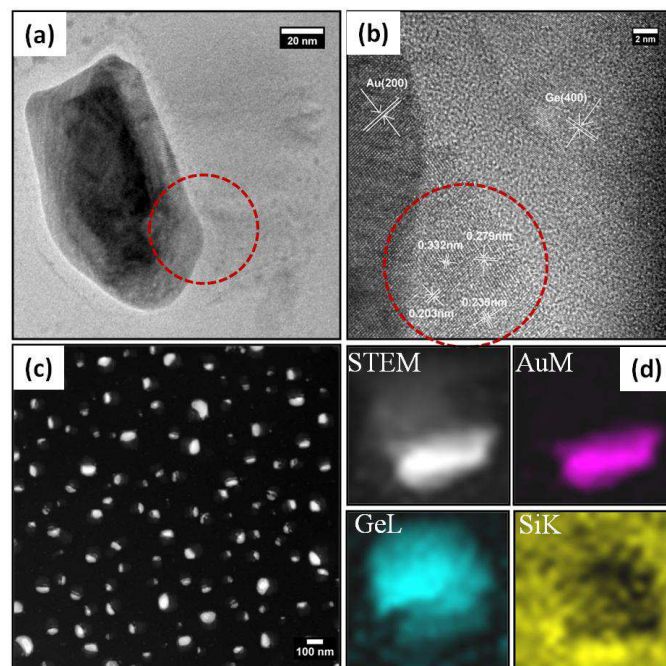


Figure 6.5: (a) Bright field TEM image of one of the bi-lobed Au-Ge nanostructures and (b) corresponding HRTEM images showing the Au-Ge alloy formation at the Au-Ge junction. (c) depicts STEM micrograph (*sample C*) and (d) STEM-EDS elemental mapping (*sample C*)[203].

Figure 6.5(c), depicts a STEM- HAADF (high angle annular dark field) image showing the large area of the specimen with bi-lobed structures. This shows the expected Z-contrast, so that Au appears brighter than the Ge over layer and Si substrate. To analyze the local distribution of Au in these structures, STEM-x-ray energy dispersive spectrometry (XEDS) elemental mapping was carried out. In Figure 6.5(d), STEM EDS elemental mapping shows the presence of Au and Ge in a single bi-lobed structure. Though it is clear about the phase separation of gold (from 6.5(d) - Au

M signal)[203], but it is not very clear about the possible presence of Si-Ge. We need to carry out high resolution cross-section STEM measurements to obtain this information.

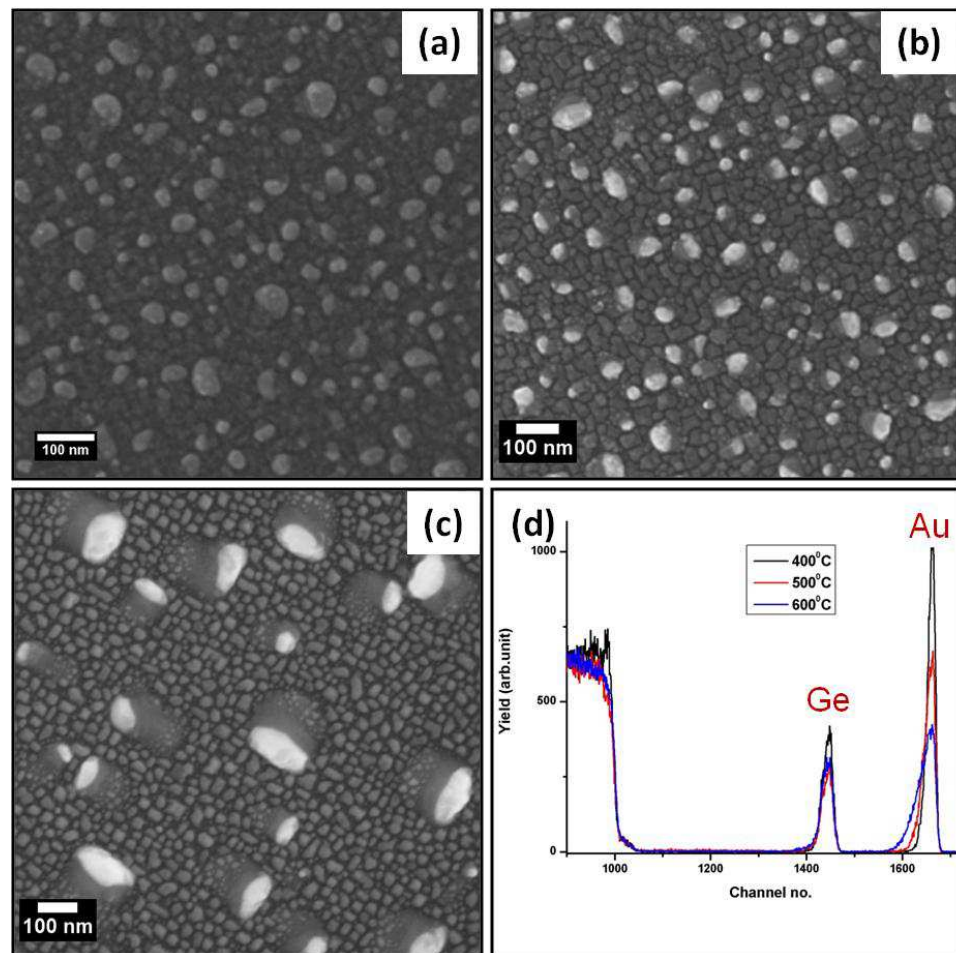


Figure 6.6: SEM image taken at RT after 5.0 nm Ge deposited on Au patterned substrate at (a) 400°C (b) 500°C and (c) 600°C. This shows that no bi-lobed structures are formed at 400°C. Corresponding RBS spectra in (d) show diffusion status of Au and Ge in Silicon at 400°C (*sample F1*), 500°C (*sample F2*) and 600°C (*sample F3*) [203].

Gamalski *et al* have shown the *in-situ* study of formation of liquid Au-Ge alloy during digermane exposure at lower temperature (below 300°C) [206]. In this work *in-situ* real time study has not been done to observe the growth of above nanostructures with temperature. To do the *ex-situ* temperature dependent study, we deposited \approx

5.0 nm Ge on Au patterned surface at 400°C, 500°C and 600°C. Formation of bi-lobed structures was not found in 400°C case (figure 6.6 (a): *sample F1*). Whereas for 500°C and 600°C, more prominent bi-lobed structures were formed (figure 6.6(b), 6.6(c))[203]. For 500°C (*sample F2*), the typical size of the structure was 131 ± 1.7 nm. That means the average size of the bi-lobed structure increases with increasing the amount of Ge. In 600°C (*sample F3*) case, the mean size was 158 ± 2.3 nm which indicates that for same Ge thickness, average size increases with the temperature of the substrate. The Rutherford backscattering spectrometry measurements shown in Figure 6.6(d), confirms the inter-diffusion of gold into Silicon and stability of Ge as a function of temperature. The inter-diffusion of gold into silicon is very well studied.

In the following, we discuss on the possible surface and interface energetic. We calculated the θ_1 and θ_2 values from the image. From that we calculated the value of γ_1 and γ_2 using the relation shown in the text (Equation 6.1 and 6.2). The notations are per the reference [207].

$$\gamma_1 \cos \theta_1 + \gamma_2 \cos \theta_2 = 1 \quad (6.1)$$

$$\gamma_1 \sin \theta_1 = \gamma_2 \sin \theta_2 \quad (6.2)$$

Where θ_1 is the angle between the Au lobe and the normal drawn at the Au, Ge and Si triple point.

θ_2 is the angle between the Ge lobe and the normal drawn at the Au, Ge and Si triple point (figure 6.7).

$\gamma_1 = \frac{\gamma_{Au/Si}}{\gamma_{Au/Ge}}$ and $\gamma_2 = \frac{\gamma_{Ge/Si}}{\gamma_{Au/Ge}}$ (Where $\gamma_{Au/Si}$, $\gamma_{Ge/Si}$, $\gamma_{Au/Ge}$ are the interfacial free energies for the Au-Si, Ge-Si and Au-Ge interfaces).

We compared the γ_1 and γ_2 values for the bi-lobed structures in the present study with the calculation done by Yuan *et al* [207] to check whether the bi-lobed structures are in equilibrium or not. The values of the $\gamma_1 (=1.05)$ and $\gamma_2 (=1.07)$ were well matched with their studies. So these Au-Ge bilobed structures are most likely the equilibrium structures. We have found that by changing the Ge thickness and working temperature, the size of these bilobed structures can be tuned. From the all above studies, it was found that the heated Au-Si alloy structures may play a major role in formation of such bilobed structures. During the deposition of Ge, gold silicide particles act as nucleation center for the growth of Ge. The minimum surface and interfacial energy

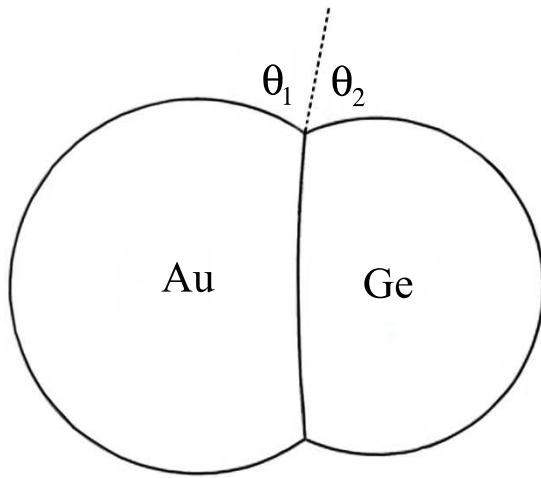


Figure 6.7: Schematic diagram showing the Au and Ge lobe making angle θ_1 and θ_2 respectively with the normal to the triple point. Here the segmented line is perpendicular to the image plane.

for the system is achieved when the Ge is nested within Au and this would be a critical factor during the nucleation of the Ge crystals, where surface energy considerations determine the size and shape of the critical nucleus. As the deposition continues, the smaller liquid droplets provide a rapid diffusion path for the incoming Ge atoms, which find it energetically favorable to join already-nucleated crystals rather than to nucleate new ones. For larger thickness of Ge (5.0 nm), more Ge is nested within Au due to the enhancement of material availability. It resulted in increase in size of the Au-Ge bilobed structures. One can clearly see that at constant temperature of 500°C, the size of the Au-Ge bilobed structures was typically ~ 116 nm for 2 nm Ge case whereas for 5nm Ge case it was ~ 131 nm.

To study the effect of substrate temperature, we deposited 2.0 nm Ge on the gold patterned substrate at room temperature (*sample D*). In figure 6.8(a), SEM image shows the formation of rectangular gold structures and Ge over layers in between the gold structures. Formation of bi-lobed structures was not found in this case[203]. Also we deposited 2.0 nm gold and then 2.0 nm Ge on Si(100) substrate and heated it upto 500°C (*sample E*). During annealing, one would expect the formation of the regular structure following the substrate symmetry of Si(100) as seen in our previous work [127]. But here, both Au and Ge were present on the surface during annealing and as the thermal diffusion coefficient of both the materials is different [208], we observed the formation of irregular Au-Ge structures (figure 6.8(b)). There is a possibility to use the combination of Au, $\text{Au}_x\text{Si}_{1-x}$, Ge, and $\text{Au}_x\text{Ge}_{1-x}$, structures. But, more

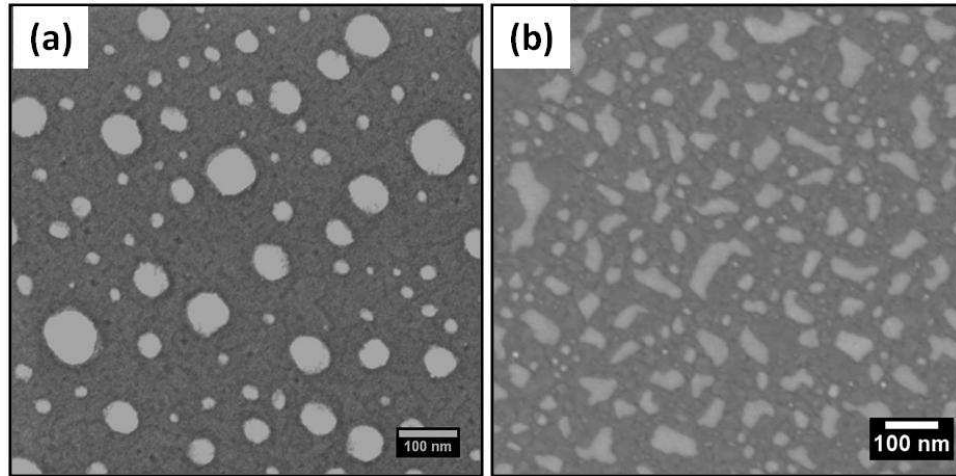


Figure 6.8: SEM images showing absence of Au-Ge bilobed structures for (a) *sample D* and (b) for *sample E* [203].

studies are necessary to have a control on specific combination of the above structures so that technological applications become viable. Further to strengthen our experimental studies, preliminary results have been carried out using first principle density functional method based on gradient corrected approach to study energetic of various bonding strength using binding energy model dimmers for the Au-Ge system [209]. This observation of phase separation at nanoscale would be very useful for proper understanding of gold contacts on Si-Ge based devices. In the next chapter, we will discuss the nanoscale phase separation during the growth of Au nanostructures on Ge substrate.

6.4 Conclusions

We reported the phase separation of Au from Ge on clean Si(100) surface, by carrying out systematic studies under ultra high vacuum conditions and molecular beam epitaxy. The effect of substrate temperature, material deposition sequence and also the role of gold silicide on the formation Au-Ge bi-lobed structures have been studied using scanning electron microscopy and transmission electron microscopy.

Chapter 7

Gold assisted molecular beam epitaxy of Ge nanostructures on Ge (100) Surface

7.1 Introduction

In chapter 6, the role of gold silicide nanostructures as a catalyst in the formation of bi-lobed Au-Ge nanostructures under UHV conditions on clean Si(100) was described. In this chapter, the role of gold nanostructures in the epitaxial growth of Ge nanostructures on cleaned Ge(100) substrate under UHV conditions would be discussed.

Epitaxy of thin films is a key process in modern nano electronic industries. It allows abrupt doping profiles in homoepitaxy and the formation of sharp interfaces in heteroepitaxy to be realized. More than 90 % of semiconductor devices consist of silicon. Knowledge of surface properties of Si, Ge and Au nanostructures are crucial for rapidly developing area of nanotechnology. Successful implementation of germanium technology will however require an understanding of the solid-state interaction in metal-germanium systems [190, 191, 192]. As the feature size becomes smaller the transistor density increases and with it the heat production. This is a problem that can be compensated by using lower driving voltages. To allow this, a higher electron and hole mobility relating the drift current to the applied electric field, is required from the semiconductor. For this, Ge is the right material to achieve this goal because it has high mobility for both electrons and holes [193]. Furthermore,

one dimensional Ge nanostructures/ nanowires show their application in high speed field effect transistor are potentially useful for high speed quantum computing due to the long decoherence time [210]. Also, the advantage of a large excitonic bohr radius in Ge (24.3 nm) allowing for quantum confinement to be observed in relatively larger structures [211] at high temperature. In order to realize this applications, controllable and high quality growth of nanowires are important. In most case, the nanowires are grown in chemical vapor deposition(CVD) method using vapor-liquid-solid(VLS) mechanism in which Au-Ge eutectic plays the vital role. The low vapor pressure of Au-Ge alloys allows to use it as catalyst for the growth of Ge nano wires inside the UHV chamber [194].

The effect of size on phase stability and phase transformations is of both fundamental and applied interest. For example, during the nucleation and growth of self-assembled nanowires from nanoscale metal catalysts, the phase of the catalyst determines properties such as the growth rate and the structure of the nanowire. Any size-dependent or growth-rate dependent changes in the catalyst may thus have strong effects on the structures that formed [195, 196, 197, 198, 199, 200, 201]. In last seven years, interesting works have been carried out in understanding the growth of silicon and germanium nanowire in presence of Au as catalyst. Also, the deviation in phase diagram of Au-Si and Au-Ge system in nanoscale has been extensively investigated by using *in-situ* TEM methods [195, 196, 197, 198, 199, 201]. Epitaxially grown self organized nanostructures on silicon have been studied in great detail [212, 127, 27, 120]. Several works has also been done using the Ge substrate instead of Si [213]. Data concerning the behavior of metal thin films on germanium upon thermal treatment is relatively scarce. The thin film reactions of 20 transition metals, excluding gold, with germanium substrates have been reported by Gaudet *et al* [200].

The main focus of this work is on solid source molecular beam epitaxy of both Au and Ge on Ge (100) substrate. It is similar to the VLS growth of Ge with Au as transport medium, except molecular-beam source is used instead of a chemical compound vapor like CVD growth. This avoids many problems, including the high temperature required to decompose the vapor compound and possible contamination of the growing layer. Also the deposition will be atom by atom which ensures uniform growth of the metal and the semiconductor material at the first stage of the process. Hence,

adatom deposition is not selective and growth is driven by adatom diffusion on the substrate.

The solid solubility of Ge in Au is 3.1 % but that of Au in Ge is very low ($<10^{-5}$ %) [214]. Systematic results reported by Sutter *et al.* clearly point out the deviation of Ge solubility from bulk for nano-scale systems (typically less than 50 nm size) [201]. The systems dealt by Sutter *et al.*, are basically for VLS type growth (free standing out-of-plane NW growth) and the results showed that the phase diagram would deviate from the bulk [201]. Cheuh *et al* reported on the post growth engineering of the nanowire (NW) structures and composition through the alloying and phase segregation that is induced by thermal annealing in Au-Ge system [202]. A direct observation of the VLS growth of Ge nanowires was reported by Wu and Yang [49], who identified the various growth stages in correlation to the Au-Ge binary phase diagram. In our earlier work, we demonstrated that, gold-silicide nano alloy formation at the substrate (Si) surface is necessary for forming phase separated Au-Ge bilobed nanostructures. Our results also indicate that Si-Ge bonding is more favorable to have than having Au-Ge bond. It would be very interesting to study the structural changes in the above Au-Ge nanostructures, when Si substrate will be replaced by Ge substrate under the same ambient [216].

In this chapter, we present the experimental observation of growth of Au-Ge nanostructures during *in-situ* thermal treatment inside UHV chamber for gold deposited on Ge(100) surfaces without oxide layer at the interface followed by further deposition of Ge on it. *Ex-situ* electron microscopy measurements (both SEM and TEM) confirm the presence of Au and Ge in these structures. The formation of Au-Ge nanostructures *via* nanoscale phase separation is demonstrated experimentally. Also, the role of substrate temperature in formation of these structures has been clearly demonstrated in this work [216].

7.2 Experimental methods

For this present study, we have prepared five types of samples. For the first case (*sample A*), a thin Au film of thickness of about ≈ 2.0 nm on n-type Ge(100) by MBE method under ultra high vacuum conditions [128]. Ge (100) substrates were

loaded into the MBE chamber and degassed at $\approx 400^\circ\text{C}$ for about 12 hours inside the chamber and followed by flashing for about 1 minute by direct heating at a temperature of $\approx 800^\circ\text{C}$. In this process, native oxide was removed and a clean Ge(100) surface was obtained. On such ultra clean surfaces, ≈ 2.0 nm thick gold films were grown epitaxially by evaporating Au from a Knudsen cell. Deposition rate was kept constant at ≈ 0.14 nm min^{-1} . Thermal annealing of the *as-deposited* sample (*sample A*) was carried out inside the UHV chamber at temperature of 500°C with a ramp rate of 7°C min^{-1} (*sample B*). Also, we deposited a ≈ 2.0 nm gold on Ge(100) sample in the MBE chamber as explained above (like *sample A*) and about ≈ 2.0 nm Ge was further deposited at a typical deposition rate of 0.6 ML/min (where one ML corresponds to 6.78×10^{14} atoms cm^{-2} for a Si(100) surface) with substrate temperatures: 500°C (*sample C*) and 600°C (*sample D*). It should be noted that Au deposition and annealing and Ge deposition after Au deposition are done sequentially without any break in the vacuum. In addition to this, we deposited ≈ 2.0 nm Ge on Ge((100) substrate followed by annealing upto 500°C (*sample E*). During the growth, chamber vacuum was $\approx 6.2 \times 10^{-10}$ mbar. The post-growth characterization of the above samples were done with the field emission gun based scanning electron microscopy (FEGSEM) measurements with 20 kV electrons using a Neon 40 cross-beam system. Cross-sectional TEM specimens were prepared from the above samples in which electron transparency was achieved through low energy Ar ion milling. TEM measurements were performed with 200 keV electrons under cross-sectional geometries.

7.3 Results and discussions

Figure 7.1 (a) depicts a SEM micrograph of as deposited 2.0 nm Au Film on Ge(100) using MBE (*sample A*). Irregular and isolated gold nanostructures were formed. Fig. 7.1 (b) shows the bright field XTEM image of the interface of gold film and the Ge substrate and corresponding high resolution image (HR) shows the d-spacing of Au(200) and Ge(111) plane (*inset* figure). The *as-deposited* sample was annealed *in-situ* inside the UHV chamber at 500°C for 30 minutes (*sample B*). Following this annealing in UHV, *ex-situ* SEM measurements (at room temperature) showed well distributed gold nanostructures (Figure 7.2 (a)). Figure 7.2 (b) and 7.2 (c) depicts the XTEM image of the Au nanostructures and cross-sectional HRTEM image of

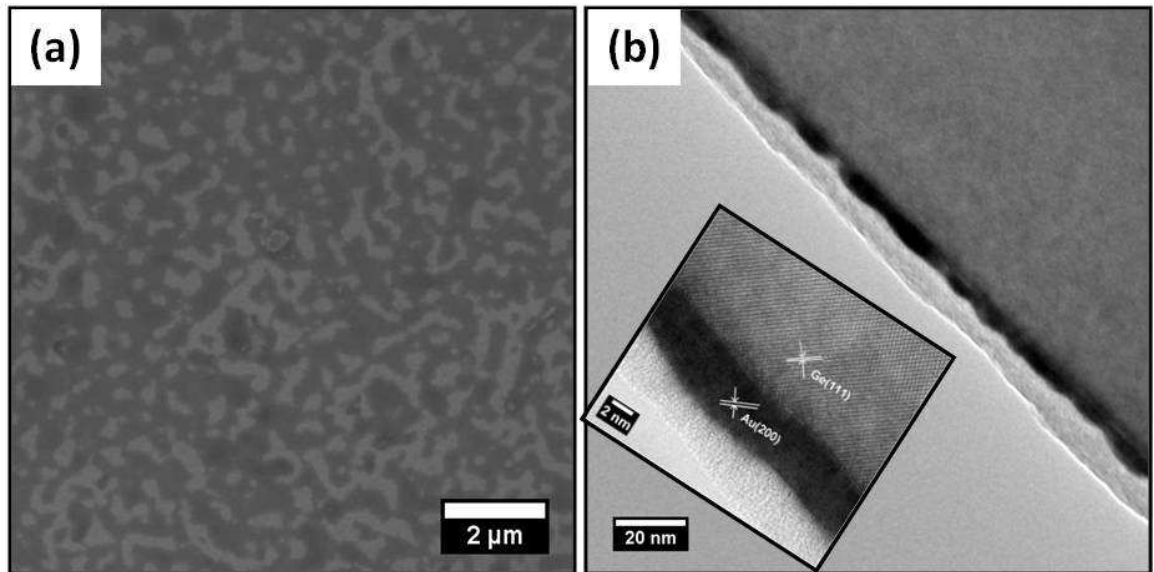


Figure 7.1: For *as deposited* MBE sample (*sample A*), (a) SEM micrograph showing gold nanostructures (b) XTEM image showing the interface of Au thin film and Ge substrate and corresponding high resolution image (*inset figure*) shows d-spacing of Au(200) and Ge(111) [216].

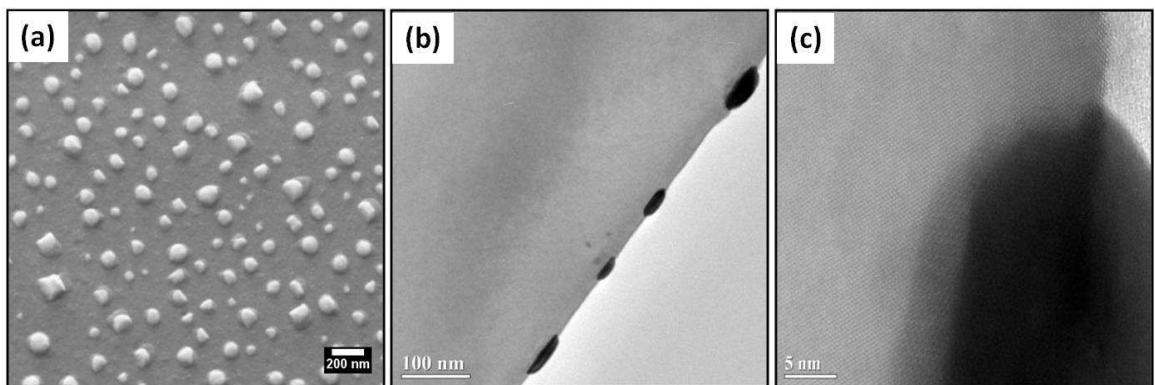


Figure 7.2: (a) SEM image taken at 54° tilt for the sample that was annealed at 500°C in UHV chamber (*sample B*) (b) corresponding bright field XTEM image of the islands and (c) high resolution XTEM image of one of the nanostructure (*sample B*) showing inter-diffusion of Au into Ge substrate [216].

single Au nanostructures respectively. The contrast shows the inter diffusion of gold into the Ge substrate. In our earlier work [127], we had shown that for Au-Si system, gold nano rectangles were formed on Si(100) system for the same annealing condition.

When a ≈ 2 nm Ge was further deposited (*sample C*) using MBE system on the above Au-patterned surface at substrate temperature 500°C inside the UHV chamber, Au nanostructures with prominent Ge pedestal were formed (Figure 7.3 (a)). This means that AuGe nanoalloys are acted as seeding positions for the growth of above structures. Because of the incorporation of larger amount of Ge in to the seed particle, Ge nanostructures with Au on top were formed [216]. Kodambaka *et al.* have shown using *in situ* microscopy for the Ge/Au system that catalysts can be either liquid or solid below eutectic temperature, depending on thermal history. They have shown that with a pre-annealing at 400°C , the Ge/Au catalyst remains liquid down to 255°C [215], this phenomenon has also been reported by Gamalski *et al* [206]. This means that with our growth conditions the catalyst should be still liquid. Sample was then exposed to molecular beam of Ge. In figure 7.3(a), SEM image taken at 54° tilt clearly shows the three dimensional nature of the Au-Ge nanostructures, where gold is on the top of the Ge. The bright contrast is the gold and other one is for the Ge. As Au is higher Z material, more secondary electrons are emitted from the Au region than from Ge region and this causes the contrast difference between gold and germanium in SEM images. In addition to these structures, one can see the formation of Ge nanostructures having typical height ~ 5.0 nm (figure 7.3 (b)). In figure 7.3 (b), bright field XTEM images of the Au-Ge nanostructures along with Ge nano islands has been shown and corresponding high resolution XTEM of the epitaxially grown Ge nano structures is shown in the *inset*. Figure 7.3 (c) depicted HRXTEM micrograph of one of the Au-Ge structures. The typical height of the pedestal Ge is ~ 8.0 nm. Furthermore, one can see that the height of the pedestal Ge is several times larger than the effective thickness of the deposited Ge. The filtered image of the square marked region is demonstrated in figure 7.3 (d). It shows the formation of Au-Ge composition at the interface of top gold and pedestal Ge. The d-spacing has been found to be of about 0.332 nm which do not match with the Au or Ge but matches quite well with the (224) plane of tetragonal phase of $\text{Au}_{0.6}\text{Ge}_{0.4}$ [205].

To do the temperature dependent study, we deposited 2.0 nm Ge on Au patterned

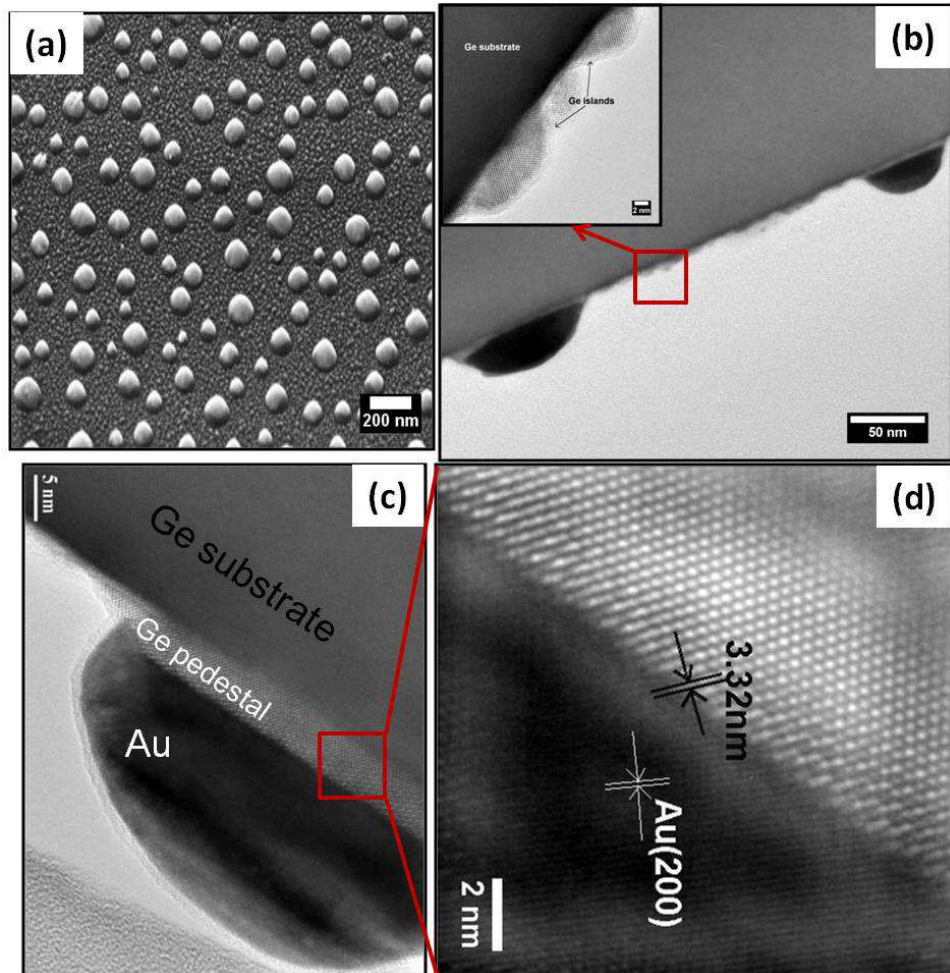


Figure 7.3: (a) SEM micrograph taken at RT after 2.0 nm Ge deposited on Au patterned substrate at 500°C (*sample C*), (b) corresponding XTEM image shows the Au-Ge nanostructures along with the Ge nano islands (the High resolution of the square marked region is shown in the *inset*), (c) HRXTEM image of one of the Au-Ge islands depicts the pedestal Ge underneath the Au and (d) filtered image of the square marked region shows the formation of Au-Ge composition at the interface [216].

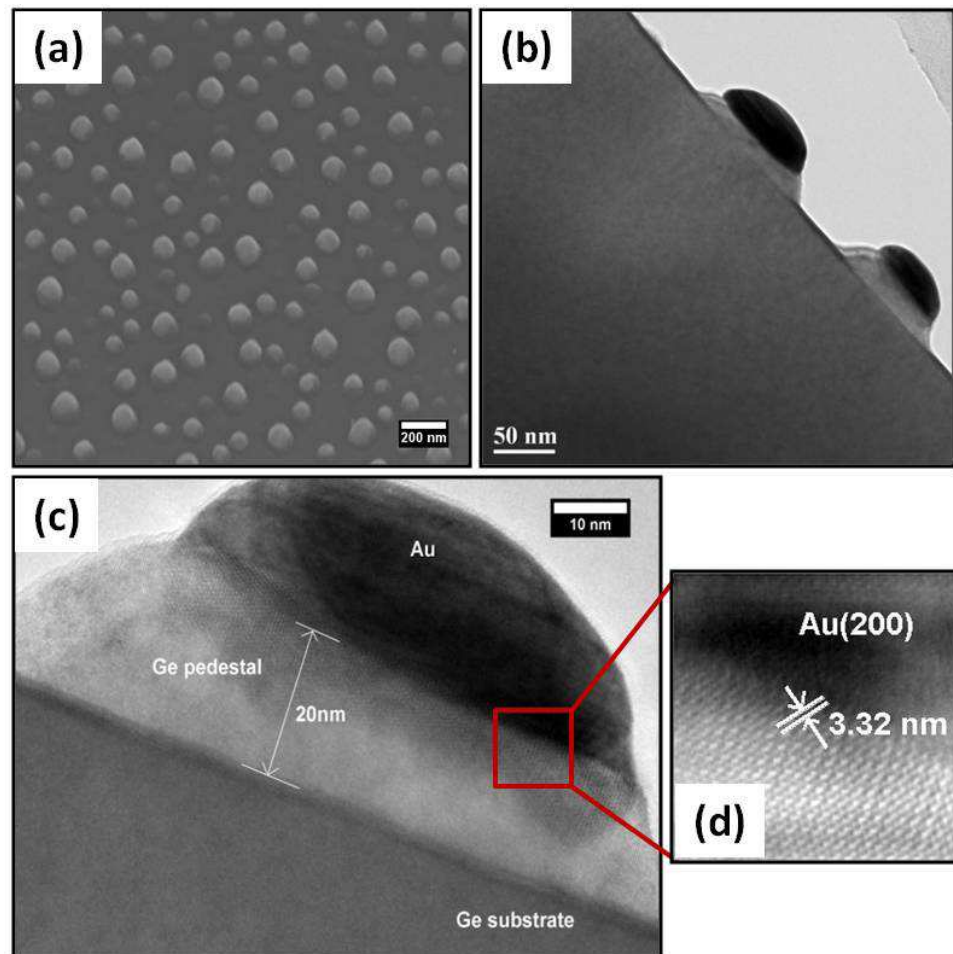


Figure 7.4: (a) SEM micrograph taken at RT after 2.0 nm Ge deposited on Au patterned substrate at 600°C (*sample D*), (b) corresponding XTEM image shows the Au-Ge nanostructures, (c) HRXTEM image of one of the Au-Ge islands depicts the pedestal Ge underneath the Au and (d) filtered image of the square marked region shows the formation of Au-Ge composition at the interface [216].

surface at 600°C (*sample D*). Formation of the above Au-Ge structures having typical size of the pedestal ~ 20 nm has been observed (figure 7.4 (a)). It should be noted that, there is no formation of small Ge islands in this case and the height of the pedestal is more than 500°C case. In figure 7.4 (b), one can clearly see the only formation of Au nanostructures with Ge as pedestal. At higher enough temperature (600°C), atoms are arriving into the seeding particle not only from the molecular beam but also from the Ge islands due to self diffusion. This resulted in increase in height of the pedestal Ge. Figure 7.4 (c) depicted the HRXTEM micrograph of one of such structures. The filtered image of the square marked region is shown in figure 7.4 (d). The d-spacing shows the formation of $\text{Au}_{0.6}\text{Ge}_{0.4}$ [205] composition at the junction of top gold and pedestal Ge. In both the cases, the Au-Ge composition was found at the interface [216]. It has been studied that the composition is not only depend on the annealing temperature but also on the cooling rate [213]. Thus, there will be some composition gradient at the interface.

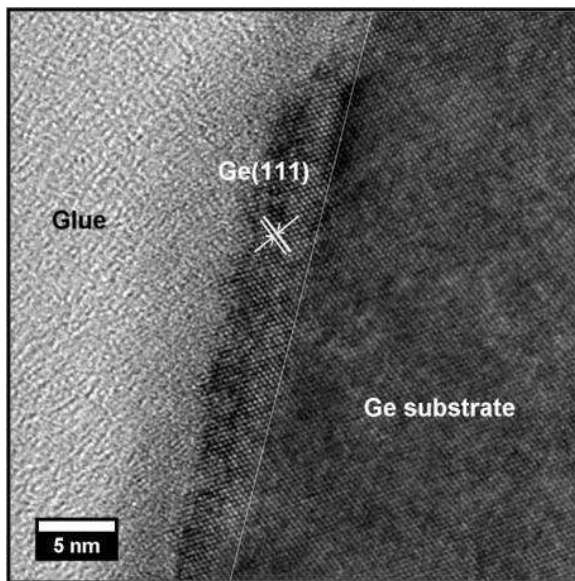


Figure 7.5: High resolution XTEM of the sample taken at *RT* after 2 nm Ge was deposited on Ge (100) followed by UHV annealing at 500°C (*sample E*), shows the homo epitaxial growth of Ge layer on Ge (100) [216].

From the above studies, it was found that the heated Au-Ge alloy structures may play a major role in formation of such Au-Ge structures. During the deposition of Ge, gold germanide particles act as nucleation center for the growth of Ge. As the deposition continues, the smaller liquid droplets provide a rapid diffusion path for the incoming Ge atoms, which find it energetically favorable to join already-nucleated crystals

rather than to nucleate new ones. As substrate is also Ge and the Ge-Ge bonding is more favorable than Au-Ge bonding, Ge pedestal were formed underneath gold. Another interesting aspect of this study is the formation of Ge islands. In *sample C*, well distributed Ge nanoislands were formed along with Au-Ge structures. To study the effect of gold over layers on formation of islands, ≈ 2 nm Ge was deposited on cleaned Ge (100) surface followed by annealing at 500°C (*sample E*). Formation of Ge nanoislands were not seen (Figure 7.5). In figure 7.5, the HRXTEM shows the homo epitaxial growth of Ge layer on the Ge(100) surface without islanding. The dotted white line is the sharp interface between the Ge layer and the Ge substrate. Thus presence of gold layer resulted in formation of Ge islands [216].

Numerous interesting aspects of Au-Ge nanostructures formation can still be studied. For instance, it would be both fascinating and beneficial to study the real time measurements of phase separation in Au-Ge system. Better understanding of growth of Au-Ge nanostructures *via* phase separation could be achieved by performing more *in-situ* experiments. This observation of phase separation at nanoscale would be very useful for proper understanding of gold contacts on Si-Ge based devices.

7.4 Conclusions

We reported the out of plane growth of epitaxial Au-Ge nanostructures by using molecular beam epitaxy. The interesting part of this work is to get the growth parameters in UHV condition to enhance the in plane material transport which leads to formation of out of plane Au-Ge nanostructures. The effect of substrate temperature and role of gold on the formation of above structures has been studied in detail.

Chapter 8

Summary

The thesis lays out a detailed study on the formation of Au-Si and Au-Ge nanostructures under different thermal annealing conditions achieved by varying parameters such as, pressure, film thickness, substrate, presence or absence of native oxide on the substrate, temperature *etc.* The emphasis is on the use of self-assembly techniques to synthesize well tuned Au, Ge, Au-Si and Au-Ge alloyed nano structures and to study the reaction between them at different ambient using transmission electron microscopy (TEM). The results obtained in the present thesis are important for the proper understanding of the growth of Au-Si and Au-Ge nanostructures of different shape and sizes which can be used for the synthesis of semiconductor nanowires. The study also presents the formation of well oriented 3D gold nano/microstructures that can be decoupled from the substrate for the real applications. *In-situ* studies of Au-Si systems at various temperatures (from RT to 850°C) were performed using the single tilt hot-stage holder. Transmission Electron Microscopy (TEM), Scanning TEM (STEM)-combined with HADDF, EDS, Scanning electron microscopy (SEM), Electron backscattered diffractometry (EBSD) and Focused ion beam (FIB) measurement are some of the techniques which have been employed to illustrate the formation of nanostructures and their properties. Rutherford backscattering spectrometry (RBS) was used for the study of diffusion along with the above techniques. Physical vapor deposition method and molecular beam epitaxy method were used to deposit thin films.

Variation in the temperature dependent behavior of gold nanostructures on Si(100) surfaces in presence and absence of native oxide layer were studied *in-situ* using a hot-stage holder inside TEM. In case of MBE samples, formation of highly oriented

square /rectangular shape nano silicide structures of average size ~ 25 nm and aspect ratio ~ 1.12 were observed at high temperatures (500°C). Selected area diffraction pattern (SAD) confirms the formation of mixed phase of gold silicide. Strain relaxation and substrate symmetry plays a major role in the alignment of these Au-Si nanostructures. In case of samples with native oxide layer, formation of bigger sized rectangular structures was observed at higher temperatures (850°C) as compared to MBE samples. Native oxide at the interface was found to act like a barrier for the inter-diffusion phenomena. At these higher temperatures, due to desorption of native oxide present at the interface, gold silicide followed the symmetry of the substrate which resulted in the formation of rectangular structures. Desorption of gold and /or gold silicide structures and formation of symmetric hole like structures in some cases was also observed.

Formation of oriented gold nano/ microstructures has been studied experimentally in Au films of various thicknesses (5.0, 11.7 and 50 nm) deposited on Si(100) surface, annealed at high temperature ($\sim 975^\circ\text{C}$) and low vacuum ($\sim 10^{-2}$ mbar) conditions. For 5.0 nm case, the average size and height of the spherical gold structure was found to be ~ 17 nm and ~ 22 nm respectively. For higher thickness cases, well oriented multi-faceted 3D gold nanostructures were observed. The average size and height of the structures increases with the increase in the initial thickness of the gold film. Interestingly, gold silicide formation was not observed in all above cases. The role of native oxide layer on morphology, orientations of the structures was studied in detail. Interfacial oxide layer, low vacuum and high temperature annealing conditions are found to be necessary to grow oriented gold structures. We also showed that oriented microstructures cannot be fabricated without oxide layer at the interface (using MBE method). These gold structures can be taken out from the substrate by simple scratching method.

In vacuum dependence study, the influence of vacuum conditions upon the formation of nanostructures in presence and absence of oxide layer has been reported by depositing ~ 2 nm Au on Si(100) using thermal evaporation method as well as MBE method followed by thermal annealing. For PVD grown samples (with oxide case), sample was annealed at high temperature (850°C) under both high vacuum (HV) and low vacuum (LV) conditions. In HV, gold silicide rectangles were observed following the

four-fold symmetry of the substrate due to selective thermal decomposition of native oxide layer, where as in LV, it does not show any such formation. This has been explained as due to low vacuum which ensures that the rate of formation(re-deposition) of oxide takes over the rate of oxide decomposition in a relatively oxygen rich environment compared to high vacuum conditions. For MBE grown samples (without oxide case), sample was annealed at 500°C in three different vacuum conditions: (i) LV external furnace ($\sim 10^{-2}$ mbar), (ii) ultra high vacuum (UHV at $\sim 10^{-10}$ mbar) chamber (MBE chamber), (iii) HV ($\sim 10^{-7}$ mbar). Although well aligned nano rectangles were formed in both HV and LV, corner rounding is more prominent in LV. Furthermore in UHV, random structures were formed having sharp corners. In all the above three cases, samples were exposed to air before annealing. To study the effect of surface oxide, *in-situ* annealing inside UHV-MBE chamber was done without exposing to air. Well aligned rectangles with sharp corners (no corner rounding) were formed. The details about the role of surface oxide in the corner rounding process have been discussed.

The role of gold silicide nanostructures as a catalyst in the formation of lobe-lobe (bi-lobed) Au-Ge nanostructures under UHV conditions on clean Si(100) surfaces has been described. For this study, ~ 2.0 nm thick Au films were grown by MBE. Nearly square shaped goldsilicide nano structures of average length ~ 48 nm were formed after UHV annealing at temperature $\sim 500^\circ\text{C}$. A ~ 2 nm Ge film was further deposited on the annealed sample while the substrate was kept at $\sim 500^\circ\text{C}$. Well ordered Au-Ge nanostructures where Au and Ge residing side by side (lobe-lobe structures) were formed. In our systematic studies, we demonstrated that, gold-silicide nano alloy formation at the substrate (Si) surface is necessary for forming phase separated Au-Ge bilobed nanostructures. The morphology of such bi-lobed structures has been tuned by varying thickness (amount) of the Ge, substrate temperature and sequence of material deposition. Our results indicate that Si-Ge bonding is more favorable to have than having Au-Ge bond. To study this nanoscale phase separation and its effect on the formation bilobed structures, it would be interesting to study growth of Au on Ge. For this study, a ~ 2.0 nm thick Au films were grown on Ge(100) substrate by MBE. Nearly square shaped $\text{Au}_x\text{Ge}_{1-x}$ nano structures were formed after UHV annealing at temperature $\sim 500^\circ\text{C}$. A ~ 2 nm Ge film was further deposited on

the annealed sample while the substrate was kept at 500°C. Well distributed Au-Ge nanostructures with Au on the top of the pedestal Ge were formed. It is very interesting to notice that no Au-Ge bilobed structures were formed. In temperature dependence study, similar Ge deposition was performed at the substrate temperature of 600°C. The height of the pedestal Ge increased with temperature.

Numerous interesting aspects of Au-Ge nanostructures formation can still be studied. For instance, it would be both fascinating and beneficial to study the real time measurements of phase separation in Au-Ge system. Better understanding of growth of Au-Ge nanostructures *via* phase separation could be achieved by performing more *in-situ* experiments.

In conclusion, the thesis emphasizes on three aspects that are relevant in the emerging area of nanoscience and nanotechnology: (i) *in-situ* studies of formation of well aligned rectangular shaped nano gold silicide structures, (ii) systematic studies on the role of interfacial oxide layer and vacuum level in making of highly oriented gold nano/micro structures and (iii) studies of formation of Au-Ge nanostructures of different shapes via nanoscale phase separation.

Appendix A

Table to summarize the results of chapter 3-chapter 5

In this appendix, we summarize (in tabular form) the results presented in chapter 3, 4 and 5.

	Chapter No.	Thickness of Au Film	Details of Experimental conditions	Results
Oxide at the interface	5	2.0 nm	HV annealed at 850°C	Rectangle/Square nanostructures were formed
	3	5.0 nm	HV annealed at 850°C	Rectangle/Square nanostructures were formed
	4	11.7 nm	HV annealed at 975°C	Faceted structures were not formed
	4	50.0 nm	HV annealed at 850°C	Faceted structures were not formed
	4	5.0 nm	LV annealed at 975°C	Spherical nano particles were formed
	4	11.7 nm	LV annealed at 975°C	Faceted structures were formed
	4	50 nm	LV annealed at 975°C	Faceted structures were formed
Without Oxide at the interface	3	2.0 nm	HV annealed at 500°C	Rectangle/Square nanostructures with rounded corners were formed
	5	2.0 nm	LV annealed at 500°C	Rectangle/Square nanostructures with rounded corners were formed
	5	2.0 nm	UHV annealed at 500°C	Less Rectangle/Square nanostructures with sharp corners were formed
	5	2.0 nm	UHV annealed at 500°C (in-situ)	Well aligned Rectangle/Square nanostructures with sharp corners were formed
	4	11.7 nm	LV annealed at 975°C	Fractal type textures along with irregular structures were formed (No facets formation)

Bibliography

- [1] M. S. Gudiksen, L. J. Lauhon, J. Wang, D. C. Smith and C. M. Lieber, *Nature* **415**, 617 (2002).
- [2] L. J. Lauhon, M. S. Gudikson, D. Wang and C. M. Lieber, *Nature* **420**, 57 (2002).
- [3] U. Srinivasan, M. A. Helmbrecht, R. S. Muller and R. T. Howe, *Optics Photonics News* **13**, 20 (2002).
- [4] K. F. Bhringer, *J. Micromech. Microeng.* **13**, S1-S10 (2003) .
- [5] C. N. R. Rao, P. J. Thomas and G. U. Kulkarni, *Nanocrystals: Synthesis, Properties and Applications* (Springer, 2007).
- [6] S. Link and M. A. El-Sayed, *J. Phys. Chem. B* **103**, 8410 (1999).
- [7] W. P. Halperin, *Rev. Mod. Phys.* **58**, 583 (1986).
- [8] A. Dowling, *Nanoscience and nanotechnologies: opportunities and uncertainties* (A Report by The Royal Society and The Royal Academy of Engineering, London, July 2004).
- [9] S. J. Tans, A. R. M. Verschueren and C. Dekker, *Nature* **393**, 49 (1998)
- [10] M. Grundmann, F. Heinrichsdorff and N. N. Ledentsov, *Jpn. J. Appl. Phys* **39**, 2341 (2000)
- [11] G. A. Somorjai and Y. G. Borodko, *Catalysis Letter* **76**, 1 (2001)
- [12] N. K. Mal, M. Fujiwara and Y. Tanaka, *Nature* **421**, 350 (2003)
- [13] M. Taneike, F. Abe and K. Sawada, *Nature* **424**, 294 (2003)

- [14] H. Gleiter, *ActaMaterial* **48**, 1 (2000)
- [15] S. Nafis, Z. X. Tang and B. Dale, *J. Appl. Phys.* **64**, 5835 (1988)
- [16] A. E. Berkowitz, J. R. Mitchell and M. J. Carey, *Phys. Rev.Lett.* **68**, 3745 (1992)
- [17] A. S. Eldenstein, J. S. Murday and B. B. Rath, *Progress in Materials science* **42**, 5 (1997)
- [18] J. P. Borel, *Surf. Sci.* **106**, 1 (1981)
- [19] Y. D. Glinka, S. H. Lin, L. P. Hwang, Y. T. Chen, N. H. Tolk, *Phys. Rev. B* **64**, 085421 (2001)
- [20] C. Burda, X. Chen, R. Narayanan, M. A. El-Sayed, *Chem. Rev.* **105**, 1025 (2005)
- [21] S. Chen, R. S. Ingram, M. J Hostetler, J. J. Pietron, R. W Murray, T. G. Schaaff, J. T. Khoury, M. M. Alvarez, R. L. Whetten, *Science* **280**, 2098 (1998)
- [22] N. L. Swanson and B. D. Billard, *Nanotechnology* **14**, 353 (2003)
- [23] H. Xu, E. J. Bjerneld, M. Kall and L. Borjesson, *Phys. Rev.Lett.* **83**, 4357 (1999)
- [24] C. J. Murphy, T. K. Sau, A. M. Gole, C. J. Orendorff, J. Gao, L. Gou, S. E. Hunyadi and T. Li, *J. Phys. Chem. B* **109**, 13857 (2005).
- [25] Federico Rosei, *J. Phys.: Condens. Matter* **16**, S1373-S1436 (2004).
- [26] J. Tersoff and R. M. Tromp, *Phys. Rev. Lett.* **70**, 2782 (1993).
- [27] S. H. Brongersma et al. , *Phys. Rev. Letts.* **80**, 3795-3798 (1998).
- [28] K. Sekar, G. Kuri, P. V. Satyam, B. Sundaravel, D. P. Mahapatra, B N Dev, *Surf Sci.* **339**, 96 (1995).
- [29] K. Sekar, G. Kuri, P. V. Satyam, B. Sundaravel, D. P. Mahapatra, B N Dev, *Phys Rev. B* **51**, 14330 (1995).
- [30] Y. Li and G. Shi, *J. Phys. Chem. B*, **109**, 23787 (2005).
- [31] L. Qian and X. Yang, *J. Phys. Chem. B*, **110**, 16672 (2005).

- [32] Y. He, X. Yu and B. Yang, *Mater. Chem. Phys.* **99**, 295 (2006).
- [33] Y. Li, G. Lu and G. Shi, *J. Phys. Chem. B*, **110**, 24585 (2006).
- [34] E. Piscopiello, L. Tapfer, M.V. Antisari, P. Paiano and P. Prete, *Phys. Rev. B* **78**, 035305 (2008).
- [35] M. G. Warner and J. E. Hutchison, *Nature Materials* **2**, 272 (2003).
- [36] Y. Xiao, F. Patolsky, E. Katz, J. F. Hainfeld and I. Willner, *Science* **299**, 1877 (2003).
- [37] A. T. Bell, *Science* **299**, 1688 (2003).
- [38] B. Hammer and J. K. Norskov, *Nature* **376**, 238 (1995).
- [39] M. Valden, X. Lai and D. W. Goodman, *Science* **281**, 1647 (1998).
- [40] E. Wahlstrom *et al*, *Phys. Rev. Lett.* **90**, 026101(2003).
- [41] M. Haruta, *Catal. Today* **36**, 153 (1997).
- [42] G. R. Bamwenda, S. Tsubota, T. Nakamura and M. Haruta, *Catal. Lett.* **44**, 83(1997).
- [43] B. Rout , B. Sundaravel, A. K. Das, S. K. Ghose, K. Sekar, D. P. Mahapatra, *J. Vac. Sci. Technol. B* **18**, 1847 (2000).
- [44] R. Tromp, G. W. Rublo, P. Balk, F. K. LeGoues and E. J. van Loenen, *Phys. Rev. Lett.* **55**, 2332 (1985).
- [45] G. W. Rubloff, *J. Vac. Sci. Technol. A* **8**, 1857 (1990).
- [46] R. S. Wagner, W. C. Ellis, *Trans. Metall. Soc. AIME* **233**, 1053 (1965).
- [47] D. Hourlier, P. Perro, *Materials Science Forum* **653**, 77-85 (2010).
- [48] E. Sutter, P. Sutter, *Nano Lett.* **8**, 411 (2008).
- [49] Y. Wu, P. Yang, *J. Am. Chem. Soc.* **123**, 3165 (2001).
- [50] F. M. Ross, J. Tersoff, M. C. Reuter, *Phys. Rev. Lett.* **95**, 146104 (2005).

- [51] K. Haraguchi, T. Katsuyama, K. Hiruma, K. Ogawa, *Appl. Phys. Lett.* **60**, 745 (1992).
- [52] F. Banhart (Ed.), *In-situ electron microscopy at high resolution* (World scientific publications, 2008).
- [53] D. W. Pashley, M. J. Stowell, M. H. Jacobs and T. J. Law, *Phil. Mag.* **10**, 127 (1964).
- [54] K. Yagi, *Thin Solid Films* **126**, 95 (1985).
- [55] R. Sinclair, T. Yamashita and F. A. Ponce, *Nature* **290**, 386 (1981).
- [56] J. M. Howe, A. R. S. Gautam, K. Chatterjee and F. Phillipp, *Acta Mater.* **55**, 2159 (2007).
- [57] K. L. Merkle, L. J. Thompson and F. Phillipp, *Phys. Rev. Lett.* **88**, 225501-1 (2002).
- [58] K. Sasaki and H. Saka, *Phil. Mag. A* **63**, 1207 (1991).
- [59] R. Sinclair, *Mater. Res. Soc. Bull.* **XIX**, 26 (1994).
- [60] R. Sinclair, J. Morgiel, A. S. Kirtikar, I. W. Wu, and A. Chiang, *Ultramicros.* **51**, 41 (1993).
- [61] H. Gabrisch, L. Kjeldgaard, E. Johnson, and U. Dahmen, *Acta Mater.* **49**, 4259 (2001).
- [62] J. G. Lee and H. Mori, *J. Mater. Res.* **20**, 1708 (2005).
- [63] S. Iijima, *J. Electron Micros.* **34**, 249 (1985).
- [64] L. D. Marks, *Rep. Prog. Phys.* **57**, 603 (1994).
- [65] R. Sinclair, T. Yamashita, M. A. Parker, K. B. Kim, K. Holloway, and A. F. Schwartzman, *Acta Cryst. A* **44**, 965 (1988).
- .
- [66] Krishna Seshan (Ed.), *Handbook of thin-film deposition processes and techniques* (Noyes Publications, New York, 2002). Second Ed.

- [67] M. Ohring *Materials Science of Thin films. Deposition and Structure* (Academic Press, 2002).
- [68] R. Glang, "Vacuum evaporation" Ch I in *Thin film technology* (McGraw-Hill Book Co., 1970).
- [69] Donald M. Mattox and William Andrew, Vacuum Evaporation and Vacuum Deposition Ch V in *Hand book of PVD processing* (Noyes Publications, New York, 1998).
- [70] A. Cho, *J. Vac. Sci. Tech.* **8**, 31-38 (1971).
- [71] A. Cho and J. Arthur, *Prog. Solid-State Chem.*, **10**, 157-192 (1975).
- [72] H. Hirayama, M. Hiroi, K. Koyama, T. Tatusmi, and M. Sato, *Mat. Res. Soc. Symp. Proc.*, **220**, 545-556 (1991).
- [73] H. Jorke, H. Kibbel, F. Schaffler, and H. J. Herzog, *Thin Solid Films* **183**, 307-313 (1989).
- [74] Y. Shiraki, *Prog. Crystal Growth Charact.* **12**, 45-66 (1986).
- [75] S. L. Delage, Silicon molecular beam epitaxy: capabilities and trends, *Academic Press*, 207-254 (1989).
- [76] K. Oura, V. G. Lifshits, A. A. Saranin, A. V. Zotov and M. Katayama, *Surface Science - An Introduction* (Springer-Verlag, 2003).
- [77] Donald E. Savage, Feng Liu, Volkmar Zielasek, and Max G. Lagally, *Germanium Silicon: Physics and Materials* (SEMICONDUCTORS AND SEMIMETAL, Vol 56, chapter-2 (Academic press, 1999).
- [78] D. K. Goswami, B. Satpati, P. V. Satyam and B. N. Dev, *Current Science* **84**, 903 (2003).
- [79] D. B. Williams and C. Barry Carter, *Transmission Electron Microscopy* Vol. I-IV (Plenum Press, New York, 1996).
- [80] John C. H. Spence, *High-resolution Electron Microscopy* (Oxford University Press 2003), 3rd Ed.

- [81] Brent Fultz and James Howe, *Transmission Electron Microscopy and Diffractometry of Materials* (Springer, 2005), 2nd Ed.
- [82] M. Knoll and E Ruska, *Z. Physik.* **78**, 318 (1932).
- [83] J. M. Cowley, A.F. Moodie, *Acta Crystallogr.* **10**, 609 (1957).
- [84] Earl J. Kirkland, *Advanced Computing in Electron Microscopy* (Plenum press , New York and London, 1998).
- [85] It is a freeware available at <http://rsbweb.nih.gov/ij/>. A more detail documentation is available at <http://www.macbiophotonics.ca/imagej/>.
- [86] *Digital Micrograph 3.4 Users Guide* (Gatan, Inc., 1999).
- [87] *DIFPACK Users Guide* (Gatan, Inc., 1999).
- [88] J.Ackermann, *Manual for the SUPRA (VP) and ULTRA Scanning Electron Microscopes. Smart SEM V. 05.00. 2005. Carl Zeiss SMT Ltd.*
- [89] J. Goldstein, et al., *Scanning Electron Microscopy and X-ray Microanalysis*(Kluwer Academic/Plenum Publishers, 2003), third edn.
- [90] V. F. Leavers, *Shape Detection in Computer Vision Using the Hough Transform* (Springer- Verlag, New York, 1992).
- [91] Adam J. Schwartz, M. Kumar and B. L. Adams, *Electron backscatter diffraction in Material science* (Kluwer Academic/ Plenum Publisher (NewYork))
- [92] Robert J. Keyse, Anthony J. Garrett-Reed, Peter J. Goodhew and Gordon W. Lorimer, *Introduction to scanning transmission electron microscopy* (Bios Scientific Publishers, 1998).
- [93] Peter W. Hawkes, John C. H. Spence, *Science of microscopy*, vol **1**, (Springer-2008)
- [94] N. D. Browning, E. M. James, K. Kishida, I. Arslan, J. P. Buban, J. A. Zaborac, S. J. Pennycook, Y. Xin, and G. Duscher, *Rev.Adv.Mat.Sci.*, **1**, 1-26 (2000).
- [95] P.Hartel, H. Rose and C. Dinges, *Ultramicroscopy* **63**, 93 (1996).
- [96] E. Rutherford, *Phil. Mag.* **21**, 669 (1911).

- [97] W. K. Chu, J. W. Mayer, M. A. Nicolet, *Backscattering spectrometry* (Academic Press, New York, 1978).
- [98] K. Sekhar, G. Kuri, P. V. Satyam, B. Sundaravel, D. P. Mahapatra and B. N. Dev, *Indian J. Phys.* **684**, 1 (1994).
- [99] M. Mayer, *Proceedings of the 15th International Conference on the Application of Accelerators in Research and Industry*, J. L. Duggan and I.L. Morgan (eds.), American Institute of Physics Conference Proceedings, Denton, USA, **475**, 541 (1999).
- [100] C. L. Cheung, A. Kurtz, H. Park and C. M. Lieber, *J. Phys. Chem. B* **106**, 2429 (2002).
- [101] S. Helveg, C. Lopez-Cartes, J. Sehested, P. L. Hansen, B. S. Clausen, J. R. Rostrup-Nielsen, F. Abild-Pedersen and J. K. Nørskov, *Nature* **427**, 426(2004).
- [102] K. A. Dick, K. Deppert, L. S. Karlsson, L. R. Wallenberg, L. Samuelson and W. Seifert, *Adv. Funct. Mater.* **15**, 1603(2005).
- [103] J. B. Hannon, S. Kodambaka, F. M. Ross and R. M. Tromp, *Nature* **440**, 69 (2006).
- [104] E. Moyén et al, *Appl. Phys. Lett.* **94**, 233101 (2009).
- [105] A. Bezryadin, C. Dekker and G. Schmid, *Appl. Phys. Lett.* **71**, 1273 (1997).
- [106] T. Morita and S. Lindsay, *J. Am. Chem. Soc.* **129**, 7262 (2007).
- [107] J. M. Mativetsky, S. A. Burke, S. Fostner and P. Grutter, *Small* **3**, 818 (2007).
- [108] B. Li et al, *Nanotechnology* **20**, 085304 (2009).
- [109] H. Wang et. al., *ACS Nano* **4**, 2901(2010).
- [110] G. M. Whitesides and B. Grzybowski, *Science* **295**, 2418-2421(2002).
- [111] A. Hiraki, M. A. Nicolet and J. W. Mayer, *Appl. Phys. Lett.* **18**, 178(1971).
- [112] T. Narusawa, S. Komiya and A. Hiraki, *Appl. Phys. Lett.* **22**, 389(1973).
- [113] A. Hiraki, E. Lugujo and J. W. Mayer, *J. Appl. Phys.* **43**, 3643(1972).

- [114] A. Hiraki, K. Shuto, S. Kim, W. Kammura and M. Iwami, *Appl. Phys. Lett.* **31**, 611(1977).
- [115] M. Iwami, S. Kim, W. Kammura and A. Hiraki, *Japan. J. Appl. Phys* **19**, Suppl. 1489 (1980).
- [116] J. W. Mayer and K. N. Tu, *J. Vac. Sci. Technol.* **11**, 86 (1974).
- [117] A. K. Green and E. Bauer, *J. Appl. Phys.* **47**, 1286 (1974).
- [118] G. Le Lay, *Sur.Sci.* **132**, 169(1983).
- [119] F. H. Baumann and W. Schroeter, *Philos. Mag. Lett.* **57**, 75 (1988).
- [120] M. Mundschaue, E. Bauer, W. Telieps, *Surface science* **213**, 381-392(1989).
- [121] U. M. Bhatta, J. K. Dash, A. Roy, A. Rath and P. V. Satyam, *J. Phys. Condens. Matter* **21**, 205403 (2009).
- [122] U. M. Bhatta, J. K. Dash, A. Rath and P. V. Satyam, *Applied Surface Science* **256**, 567 (2009).
- [123] U. M. Bhatta, J. K. Dash, A. Rath, J. Ghatak, L. Yi-Feng, C.P. Liu and P. V. Satyam, *Nanotechnology* **20**, 465601(2009).
- [124] E. Kopatzki, S. Giinther, W. Nichtl-Peche and R. J. Behm, *Surface Science* **284**,154-166(1993).
- [125] S. Frank, H. Wedler, and R. J. Behm, *Phys Rev. B* **66**, 155435(2002).
- [126] Vasisht Sanjeev and Shirokoff John, *Applied Surface Science* **256**, 4915-4923 (2010).
- [127] A. Rath, J. K. Dash, R. R. Juluri, A. Rosenauer and P. V. Satyam, *J. Phys D: Appl Phys* **44**, 115301 (2011): *arXiv:1202.0647*
- [128] D. K. Goswami, B. Satpati, P. V. Satyam and B. N. Dev, *Curr. Sci.* **84**, 903(2003).
- [129] Ijima Sumio and T. Ichihashi, *Phys. Rev. Lett.* **56**, 616(1986).
- [130] B. Ressel, K. C. Prince, Y. Homma and S. Heun, *J. Appl. Phys.* **93**, 3886 (2003).

- [131] C. Suryanarayana, T. R. Anantharaman, *Mater. Sci. Eng.* **13**, 73 (1974).
- [132] T. R. Anantharaman, H. L. Luo, W. Klement, *Nature*(London) **210**, 1040 (1966).
- [133] H. L. Gaigher and N. G. Vander Berg, *Thin Solid Films* **68**, 373 (1980).
- [134] A. K. Green and E. Bauer, *J. Appl. Phys.* **47**, 1284 (1976).
- [135] B. Y. Tsaur and J. W. Mayer, *Philos. Mag. A* **43**, 345 (1981).
- [136] Au₇Si (JCPDS 26-0723), Au₅Si (JCPDS 26-0725), Au₅Si₂ (JCPDS 36-0938), Au₂Si (JCPDS 40-1140), Au₃Si (JCPDS 24-0463)
- [137] L. Hultman, A. Robertson, T. G. Hentzell, I. Enstroem and P. A. Psaras, *J. Appl. Phys.* **62**, 3647 (1987).
- [138] D. N. McCarthy and S. A. Brown, *J. Phys. Conference series* **100**, 072007 (2008).
- [139] J. H. Wei, S. C. Lee, P. Balk, F. K. LeGoues and E. J. van Loenen *J. Electrochem. Soc.* **144**, 1870 (1997).
- [140] Xiaoge Gregory Zhang, *Electrochemistry of Silicon and Its Oxide* (KLUWER ACADEMIC PUBLISHERS, 2001).
- [141] F. Ruffino, M. G. Grimaldi, F. Giannazzo, F. Roccaforte and V. Raineri, *Appl. Phys. Lett.* **89**, 263108 (2006).
- [142] H. Wohltjen and A. W. Snow, *Anal. Chem.* **70**, 2856 (1998).
- [143] S. A. Maier, H. A. Atwater, *J. Appl. Phys.* **98**, 011101 (2005).
- [144] A. N. Shipway, E. Katz and I. Willner, *Chem. phys. chem.* **1**, 18 (2000)
- [145] M. Haruta, *Gold Bull.* **37**, 27 (2004)
- [146] J. R. Lakowicz, *Plasmonics* **1**, 5 (2006).
- [147] R. Grisel, K. J. Weststrate, A. Gluhoi, and B. E. Nieuwenhuys, *Gold Bull.* **35**, 39 (2002).

- [148] Vasisht Sanjeev and Shirokoff John, *Applied Surface Science* **256**, 4915-4923 (2010).
- [149] H. Sadan and W. D. Kaplan, *J. Mater Sci*, **41**, 5099-5107 (2006).
- [150] C. M. Muller et al , *Nanotechnology* **19**, 485306 (2008).
- [151] L. D. Marks, *Rep. Prog.Phys.* **57**, 603 (1994).
- [152] L. D. Marks, *Ultramicroscopy*, **18**, 445-452 (1985).
- [153] N. P.Young, M. A. van Huis, H. W. Zandbergen, H. Xu and A. I. Kirkland, *Ultramicroscopy*,**110**, 506-516 (2010).
- [154] S. Dhara and K. G. M. Nair, *Appl. Phys.Lett.* **85**, 692 (2004).
- [155] J. S. Wu, Y. F. Chen, S. Dhara, C. T. Wu,K. H. Chen and L. C. Chen, *Appl. Phys. Lett.* **82**, 4468 (2003).
- [156] G. Wulff, *Z Krystallogr Mineral* **34**, 449 (1901).
- [157] B. E. Sundquist, *Acta Metall* **12**, 67 (1964).
- [158] J. C. Heyraud, J. J. Metois, *Acta Metall* **28**, 1789 (1980).
- [159] Z. M. Wang, P. Wynblatt, *Surface Sci* **398**,259 (1998).
- [160] F. Ruffino et al., *Journal of Nanoparticle Research* **13**, 2329 (2011).
- [161] A. Rath, J. K. Dash, R. R. Julur, A. Rosenauer, Marcos Schoewalter and P. V. Satyam, *J. Appl. Phys.* **111**, 064322 (2012) :arXiv:1203.0819v1 [cond-mat.mes-hall]
- [162] JCPDS-**0111174**
- [163] A. A. Stekolnikov and F. Bechstedt, *Phys. Rev. B* **72**, 125326 (2005).
- [164] P. Politi, G. Grenet, A. Marty, A. Ponchet, and J. Villain, *Phys. Rep.* **324**, 271 (2000).
- [165] I. Daruka, J. Tersoff, and A. L.Barabasi, *Phys. Rev. Lett.* **82**, 2753 (1999).
- [166] D. Ito, M. L. Jespersen and J. E. Hutchison, *ACS Nano* **2**, 2001(2008).

- [167] C. R. Henry, *Prog. Surf. Sci.* **80**, 92 (2005).
- [168] Thomas Engel, *Surf. Sci. Rep.* 18 (1993) 91.
- [169] B. Nielsen, K. G. Lynn and T. C. Leung, *Phys. Rev. B* **44**, 1812 (1991).
- [170] H. Dallaporta, M. Liehr and J. E. Lewis, *Phys. Rev. B* **41**, 5075 (1990).
- [171] Jun Wang, C. E. J. Mitchell, R. G. Egdell and J. S. Foord, *Surf. Sci.* **506**, 66 (2000).
- [172] A. Rath, R. R. Juluri and P. V. Satyam, *J. Crystal Growth* (Under review, 2012):arXiv:1204.4618.
- [173] A. Rath, J. K Dash, R. R. Juluri and P. V. Satyam, *J. Vac. sci. technol A-Lett.* (Under review, 2012):arXiv:1204.5370.
- [174] Au₅Si₂ (JCPDS 36-0938), Au₃Si (JCPDS 24-0463).
- [175] D. D. Wagman, W. H. Evans, V. B. Parker and R. H. Shumm et al., tables of thermodynamic chemical properties.
- [176] JANAF, Thermochemical Tables US National Beareau of Standards, National Standard Reference Data Series - **37** (*2nd Ed*), 1971.
- [177] H. J. Freund, *Surf. Sci.* **500**, 271 (2002).
- [178] S. W. Boettcher, N. C. Strandwitz, M. Schierhorn, N. Lock, M. C. Lonergan, and G. D. Stucky, *Nat. Mater.* **6**, 592 (2007).
- [179] I. Berbezier, A. Ronda, A. Portavoce and N. Motta, *Appl. Phys. Lett.* **83**, 4833 (2003).
- [180] D. J. Eaglesham, F. C. Unterwald and D. C. Jacobson, *Phys. Rev. Lett.* **70**, 966 (1993).
- [181] H. J. Fan, P. Werner, and M. Zacharias, *Small* **2**, 700 (2006) and references therein.
- [182] Y. B. Li, Y. Bando and D. Golberg, *Adv. Mater.* **16**, 37 (2004).
- [183] Goldberger, J. He, R. R. Zhang, Y. F. Lee, S. W. Yan, H. Q. Choi and H. J. Yang, *Nature*, **422**, 599 (2003).

- [184] A. K. Green and E. Bauer, *Surf. Sci.* **103**, L127 (1981).
- [185] K. Meinel and D. Katzer, *Appl. Surf. Sci.* **514**, 56 (1992).
- [186] A. Hiraki and M. Iwami, *Jpn. J. Appl. Phys., Suppl.* **2**, 749 (1974).
- [187] J. Han, D. Jeon, and Y. Kuk, *Surf. Sci.* **376**, 237 (1997).
- [188] F. H. Baumann and W. Schroter, *Phys. Rev. B* **43**, 6510 (1991).
- [189] B. Bokhonov and M. Korchagin, *J. Alloys Compd.* **312**, 238 (2000).
- [190] Y. F. Hsieh, L. J. Chen, E. D. Marshall and S. S. Lau, *Appl. Phys. Lett.* **51**, 1588 (1987).
- [191] O. Thomas, S. Delage, F. M. d'Heurle and G. Scilla, *Appl. Phys. Lett.* **54**, 228 (1989)
- [192] S. Q. Hong, C. M. Comrie, S. W. Russell and J. W. Mayer, *Appl. Phys.* **70**, 3655 (1991).
- [193] J. J. Rosenberg, *IEEE Trans. Electron. Devices* **ED-30**, 1602 (1983).
- [194] H. Adhikari, A. F. Marshall, I. A. Goldthorpe, C. E. D. Chidsey and P. C. McIntyre, *ACS Nano*, **1**, 415 (2007).
- [195] R. Kohler, W. Neumann, M. Schmidbauer, M. Hanke, D. Grigoriev, P. Schafer, H. Kirmse, I. Hausler, and R. Schneider, *NanoScience and Technology, Semiconductor Nanostructures* (D. Bimberg(ed.) **chapter 5**) Springer, 2008, 97-121, DOI: 10.1007/978-3-540-77899-85
- [196] E. A. Sutter and P. W. Sutter, *ACS Nano* **4**, 4943 (2010).
- [197] W. Neumann, H. Kirmse, I. Husler, I. Otto and I. Hhnert, *J. Alloys and Compounds* **382**, 2 (2004).
- [198] I. Goldfarb, *Phys. Rev. Lett.* **95**, 025501 (2005)
- [199] B. Kim, J. Tersoff, S. Kodambaka, M. C. Reuter and F. M. Ross, *Science* **322**, 1070(2008).
- [200] S. Gaudet, C. Detavernier, A. J. Kellock, P. Desjardins and C. Lavoie, *J. Vac. Sci. Technol. A* **24(3)**, 474 (2006).

- [201] E. Sutter and P. Sutter, *Nanotechnology* **22**, 295605(2011).
- [202] Y. L. Chueh et al, *Nano Lett.* **10**, 393(2010).
- [203] A. Rath, J. K. Dash, R. R. Juluri, Marco Schowalter, Knut Mueller, A. Rosenauer and P. V. Satyam, *J. Appl. Phys.* **111**, 104319 (2012) : *arXiv:1202.0614*
- [204] Au₇Si (JCPDS 26-0723), Au₅Si (JCPDS 26-0725), Au₅Si₂ (JCPDS 36-0938).
- [205] Au_{0.6}Ge_{0.4} JCPDS 18-0551.
- [206] A. D. Gamalski, J. Tersoff, R. Sharma, C. Ducati and S. Hofmann, *Nano Lett.* **10**, 2972 (2010).
- [207] C. W. Yuan, S. J. Shin, C. Y. Liao, J. Guzman, P. R. Stone, M. Watanabe, J. W. Ager III, E. E. Haller and D. C. Chrzan, *Appl. Phys. Lett.* **93**, 193114 (2008).
- [208] D. Srivastava and B. J. Garrison, *Phys. Rev. B* **46**, 1472 (1992).
- [209] A. Rath, J. Dash, J. J. Raghava, Albert Dearden, S. Nayak (*to be Published*).
- [210] Y. J. Hu *et. al.*, *Nature Nanotechnology* **2**, 622 (2007).
- [211] X. H. Sun *et. al.*, *J. Vac. sci. technol. B* **25**, 415 (2007)
- [212] A. Shibata, *surface science* **303**, 161 (1994) .
- [213] S. Hajjar et al, *Phys. Rev. B* **84**, 125325 (2011) and references there in.
- [214] G. V. Samsonov and V. N. Bondarev, *Germanides*, Published by consultants Bureau, New York, **52** (1969).
- [215] S. Kodambaka, J. Tersoff, M. C. Reuter, F. M. Ross, *Science* **316**, 729 (2007) .
- [216] A. Rath, J. K. Dash, R. R. Juluri, A. Ghosh and P. V. Satyam (*to be Published*):arXiv:1208.0238.